

Cross-shore morphodynamics of intertidal sandbars

A conceptual model, empirical evidence and numerical modelling

Lennard Spaans

June 2019

 TU Delft

Cross-shore morphodynamics of intertidal sandbars

A conceptual model, empirical evidence and numerical modelling

By

Lennard Spaans

in partial fulfilment of the requirements for the degree of

Master of Science
in Civil Engineering

at the Delft University of Technology,
to be defended publicly on Wednesday June 5, 2019 at 13:30 PM

Supervisor:	Dr. S.E. (Sander) Vos	TU Delft
Thesis committee:	Prof. dr. ir. A.J.H.M. (Ad) Reniers	TU Delft
	Dr. ir. S. (Sierd) de Vries	TU Delft
	Dr. ir. R.T. (Robert) McCall	Deltares

Abstract

The beach recovery process determines the resilience of a sandy coast and is an important aspect of the coastal safety. Sediment stored underwater due to storms is transported onshore by the migration of subtidal and intertidal bars under mild wave conditions. The intertidal zone is an important interface, connecting the marine and aeolian zone and facilitating the transition of hydrodynamic to aeolian sediment transport. The aim of this study is to investigate the cross-shore morphodynamics of intertidal sandbars.

The dominant cross-shore sediment transport processes can mainly be divided into surf zone and swash zone processes. The surf zone processes are primarily determined by the balance of wave nonlinearities, undertow and infra-gravity waves. In the swash zone, the cross-shore sediment transport is determined by the balance between the turbulent uprush and the gravity induced backwash.

A recent terrestrial laser scanning (TLS) measuring campaign conducted at Kijkduin, the Netherlands, provided new insight in the intertidal bar behavior. The results of one cross section are analyzed. In a period of 6 weeks, two distinctive intertidal bars formed, grew and migrated onshore during mild wave conditions and eventually eroded again during a storm. Within 5 days, the upper intertidal bar migrated onshore over a distance of 25m and grew with a height of 0.3m, attributed to swash zone processes. Onshore sediment transport fluxes reached values of nearly 2 m³ per meter width in one tidal cycle.

The findings are compared with two XBeach models (surf beat model and hydrostatic swash model) which are used to reproduce the observed morphological behavior of the upper intertidal bar. Both models partly reproduce the onshore migration but show deviating results regarding the final growth of the intertidal bar. In contrast to the surf beat model, the morphological changes in the hydrostatic swash model are primarily induced by swash zone processes, which is comparable to the processes in the TLS measurements.

Finally, a conceptual model is developed in which four intertidal bar regimes are classified based on the tidal water level. The distinction determines the dominant cross-shore processes for the formation, migration, growth and destruction of intertidal bars. The model shows that the swash zone processes are dominant for the onshore migration and growth of intertidal bars in the overwash regime, while the surf zone processes are dominant in the submersion regime.

The findings presented in this study provide a better understanding of the intertidal bar behavior. Although the XBeach models did not reproduce the observed behavior completely, there are some pronounced similarities. Further research is required to increase the knowledge of intertidal bar behavior at a variety of sandy coasts and to improve the performance of processes-based models like XBeach.

Keywords: Intertidal sandbars; cross-shore sediment transport; conceptual model; terrestrial laser scanning; XBeach

Contents

Abstract	v
Nomenclature	ix
1. Introduction	1
1.1. Background.....	1
1.2. Problem definition.....	2
1.2.1. Recent progress in measuring and modelling	2
1.3. Research questions.....	3
1.4. Thesis outline.....	3
2. Theoretical background of the physical processes involving intertidal bars	5
2.1. Coastal terminology	5
2.1.1. The coastal region	5
2.1.2. Beach states.....	6
2.1.3. Storm impact regimes	6
2.1.4. Sediment transport	7
2.2. Cross-shore sediment transport processes.....	8
2.2.1. Surf zone processes.....	8
2.2.2. Swash zone processes	10
2.3. Literature review on intertidal bars	12
2.4. Initial conceptual model.....	13
2.5. Conclusion	15
3. Study area	17
3.1. Coastal setting	17
3.2. Available data	18
4. TLS measurements	21
4.1. Data collection.....	21
4.2. Data selection.....	22
4.2.1. Period selection	22
4.2.2. Cross section selection	23
4.3. Data processing	24
4.3.1. Transformation and corrections.....	25
4.3.2. Selecting the ROI	25
4.3.3. Noise removal.....	26
4.3.4. Object removal	28

4.3.5. Interpolation.....	29
4.3.6. Additional corrections	29
4.4. Results	32
4.4.1. Period A (mild- and storm period).....	32
4.4.2. Period B (onshore intertidal bar migration)	34
4.5. Conclusion	37
5. XBeach modelling	39
5.1. Model selection and description.....	39
5.1.1. Hydrodynamic model selection.....	40
5.1.2. Sediment transport: surf beat model.....	41
5.1.3. Sediment transport: hydrostatic swash model	42
5.1.4. Bottom change	44
5.2. Model setup	45
5.2.1. General setup	45
5.2.2. Surf beat model setup	45
5.2.3. Hydrostatic swash model setup	48
5.3. Results	51
5.3.1. Surf beat model	51
5.3.2. Hydrostatic swash model	52
5.3.3. XBeach model performance	54
5.4. Conclusion	57
6. Developing a conceptual model	59
7. Discussion.....	63
7.1. TLS measurement accuracy.....	63
7.2. TLS measurement and XBeach model comparison	63
8. Conclusion and recommendations	67
8.1. Conclusion	67
8.2. Recommendations.....	69
Bibliography	71
A. Laser scanner details.....	75
B. TLS measurement results for cross sections 2 and 3.....	76
C. XBeach model results for increased wave energy	79

Nomenclature

Abbreviation

GLM	Generalized Lagrangian Mean
GPS	Global Positioning System
JONSWAP	Joint North Sea Wave Project
LiDAR	Light Detection And Ranging
MHW	Mean High Water
MLW	Mean Low Water
NAP	Normaal Amsterdams Peil, Dutch local datum
NLSWE	Non-Linear Shallow Water Equations
OET	Open Earth Tools
PLS	Permanent laser scanning
ROI	Region Of Interest
TIN	Triangular Irregular Network
TLS	Terrestrial laser scanning
TMA	Texel, Marsen and Arsloe

Symbols

α	Bed-slope calibration factor	[-]
β	Beach slope	[rad]
β_b	Local bed slope	[rad]
β_d	Turbulent stirring calibration factor	[-]
β_s	Bed-slope correction factor	[-]
γ	Peak enhancement factor	
Δ	Relative weight of sediment (≈ 1.6 for sand)	[-]
ϵ_b	Surf similarity parameter	[-]
ϵ_s	Suspended load efficiency	[-]
θ'	Non-dimensional shear stress	[-]
θ_{cr}	Shields criterion for initiation of motion	[-]
θ_m	Mean wave direction	[rad]
u_h	Turbulent eddy viscosity	[m ² /s]
ϕ	Critical bed slope	[rad]
Ω	Dimensionless fall velocity	[-]
A_s	Wave asymmetry parameter	[-]
A_{sb}	Bed load coefficient	[-]
A_{ss}	Suspended load coefficient	[-]

C	Depth-averaged sediment concentration	$[m^3/m^3]$
$C_{eq,b}$	Depth-averaged equilibrium bed load concentration	$[m^3/m^3]$
$C_{eq,s}$	Depth-averaged equilibrium suspended load concentration	$[m^3/m^3]$
D	Grain size diameter	[m]
D_h	Sediment diffusion coefficient	$[m^2/s]$
$f_{2.5}$	Wave friction factor	[-]
f_{As}	Wave asymmetry calibration factor	[-]
f_{mor}	Morphological acceleration factor	[-]
f_{sk}	Wave skewness calibration factor	[-]
f_{Ts}	Adaptation time calibration factor	[-]
g	Gravitational acceleration	$[m/s^2]$
H_b	Breaking wave height	[m]
H_{m0}	Significant wave height	[m]
h	Water depth	[m]
K	Horizontal diffusivity coefficient	$[m^2/s]$
k	Turbulent kinetic energy	$[m^2/s^2]$
k_b	Near-bed wave-breaking induced turbulence	$[m^2/s^2]$
p	Sediment porosity	[-]
S_b	Bed load sediment transport volume	$[m^3/m/s]$
S_k	Wave skewness parameter	[-]
S_s	Suspended load sediment transport volume	$[m^3/m/s]$
S_x	Sediment transport volume in the cross-shore direction	$[m^3/m/s]$
$S_{x,slope}$	Sediment transport volume (including bed-slope correction)	$[m^3/m/s]$
S_y	Sediment transport volume in the longshore direction	$[m^3/m/s]$
s	Wave spreading coefficient	[-]
T	Wave period	[s]
T_p	Peak wave period	[s]
T_s	Adaptation time	[s]
U_{cr}	Critical velocity	[m/s]
u_a	Mean flow velocity component due to nonlinear waves	[m/s]
u^E	Eulerian flow velocity	[m/s]
u^L	Generalized Lagrangian Mean flow velocity	[m/s]
u_{rms}	Short wave orbital velocity	[m/s]
$u_{rms,2}$	Near-bed short wave orbital velocity	[m/s]
w_s	Sediment fall velocity	[m/s]
z_b	Bed level	[m]
z_s	Surface level	[m]

1. Introduction

1.1. Background

Intertidal sandbars are frequently occurring features in the recovery process of sandy coastal systems with a significant tidal range (Masselink et al., 2006a). After a storm, the recovery process is an important aspect of the coastal safety and determines the resilience of a coast. During storm events the beach-dune system is eroding, and a so-called winter profile is created with a relatively gentle slope (see Figure 1-1a). After the storm, under mild wave conditions, the coastal system is slowly recovering (see Figure 1-1b), ultimately creating a summer profile with a wide beach and steep slope (see Figure 1-1c). These seasonal changes determine the variability of the coastal system (Wright and Short, 1984).

In the recovery process, sediment stored underwater is transported onshore by the migration of subtidal and intertidal bars (Houser, 2009), as shown in Figure 1-1b. Ultimately, the bars weld to the beach where the sand dries. From there, sand is transported by wind up to the dunes where it can be stored more permanently. The intertidal zone plays an important role in this recovery process, where high onshore sediment transport rates (Masselink et al., 2006a) and a transition from hydrodynamic to aeolian sediment transport can be found (Hoonhout and de Vries, 2017). The cross-shore intertidal sandbar behavior is the topic of this MSc thesis, observed in terrestrial laser scanning measurements and reproduced by numerical modelling in XBeach.

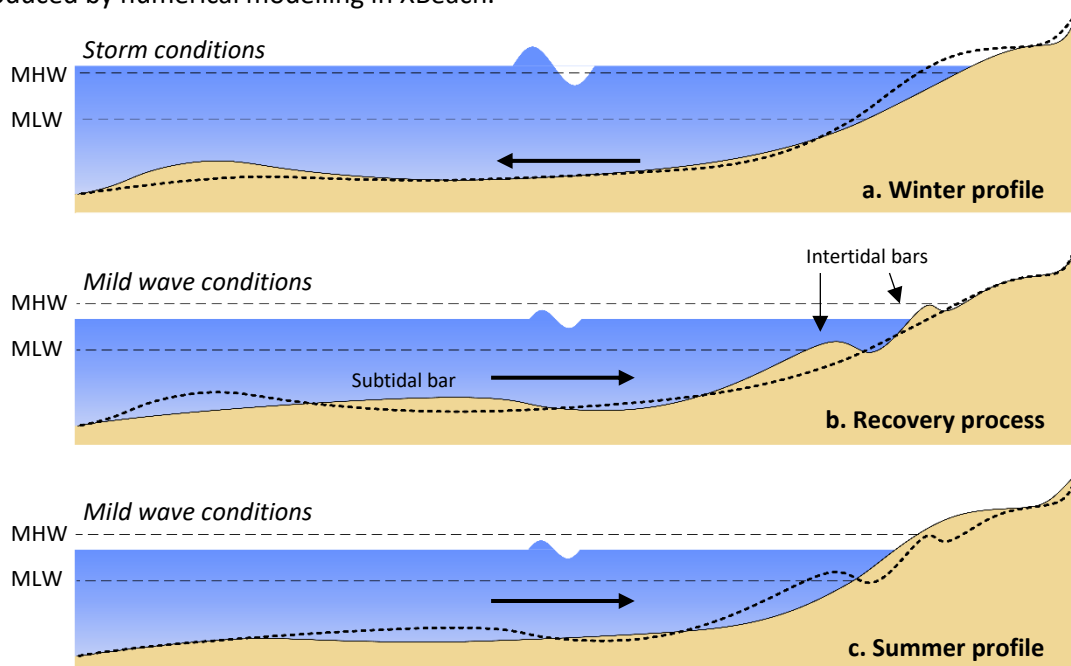


Figure 1-1: Cross-shore storm and seasonal variability from a winter profile (a), through recovery (b) to a summer profile (c).
MHW = Mean high water, MLW = Mean low water.

1.2. Problem definition

The recovery of the shoreline by migration of intertidal bars is a process including many mechanisms over multiple spatial and temporal scales (Cowell et al., 2003). This is resulting in a complex coastal behavior which is hard to measure and predict accurately on the engineering time scale (years to decades). To map and gain knowledge on the morphological changes, long term coastal measurements already exist since several decades. An example is the JARKUS (yearly coastal measurements), performed at the Dutch coast (Verhagen, 1990). These measurements, like most performed long term measurement campaigns, do not include the spatial and temporal detail of micro (mm – 100m) and mezzo (100m – km) scale mechanisms (Vos et al., 2017) which are important for the understanding and predictions on the engineering time scale.

1.2.1. Recent progress in measuring and modelling

Measuring with terrestrial laser scanning (TLS)

Recently, the CoastScan project was setup to provide measurements on both small and long spatial and temporal scales (Vos et al., 2017). A measuring campaign was setup at Kijkduin in the Netherlands, to monitor a kilometer of beach for up to 6 months. Hourly topography was obtained using a terrestrial laser scanner (TLS) with a quality at the centimeter range. These measurements enable to gain knowledge on the coastal morphological behavior over multiple spatial and temporal scales with the ultimate goal to increase the accuracy of current numerical models.

From the dataset obtained at Kijkduin, a relation was found between the intertidal bar behavior and the neap-spring tidal cycle (Hobbelen, 2018). Analogous to Kroon and Masselink (2002), the observations show onshore migration of intertidal bars with an increasing tidal range. The onshore migration and welding of intertidal bars is important for beach recovery (Houser, 2009) and is therefore examined further in this study.

Numerical modelling in XBeach

In recent decades process-based numerical models have been developed to predict nearshore morphological changes. Some examples are XBeach, Delft3D, Unibest-TC and MIKE. Research into the reproduction of intertidal sandbar dynamics in these numerical models is still limited and appear to be a difficult task, as recently showed in Cohn et al. (2019). XBeach has the advantages that it incorporates the most relevant processes for cross-shore sediment transport (Trouw et al., 2012), especially close to the waterline, and is therefore used in this thesis.

XBeach is a process-based numerical model that predicts the nearshore and coastal morphological change (Roelvink et al., 2009). It was originally developed to assess the natural coastal response during time-varying storm and hurricane conditions on the spatial scale of kilometers. Since then, a number of additional options have been implemented, allowing to choose which time-scales to resolve (Roelvink et al., 2018a).

In sum, the current knowledge on post-storm recovery by the migration of intertidal bars over multiple spatial and temporal scales is limited, resulting in unreliable long term predictions in numerical models such as XBeach.

1.3. Research questions

The main research question of this thesis is:

What is the cross-shore morphological behavior of intertidal bars at Kijkduin on a timescale of hours to weeks and to what extent can it be reproduced in XBeach?

Therefore, the beach recovery by intertidal bars is analyzed using the field measurements at Kijkduin and model simulations are performed in XBeach. The following sub-questions are formulated to answer the main research question in a stepwise manner:

- SQ 1: What are the dominant cross-shore sediment transport processes responsible for the dynamic behavior of sandbars in the intertidal zone found in literature?*
- SQ 2: What is the intertidal bar behavior during mild and energetic wave conditions found in the TLS measurements at Kijkduin and which sediment transport processes are responsible?*
- SQ 3: What is the performance of the XBeach model with respect to the TLS measurement results?*
- SQ 4: How can the intertidal bar behavior be described in a conceptual model?*

1.4. Thesis outline

To answer the research questions defined above, this thesis is divided into 7 chapters as depicted in Figure 1-2. This outline provides the basic structure of this report, centered on the TLS measurements (chapter 4) and XBeach modelling (chapter 5) of the intertidal bars observed at Kijkduin.

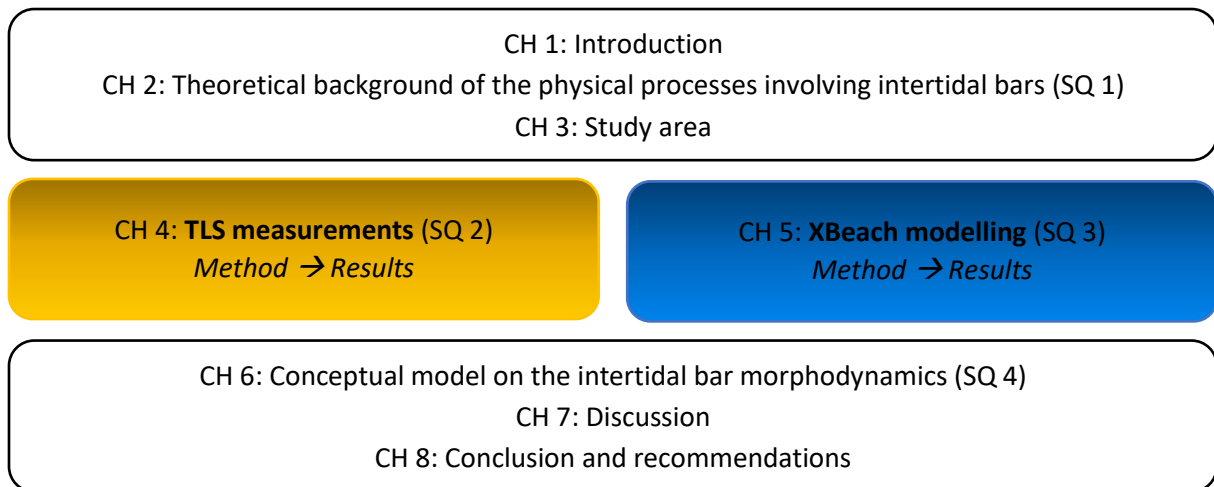


Figure 1-2: Basic thesis structure, divided into 7 chapters.

After this introduction, the coastal terminology used in this thesis is explained in chapter 2, followed by an explanation about cross-shore sediment transport processes and a literature review on intertidal bars. Based on this an initial conceptual model is constructed in a basic framework. The chapter concludes by answering the first sub-question (SQ 1). Subsequently, the study area of the measuring campaign is introduced in chapter 3. Besides the TLS measurements additional available data is listed that is used for the analyzes and the setup of the XBeach model.

In chapter 4, the method of collecting, selecting and processing the TLS measurement data is described in order to extract the necessary results. Two measuring periods are selected. Period A: both mild and energetic (storm) conditions and period B: only mild wave conditions. Furthermore, one cross section is chosen of which the cross-shore development is analyzed. This chapter concludes by answering sub-question 2 (SQ 2).

In chapter 5, two hydrodynamic models (the surf beat model and the hydrostatic swash model) of the numerical model XBeach are used to calculate the morphodynamics in period B (as described above). Firstly, the implementation of the dominant cross-shore sediment transport processes (explained in chapter 2) for both hydrodynamic models are described. Then, the setup of the models for the study area of Kijkduin are described, followed by the model results in which a comparison with the observations of the TLS measurements is made. The chapter concludes by answering sub-question 3 (SQ 3).

The literature review (chapter 2), TLS measurement results (chapter 4) and XBeach modelling results (chapter 5) are all combined to develop a conceptual model of the behavior of intertidal sandbars in chapter 6. Thus, sub-question 4 (SQ 4) is answered in this chapter. Subsequently, the TLS measurements results and the XBeach modelling results are discussed in chapter 7. Finally, an answer is given to the main research question in the conclusion, followed by recommendations for further research (chapter 8).

2. Theoretical background of the physical processes involving intertidal bars

The intertidal bar behavior is affected by a combination of physical processes. The theoretical background, involving the dominant processes on the behavior of intertidal bars, used in this study will therefore be described in this chapter. First, the coastal terminology found in literature and important in this study is formulated (section 2.1). Subsequently, the second section describes the important cross-shore processes responsible for sediment transport in the intertidal zone (section 2.2). In section three, a literature review on the behavior of intertidal bars is discussed (section 2.3). Based on this literature review and the cross-shore sediment transport processes an initial conceptual model on the behavior of intertidal bars is constructed (section 2.4). Finally, in part five, the chapter concludes by answering sub-question 1 (section 2.5).

2.1. Coastal terminology

2.1.1. The coastal region

The coastal region can be divided into areas with each their own characteristics. In literature several definitions for the coastal region can be found. Here the definitions described in Bosboom and Stive (2015) are followed. The coastal profile or shoreface is defined as the active nearshore zone affected by wave action (see Figure 2-1). It extends from water depths of 10 to 20 meters up to the beach and dune system. The shoreface can be divided into the lower shoreface, or shoaling zone, where wave amplitudes increase up to their breaking point and the upper shoreface consisting of the **surf zone**, **swash zone**, beach and the first dune row or cliff face. On the engineering time scale nearly all morphological changes take place at the upper shoreface.

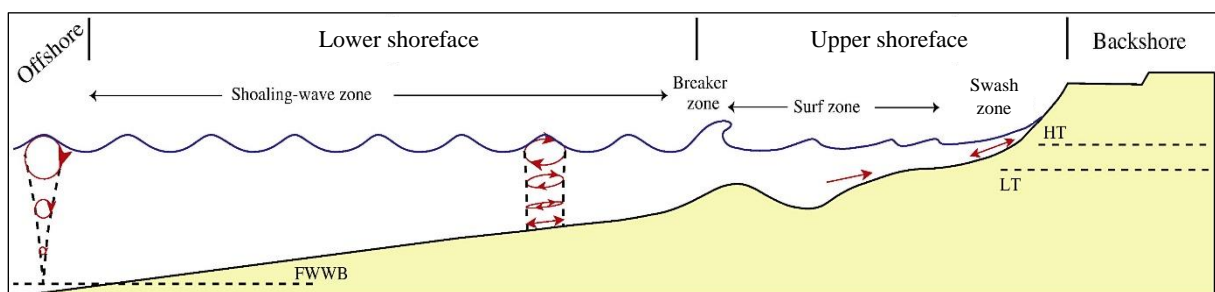


Figure 2-1: Schematization of the coastal region, including the positions of the various shoreface zones. Modified from Dashtgard et al. (2012).

The **intertidal zone** (part of the upper shoreface) is the transitional zone between water and land, emerged at low tidal water levels and submerged at high tidal water levels. This zone is therefore subject to both hydrodynamic and aeolian processes. The **swash zone** is also a transitional zone between water and land. Alternately being emerged and submerged on the timescale of wind waves and swell waves. This region between the wave runup and rundown level is often referred to as the beach face (Puleo et al., 2000). Due to changing tidal water levels, the surf zone and swash zone are shifting up and down the coastal profile, changing the active sediment transport processes (described in section 2.2) at one location in the intertidal zone.

2.1.2. Beach states

Wright and Short (1984) classified a series of beach states according to their appearance. Based on field studies on Australian beaches they distinguished six beach states, from fully dissipative to highly reflective beaches. In between, four intermediate states exist which contain both reflective and dissipative elements. Dissipative and reflective beaches are relatively two-dimensional, characterized by their cross-shore profile. Respectively, the beach states roughly correspond to winter and summer profiles, as shortly described in the introduction (section 1.1).

Dissipative beaches are characterized by a wide and flat sandy coastal zone with multi-barred surf zones. The sediment material is relatively fine and bed slopes between 0.01 and 0.02 are found. A dissipative beach is the result of high energy waves which contain spilling breakers. These high energy and short waves are typical for a storm wave climate (such as for the Dutch coast) and the associated variability results in a highly dynamic coastal profile (Bosboom and Stive, 2015).

Reflective beaches are characterized by a relatively steep and narrow beach face with a berm and a narrow surf zone without bars. The sediment material is relatively coarse and bed slopes between 0.1 and 0.2 are found. Reflective beaches typically contain collapsing or surging breakers corresponding to long and small amplitude waves. These beaches are the result of a period of mild wave conditions that transport sediment onshore (Bosboom and Stive, 2015).

To indicate the beach state the dimensionless fall velocity can be used (Wright and Short, 1984):

$$\Omega = \frac{H_b}{w_s T} \quad (2.1)$$

where H_b is the breaking wave height, w_s is the sediment settling velocity and T is the wave period. Reflective beaches typically have $\Omega < 1$, intermediate beaches $1 < \Omega < 6$ and dissipative beaches $\Omega > 6$.

The appearance of a certain beach can change over time and move through a series of beach states. The dimensionless fall velocity is used by Wright and Short (1984) to explain what response is expected. Mild wave conditions slowly force a beach towards a more reflective beach state through onshore sediment transport, whereas storm waves are responsible for fast offshore movement of sediment resulting in a more dissipative beach state (Bosboom and Stive, 2015).

2.1.3. Storm impact regimes

The classification of storm impact regimes, proposed by Sallenger (2000), is applied in this thesis for the construction of a conceptual model for intertidal bars (chapter 6). Sallenger (2000) categorized the impact of hurricanes to natural barrier islands in storm impact regimes. A division of four different regimes is based on the coupling between the forcing, in terms of the water levels, and the resistance, characterized by the dune geometry. The involved water levels are the runup level (R_{high}) and rundown level (R_{low}), including the astronomical tides and storm surges. The dune geometry is represented by

elevation of the dune crest (D_{high}) and dune foot (D_{low}). Using these parameters, the regimes are defined as follows:

1. **Swash regime:** $R_{high} < D_{low}$
The wave runup level remains below the dune foot.
2. **Collision regime:** $D_{high} > R_{high} > D_{low}$
The wave runup level is above the dune foot but below the dune crest.
3. **Overwash regime:** $R_{high} > D_{high}$ & $R_{low} < D_{high}$
The wave runup level is above the dune crest and the rundown level is below the dune crest.
4. **Inundation regime:** $R_{low} > D_{high}$
The wave rundown level is above the dune crest.

2.1.4. Sediment transport

Sediment transport is the movement of sediment particles defined over a certain period of time and through a vertical plane. In coastal engineering the sediment transport rates are often expressed in $m^3/m/s$ indicating the volumes of accretion and erosion. Considering the deposited volumes of sand with zero local gains or losses the sediment balance can be formulated as follows (Bosboom and Stive, 2015):

$$\frac{\partial z_b}{\partial t} + \frac{\partial S_x}{\partial x} + \frac{\partial S_y}{\partial y} = 0 \quad (2.2)$$

where,

z_b	Bed level	[m]
S_x	Sediment transport volume in the cross-shore direction (including pores)	[$m^3/m/s$]
S_y	Sediment transport volume in the longshore direction (including pores)	[$m^3/m/s$]

Sediment transport can be divided in bed load and suspended load transport. Sediment particles that are transported in a thin layer close to the bed is defined as bed load transport. These sediment particles migrate by rolling, sliding or jumping over the bed and are nearly continuously in contact with the bed. For shear stresses just above a critical value, single particles start migrating over the bed. At higher shear stresses, an entire layer of particles starts moving which is referred to as sheet flow. When the jumps become larger and the particle loose contact with the bed for some time they become part of the suspended load. The mechanism between the two types of sediment transport are different and transport formulations are therefore often separated (Bosboom and Stive, 2015).

Bed load transport is very much dependent on the bed shear stress acting on the sediment particles. Many approaches found in literature are therefore describing bed load transport as a function of the bed shear stress due to waves and currents. Often the shear stress is raised to a power of 1.5 to 2, for example in the formulation of Ribberink (1998). As the shear stress is quadratically related to the shear velocity and the velocity direction does not influence the sediment load, the bed load transport can be described by $\langle S_b \rangle \propto \langle u|u|^{n-1} \rangle$ with $n = 3$ to 4.

Sediment gets into suspension when the bed shear stress is larger than the critical bed shear stress and the upward forces are larger than the downward gravity force of the submerged weight of the particles. Assuming the suspended sediment responds instantaneous to the water motion, suspended sediment transport can be described by a function of the sediment concentration in the water column and the horizontal water velocity. The instantaneous velocity and concentration consist of a current related and wave related part. The current related part is often wave induced, for example undertow and streaming (described in Section 2.2). The wave related part is the transport by the oscillatory water

motion. Amongst others, in the Soulsby Van Rijn formulation (Soulsby, 1997) the wave related part is left out in the suspended sediment transport equation. Here, the wave related part is assumed to be small compared to the current related part and the contribution of the oscillatory velocity is thought to be accounted for in the bed load transport formulation.

In literature many formulations are found for sediment transport, both for sub-aqueous and aeolian transport. They are still largely empirical and often show large differences compared to actual measurements (Bosboom and Stive, 2015).

2.2. Cross-shore sediment transport processes

Cross-shore sediment transport is the transport in onshore or offshore direction and determines the coastal profile shape. As described in section 1.1, the coastal profile shape changes under the influence of the hydrodynamic conditions. These conditions drive cross-shore sediment transport processes determining if sediment is transported onshore or offshore. Sediment is transported predominantly from the point of wave breaking, in the surf zone and swash zone. The cross-shore sediment transport processes are described separately for the surf zone and swash zone in the two subsections below.

2.2.1. Surf zone processes

In the surf zone, under normal conditions a mixture of bed and suspended load is present in the water column mainly due to breaking induced **turbulence**. The total net cross-shore sediment transport is divided into three components: Wave nonlinearities (short wave **skewness** and **asymmetry**), mean transport due to the combination of steady flows (**Stokes drift**, **undertow** and **streaming**) and **infragravity waves** (Aagaard et al., 2013; Roelvink and Stive, 1989). These components together with the breaking induced turbulence are described below.

Wave nonlinearities (short wave skewness and asymmetry)

When waves propagate towards the coast, non-linear effects start to play an important role in wave-induced transport. Besides the change in wave height and length in the shoaling zone, waves also change in shape. From a sinusoidal type of wave in deep water, the wave crests gradually become higher and narrower while the trough is extending and flattens (see Figure 2-2). The result is an asymmetric shape relative to the horizontal axis called **skewness** (Grasmeijer, 2002). Wave skewness tends to cause net onshore directed transport of sediment due to skewed orbital velocities. However, boundary layer processes caused by, for example, bedforms may introduce phase lags between fluid velocity and sediment concentration (Aagaard et al., 2013). In some cases the phase lags are large enough to cause net transport opposite to the incoming waves, offshore directed (Osborne and Greenwood, 1993).

Subsequently, the waves show an **asymmetry** relative to the vertical axis. Steepening of the face resulting in a pitched forward and sawtooth-like shape is referred to as wave asymmetry (Elgar and Guza, 1985). Wave asymmetry contributes to onshore sediment transport due to skewed accelerations (Elgar et al., 2001).

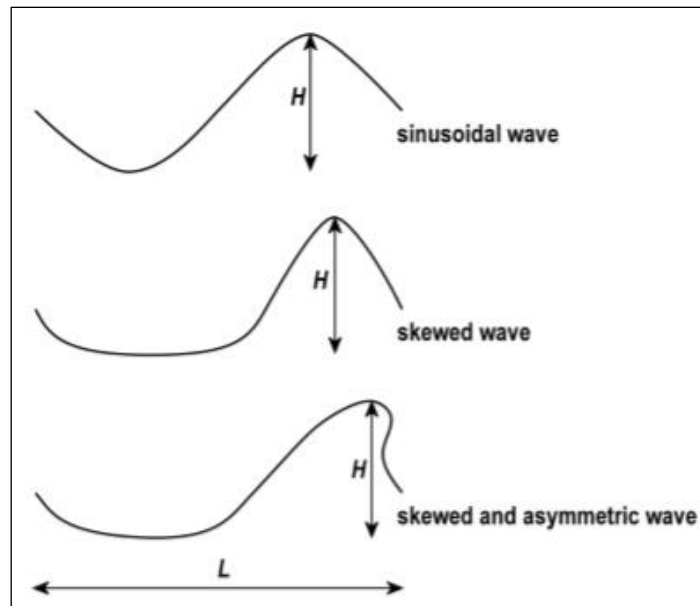


Figure 2-2: Wave skewness and asymmetry. From Grasmeijer (2002).

Mean transport (Stokes drift, undertow and streaming)

Under oscillatory waves, water particles do not describe a closed orbit due to the increase in horizontal orbital velocity with increasing distance from the bed. The water particle moves faster under the crest in the wave propagation direction and moves slower backward under the trough. As a result, there is a net onshore mass transport in the direction of the wave propagation. This is referred to as **Stokes drift**. The process increases in the shoaling zone as the wave amplitude increases and consequently decreases in the surf zone where the wave amplitude decreases (Bosboom and Stive, 2015; Walstra and Van Rijn, 2003).

For coastal situations, there is a zero net mass transport as the beach acts as a closed boundary. Therefore, there must be a return flow balancing the onshore directed Stokes drift (see Figure 2-3). In non-breaking waves the return flow is relatively small. In the surf zone, the mass transport is substantially larger between the wave crest and trough due to the additional roller energy of breaking waves. This results in large offshore directed velocities under the wave trough, referred to as the **undertow** (Svendsen, 1984). During storm conditions this return flow is larger due to higher waves. During these conditions this is considered to be the dominant offshore sediment transport process (Steetzel, 1993). The effect of the undertow on sediment transport is dominant over the effect of Stokes drift as sediment concentrations are generally relatively large close to the bed, decreasing with the distance from the bed.

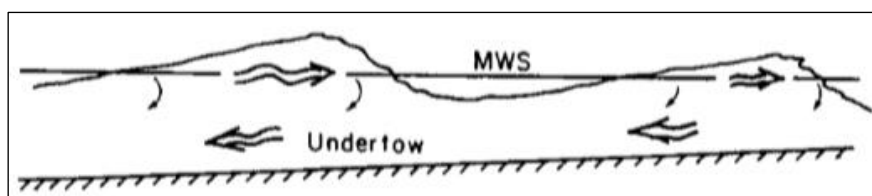


Figure 2-3: The undertow as a result of the onshore mass transport. From Svendsen (1984).

Close to the bed in the boundary layer, Longuet-Higgins (1953) demonstrated there is a **streaming** in the direction of the wave propagation, potentially transporting sediment in onshore direction. In non-breaking conditions (outside the surf zone) this boundary layer streaming is important to onshore sediment transport. However, in the surf zone where waves are breaking the undertow is dominant and the contribution of boundary layer streaming to sediment transport is negligible (Ruessink et al., 2007).

Infra-gravity waves

The third component of cross-shore sediment transport are the so-called **infra-gravity waves**. These waves are generated by variations in wave height in time and space, the wave groups. Waves carry momentum and the excess momentum flux due to waves is referred to as radiation stress. This radiation stress varies due to the wave height variation in wave groups. The result is a long (infra-gravity) wave motion on the wave group scale. Outside the surf zone the long wave is forced, traveling with the same length and speed of the wave group. This phenomenon is referred to as the bound long wave. For bound long waves the phase shift between the long wave and the short wave envelope of the wave group is in the order of π . In other words, the trough of the bound long wave coincides with the highest velocity in the wave group. This negative correlation causes an offshore sediment transport (Bosboom and Stive, 2015; Deigaard et al., 1999).

In the surf zone (where short waves are breaking) the bound long waves are released, travelling further as free long waves. The phase relationship between the long wave and short wave envelope may therefore change to a positive correlation resulting in onshore sediment transport (Roelvink and Stive, 1989).

Turbulence

Wave-breaking induced **turbulence** may stir sediment into the water column, which can then be advected by the previously mentioned components. When waves break in the surf zone they introduce a turbulent flow penetrating towards the bottom. As this turbulent flow reach the seabed it generates large shear stresses entraining the sediment from the bed (van Thiel de Vries et al., 2008).

2.2.2. Swash zone processes

The swash zone is a very dynamic region with large and rapid morphological variations (Puleo et al., 2000). To quantify the cross-shore sediment transport, the swash cycle is in literature separated into two phases. The uprush phase is the sediment transport during wave propagation up the beach face and backwash during the return flow down the slope of the beach face (Bakhtyar et al., 2009). A schematization of the swash cycle is depicted in Figure 2-4. In practice, the extent, duration and timing depend on the swash event, the characteristics of the bed material and the location in the swash zone. From Masselink and Puleo (2006b) some fundamental differences between the uprush and backwash phases of the swash flow can be distinguished and are described below, followed by a description on the forcing waves.

Turbulence

Wave-breaking induced **turbulence** is generally dominant during the uprush, whereas turbulent dissipation is dominant during the backwash phase which is the result of the formation of a boundary layer near the bed. Due to this process, sediment is mixed high into the water column during uprush where it is transported as suspended load, while sheet flow and bedload transport dominate during the backwash phase.

Groundwater flow (In- and exfiltration)

There is interaction between the swash motion and the beach groundwater level during a swash cycle. **Infiltration** (into the bed) occurs mainly during uprush and **exfiltration** (out of the bed) mainly during backwash. The amount of in- and exfiltration is strongly depending on the beach groundwater level, beach slope and sediment characteristics (Elfrink and Baldock, 2002). The in- and exfiltration behavior influence the sediment transport process. However, on sandy beaches their influence is relatively small.

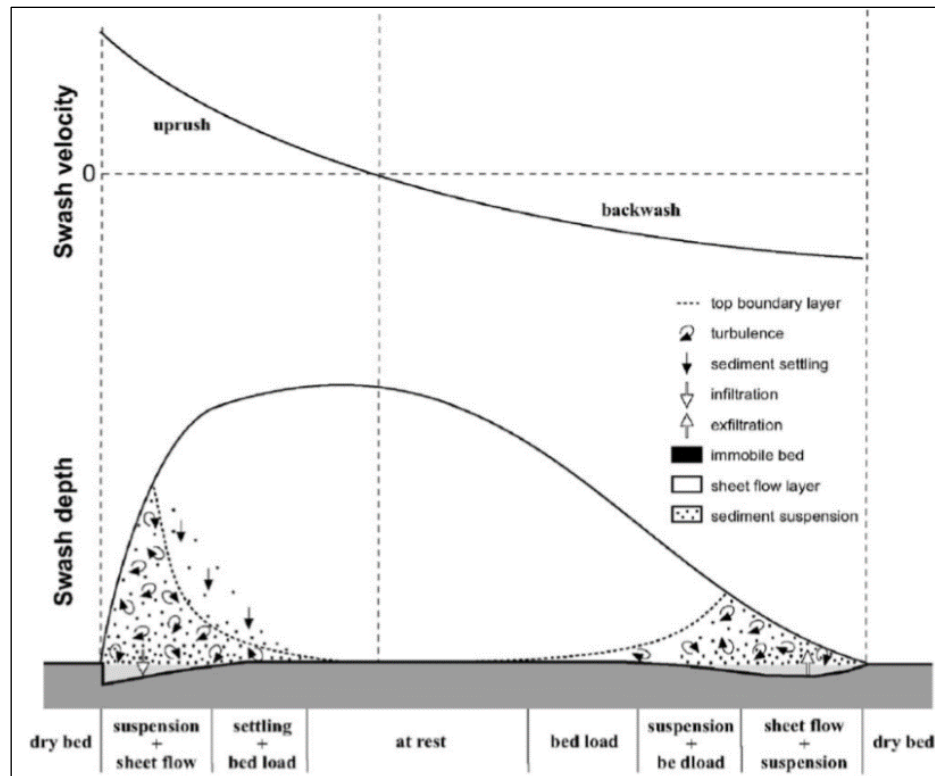


Figure 2-4: Schematic of sediment transport processes during a swash cycle. From Masselink and Puleo (2006b).

Gravity

In general, flow acceleration is less than **gravitational** acceleration throughout most of the swash duration. However, during the collapse of a wave bore a short burst of accelerating uprush can occur. Shear stresses tend to be larger during uprush than during backwash, but for a shorter duration. Flow velocities are similar between uprush and backwash, but flow durations are typically slightly longer during the backwash phase. As a result, the velocity skewness is directed offshore.

Forcing waves (short versus long waves)

The dominance of long (infra-gravity) wave motion over short (sea, swell) wave motion in the swash zone depends on a combination of the offshore wave conditions and local bathymetry. The dominance can roughly be determined by whether the surf zone is saturated or unsaturated (Elfrink and Baldock, 2002). In a saturated surf zone, the short wave height is limited by the local water depth. Typical for saturated dissipative beaches where generally energetic wave conditions prevail (as described in subsection 2.1.2), the swash zone may be expected to be dominated by non-breaking long waves (Elfrink and Baldock, 2002). During energetic conditions the short waves break in relatively deep water, increasing the dissipation length. Moreover, on the mildly sloping dissipative beaches the dissipation length is large. Therefore, short waves are predominantly dissipated by the time they are reaching the swash zone. For unsaturated surf zones on the contrary, short wave motions become more important, as short wave bores reach the shoreline (Wright and Short, 1984).

The dominance of the short versus long waves can be predicted by the surf similarity parameter (Masselink and Puleo, 2006b; Guza and Inman, 1975):

$$\epsilon_b = \frac{4\pi^2 H_b}{2gT^2 \tan^2 \beta} \quad (2.3)$$

where H_b is the breaking wave height, T is the incident wave period and $\tan\beta$ is the beach face slope. Infra-gravity motions are dominant for values of $\varepsilon_b > 20$ (indicating dissipative conditions), whereas short wave motions are dominant for values $\varepsilon_b < 2.5$ (indicating reflective conditions).

2.3. Literature review on intertidal bars

Sediment transport in the intertidal zone generally appears in the morphological form of intertidal bars (Houser, 2009). Their formation, migration and destruction are observed on many tidal beaches with a significant tidal range ($> 1\text{m}$). They are oriented parallel to the coast and located between the mean low and high water spring levels. Based on their morphology, the intertidal bar system can be divided into three main types (Masselink et al., 2006a):

1. **Slip-face bars (or swash bars)** occur on gentle beaches (intertidal slopes around 0.035) and can be compared to intermediate beach states, as described in subsection 2.1.2. They are characterized by a single intertidal bar with a seaward slope of 0.05 – 0.1 and a pronounced height, generally exceeding 1 meter. The onshore migration rates often exceed 1 meter per day.
2. **Low-amplitude ridges** occur on very gentle dissipative beaches (intertidal slopes around 0.02). They can have 2 to 6 intertidal bars with a seaward slope of 0.035 – 0.07 and heights between 0.5 and 1 meter. Their onshore migration rates rarely exceed 1 meter per day and are generally between 1 and 10 meters per month.
3. **Sand waves** occur on nearly horizontal, extremely dissipative beaches (intertidal slopes < 0.01). The number of bars may range from 4 to more than 10 intertidal bars with seaward slopes of 0.02 – 0.05 and heights below 0.5 meter. Sand waves appear to oscillate onshore and offshore about a mean point and do not migrate in one direction consistently.

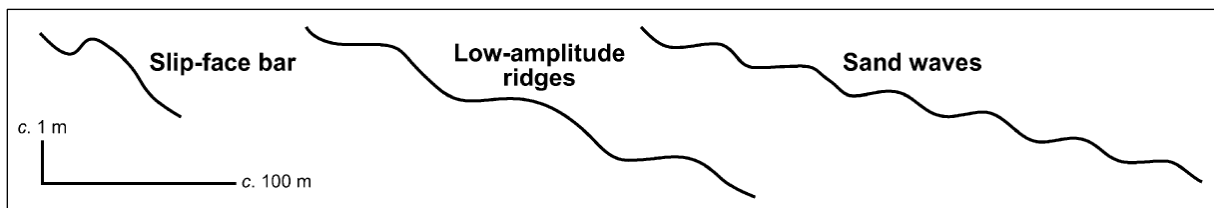


Figure 2-5: Three main intertidal bar types (Masselink et al., 2006a)

An overview of field studies on intertidal sandbars is presented in Table 2-1. Based on the morphological features and the hydrodynamic conditions the intertidal bars can be divided in the bar types described above. The morphological response of these intertidal bars primarily depend on the wave- and tidal conditions and are described below.

Wave conditions

The morphological response of intertidal bars forms a strong connection with the wave conditions. Generally, bars form and migrate onshore during mild wave conditions, and are destroyed and may migrate offshore during energetic (storm) conditions (Masselink et al., 2006a). However, the morphological response is affected by the relaxation time effects and morphological feedback (Cohn et al., 2017; Wijnberg and Kroon, 2002).

The formation, migration and destruction of the bars can be a result of both surf zone and swash zone processes (Masselink et al., 2006a; Kroon and Masselink, 2002). Surf zone processes can transport intertidal bars onshore when they are exposed to low-medium energy breaking waves (Sunamura and Takeda, 1984; Kroon and Masselink, 2002). Waves advancing over the sandbar crest transports sediment from the seaward to the landward side of the bar. Swash zone processes can also migrate bars

onshore. In this process, sediment is entrained at the seaward slope of the bar. Subsequently, uprush overtops the bar crest and sediment is deposited landward of the bar crest (Wijnberg and Kroon, 2002). Various theories are present on the formation of intertidal sandbars. According to Kroon (1994) a small ridge is formed near the low water level by swash zone processes, which develops further into an intertidal bar. However, other researchers link the formation of intertidal bars to surf zone processes (Kroon and Masselink, 2002). In energetic (storm) conditions, the offshore migration and destruction of intertidal bars mainly occurs in the surf zone, where large bed return flows (undertow) are present (Kroon, 1994; Houser and Greenwood, 2003).

Tidal conditions

The tidal variations are important for the cross-shore sediment transport processes as it shifts wave action up and down the beach profile, determining the position and duration of distinct wave action (Masselink et al., 2006a). Spring tides result in a large intertidal area and a small residence time for morphodynamic (cross-shore sediment transport) processes. In contrast, neap tide narrows the intertidal area and increases the time for morphodynamic processes to occur on one location (Kroon and Masselink, 2002). Therefore, morphological changes are potentially larger during neap tide.

Field study	Morphological features					Hydrodynamics		Bar type
	Stage	n_b	$\tan \beta$	B_h [m]	dx/dt [m/day]	Tide [m]	H_{m0} [m]	
Egmond beach, NL (Kroon, 1994)	F, M, D	1	-	1.0	$\sim +10$	1.5-2.0	1-6	1
Linden beach, Nova Scotia, CA (Dawson et al., 2002)	M	6	~ 0.004	0.5	$< -/+0.5$	1-2	0.5	3
Thedlethorpe beach, GB (Kroon and Masselink, 2002)	M	6	~ 0.015	0.5	+2	2.8-6.0	0.5	2
North Lincolnshire coast, GB (Van Houwelingen, 2004)	M	5	~ 0.015	0.6	$< +1$	3-6	-	2
Vejers beach, DK (Jensen et al., 2009)	F, M, D	1	~ 0.026	0.4	$\sim +12$	0.6-1.2	1-3	1
Newport, Oregon, US (Cohn et al., 2015)	M	1 to 2	-	1.0	+1.5	2.0-4.0	1-3	1
Oysterville, Washington, US (Cohn et al., 2017)	M	2	~ 0.015	1.2	+12	1.5-3.5	1-2	1

Table 2-1: Literature overview of intertidal bar field studies listed by publication year. Intertidal bar stages are separated into formation (F), migration (M) and destruction (D). The morphologic characteristics are furthermore defined by the number of intertidal bars (n_b), intertidal slope ($\tan \beta$), maximum intertidal bar height (B_h), migration rate of the bar crest (dx/dt) and the bar type (1. Slip face bar; 2. Low-amplitude ridges; 3. Sand waves). The hydrodynamics are described by the neap-spring tidal range (Tide) and the offshore wave conditions (H_{m0} and T_p).

2.4. Initial conceptual model

Based on the cross-shore sediment transport processes (section 2.2) and the literature review on intertidal bars (section 2.3) an initial conceptual model is developed to help visualize the behavior of an intertidal sandbar. As described in section 2.2, the cross-shore sediment transport processes can be divided into surf zone and swash zone processes. Within a tidal cycle, the dominance of these processes is related to the tidal water level with respect to the intertidal bar. For relatively low water levels, the swash zone processes are dominant, acting on the seaward slope and crest of the bar. With an increasing tidal level, the surf zone over the intertidal bar gets larger and its sediment transport processes become more important. Eventually, when the intertidal bar gets submerged, merely the surf zone processes act on the bar.

The wave energy approaching the coast can roughly be distinguished in mild and energetic wave conditions. These wave conditions have a strong connection to the morphological response. The morphological response of the combination of wave and tidal conditions are implemented in the conceptual model shown in Table 2-2. The formation and onshore migration (indicated in green) have a positive effect on the recovery of the coastal system, whereas the destruction and offshore migration (indicated in red) have a negative effect.

Intertidal bar dominated by:		Wave conditions	
		Mild	Energetic
Tidal level	HW ↑ Surf zone processes	Formation and/or onshore migration	Offshore bar migration and/or destruction
	LW ↓ Swash zone processes	Formation and/or onshore migration	Destruction

Table 2-2: Initial conceptual model on the intertidal bar behavior in response to the wave and tidal conditions.

This (initial) conceptual model is further extended in chapter 6, mainly based on the TLS measurements presented in chapter 4. Although significant research is performed to the morphological features of intertidal bars (Wijnberg and Kroon, 2002; Masselink et al., 2006a), a conceptual model has not yet been developed for its dynamic behavior. A conceptual model helps visualizing the complex behavior of intertidal bars. In this way, the understanding of the intertidal bar morphodynamics can be improved and processed based numerical models (such as XBeach) can further be developed. In this study, mainly the results of the TLS measurements (described in chapter 4), but also the XBeach modelling results (described in chapter 5) will support the development of a conceptual model on the intertidal sandbar behavior.

2.5. Conclusion

Based on this chapter an answer is given to sub-question 1, described below.

SQ1: What are the dominant cross-shore sediment transport processes responsible for the dynamic behavior of sandbars in the intertidal zone found in literature?

The dominant cross-shore sediment transport process in the intertidal zone are divided in surf zone and swash zone processes. In the surf zone the cross-shore sediment transport is primarily determined by the balance of wave nonlinearities (wave *skewness* and *asymmetry*), mean transport (*undertow*) and *infra-gravity waves*, provided that sediment is entrained into the water column by wave-breaking induced *turbulence*. In general, wave nonlinearities contribute to onshore sediment transport whereas undertow drives offshore sediment transport. Depending on the phase shift between the infra-gravity wave and short wave envelope, infra-gravity waves might contribute to either onshore- or offshore sediment transport.

In the swash zone the cross-shore sediment transport is determined by the balance between the uprush and backwash. Generally, the wave-breaking induced *turbulent* uprush and the *gravity* induced backwash transport sediment onshore and offshore respectively. However, the backwash can also transport sediment onshore when the uprush overtops the bar crest and sediment is transported further on the landward side. The swash zone dynamics can be forced by the oscillatory wave motions of short waves and long waves. The oscillatory wave motion prevailing in the swash zone (on the beach face) is depending on the offshore wave conditions and the local bathymetry. Short waves are generally dominant for mild wave conditions on a reflective beach, whereas long waves are dominant for energetic wave conditions on a dissipative beach.

The dominant processes driving intertidal bar morphodynamics largely depend on the tidal level and the wave conditions that prevail. For relatively low water levels with respect to an intertidal bar, the swash zone processes are dominant. With a rising tidal water level the surf zone processes become more important and ultimately dominant when the intertidal bar gets submerged. The balance of the above mentioned surf zone and swash zone processes determine the on- or offshore transport of sediment. Generally, onshore and offshore sediment transport occurs for mild and energetic wave conditions, respectively.

3. Study area

Before describing the TLS measurements (in chapter 4), first the study area of the measurement campaign is described in this chapter. Here, the coastal setting (section 3.1) and the available and relevant data (section 3.2) for the comparison with the XBeach model (chapter 5) are described.

3.1. Coastal setting

As part of the CoastScan project a measurement campaign was setup at Kijkduin, the Netherlands, in the period of November 2016 to May 2017. This coastal area, depicted in Figure 3-1, contains a sandy beach and a dune area. The average mean grain size, D_{50} , of the wet coastal area is $300 \mu\text{m}$ with a standard deviation of about $90 \mu\text{m}$ (Wijsman and Verduin, 2011). In the figure it can be seen that the Sand engine is located close to the study area. Since the Sand engine was constructed in 2011, the adjacent coast including the study area has been accreting, widening the beach (Luijendijk et al., 2017). Earlier constructed groins are largely covered by the accreted sand and are only partly emerged during low water. The influence of these structures is therefore expected to be minimal, especially for the cross-shore sediment transport processes.



Figure 3-1: Overview of the study area (white circle) including the Sand engine. Modified from Google Maps. Lower right image: The study area in the Netherlands, depicted by the blue circle. Two offshore wave data platforms, Europlatform (EUR) and IJmuiden Munitiestortplaats (MSP), are indicated in black. Modified from Rijksoverheid (2017).

The Dutch coast consists of a sand barrier system containing two to three bars (Short, 1992; Wijnberg and Kroon, 2002). The inner (intertidal) bar is mostly attached to the beach as a ridge and runnel, cut by drains and rips (visible in Figure 3-2 by the variability between the yellow and green areas). The beach itself has a rather uniform, concave upward sloping profile up to the beach berm and followed by the dune area. The beach berm is a relatively flat area on which local beach pavilions are located during the Spring and Summer period.

3.2. Available data

Next to the topographic data derived in the measurement campaign, additional topographic (above water) and bathymetric (under water) data is available. In September (6th – 9th) 2016, January (24th – 27th) 2017 and June (4th – 7th) 2017 bathymetry/topography surveys were done by Shore monitoring and Research. The survey of January 2017 (shown in Figure 3-2) is performed during the TLS measurement campaign and is therefore the main contributor for the bathymetry in the XBeach model (as will be shown in chapter 5).

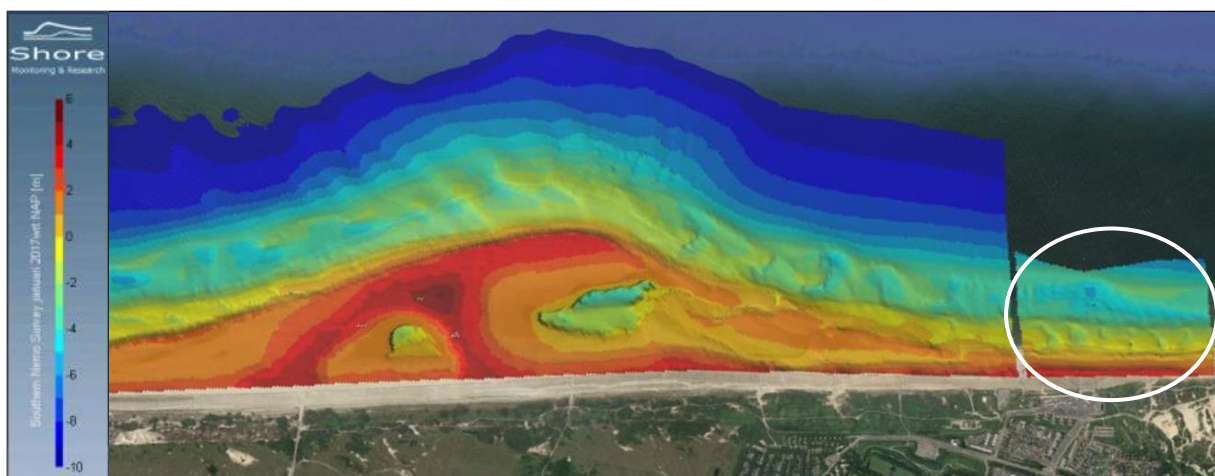


Figure 3-2: Bathymetry survey of January 2017. The white circle indicates the study area at Kijkduin. Modified from (Weger, 2017).

The study area is exposed to an episodic seasonal wave climate with a semi-diurnal tide. In the winter (Nov-Jan) the average offshore significant wave height is 1.7 m. Where small waves ($H_s < 1$ m) predominantly originate from the northwest, average waves ($1.5 \text{ m} < H_s < 3.5 \text{ m}$) from both the southwest and northwest and the highest waves ($H_s > 4.5 \text{ m}$) from the west and northwest (Luijendijk et al., 2017). Wave data including the wave height, direction and period is taken from the offshore Europlatform in the North Sea. This platform is located approximately 40 km of the coast of Goeree, as shown in Figure 3-1, where the water depth is 30m. The tide at Scheveningen (approximately 5 km northeast of Kijkduin) is semi-diurnal and has a spring/neap tidal range of 1.98/1.48 m. The tide is asymmetric with on average a rising period of 4 hours and 21 minutes and a falling period of about 8 hours. This causes asymmetric alongshore velocities with maximum flood (northeast directed) and ebb (southwest directed) tidal currents of respectively 0.7 m/s and 0.5 m/s (Luijendijk et al., 2017).

For the TLS measurement campaign at Kijkduin (which is described in chapter 4) additional bathymetric, wave and tidal data is required. An overview of this available and relevant data of the study area is presented in Table 3-1.

Measured parameter	Means	Frequency and/or period	Coverage
Topography	Terrestrial Laser Scanner (TLS)	Hourly, November 2016 to May 2017	Study area (Kijkduin), longshore stretch of ~2 km
Bathymetry and topography	GPS on Jetski and GPS/Echo sounder on quad bike	September (6 th – 9 th) 2016, January (24 th – 27 th) 2017 and June (4 th – 7 th) 2017	Sand Engine and study area
Wave data	Two offshore platforms	Continuous	Europlatform 3 (EUR; water depth h=30 m, ~40 km of the coast of Goeree) IJmuiden Munitiestortplaats (IJM MSP; h=24 m ~30 km of the coast of IJmuiden)
Tidal data	Tide gauge	Continuous	Located in Scheveningen Harbor (~5 km northeast of Kijkduin)

Table 3-1: Overview of the available data, relevant for the study area. Modified from Luijendijk et al. (2017).

4. TLS measurements

This chapter is divided in the methodology of the TLS measurements and the subsequent measurement results, described and shown in section 4.4. The methodology of the TLS measurement consist of the data collection (section 4.1), selection (section 4.2) and processing (section 4.3) of the measurement campaign at the study area of Kijkduin (described in the previous chapter). Finally, in section 4.5 sub-question 3 and 4 are answered.

4.1. Data collection

The aim of the measurement campaign was to use permanent laser scanning (PLS) to provide topographic measurements over multiple spatial and temporal scales (Vos et al., 2017). Permanent laser scanning is a form of terrestrial laser scanning where a laser scanner is permanently scanning the beach from the same position in a near continuous way. In this measurement campaign, the topography of a kilometre of beach and dune area was measured in the period of November 2016 to May 2017. Every hour a scan was taken to obtain detailed information on the morphological changes of the study area. For the laser scanner it is not possible to penetrate through the turbid seawater. Therefore, only the emerged area of the beach is measured. The laser scanner was positioned on top of a hotel building, offering a clear view on the coastal study area. To take accurate scans, the laser scanner was mounted on a stable measuring frame and protected by a housing (see Figure 4-1a).

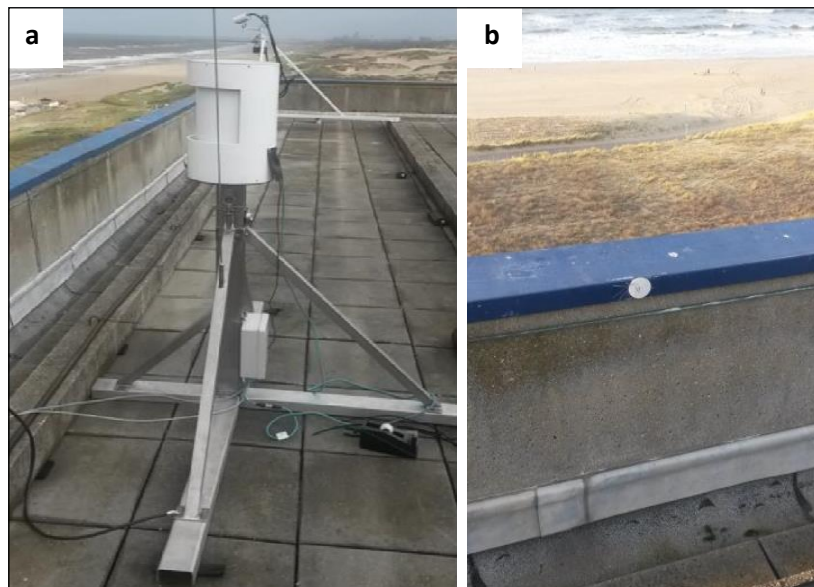


Figure 4-1: Laser scanner setup on top of the NH Hotel Atlantic Den Haag (a). A reference point on the roof in front of the laser scanner (b)). From Vos et al. (2017).

The scans taken by the laser scanner are related to the coordinate system of the laser scanner itself, with its origin at the scanner's center. To relate the scans to the national coordinate system, referred to as Geo-Referencing, five reference points are used which are visible on the scans. As an example, one of these reference points is visible in Figure 4-1b. The scans are taken over a horizontal field of view of 180 degrees. This window provides the required data of the region of interest (the coastal area) but leaves out unwanted areas to diminish the data size. The reference points are spread over the field of view, shown in Figure 4-2. Initially, three points are located on the roof of the hotel building (green points in Figure 4-2) and two in the dune area (red points in Figure 4-2). The location of these reference points was measured accurately using a Leica Viva GS10/GS14 GPS. Further details on the laser scanner are described in Appendix A of this thesis.



Figure 4-2: Overview of the study area with the position of the laser scanner and the reference points. The green points are clearly visible in the scans while the red points are not. Yellow points are additional points, used for correction (see subsection 4.3.1 on transformation and corrections).

4.2. Data selection

A temporal and spatial selection of the collected data is made, which is analyzed in section 4.4 and used to compare with XBeach results in section 5.3. Hourly topography of a kilometre of beach and dune area is collected for a period of approximately 6 months, as described above. Not all data of this large dataset is required for the analyses and comparison. Therefore, a selection in time and space is chosen, reducing the computational effort. The data selection in time and space is described below in two subsections.

4.2.1. Period selection

Period A (mild- and storm conditions)

In period A, from January 15 to February 28, 2017, a selection of 82 low water scans is used to analyze a period of mild wave conditions followed by a storm (as shown in Figure 4-3). The cross-shore intertidal bar behavior is different for both conditions, as discussed in chapter 2. Therefore, both conditions are included in the selected data. Starting with the first scan at 13 hours on January 15, 2017, this period counts 86 low water periods. During 4 low water periods the scans were not available or the quality was not satisfactory (as listed in Table 4-1).

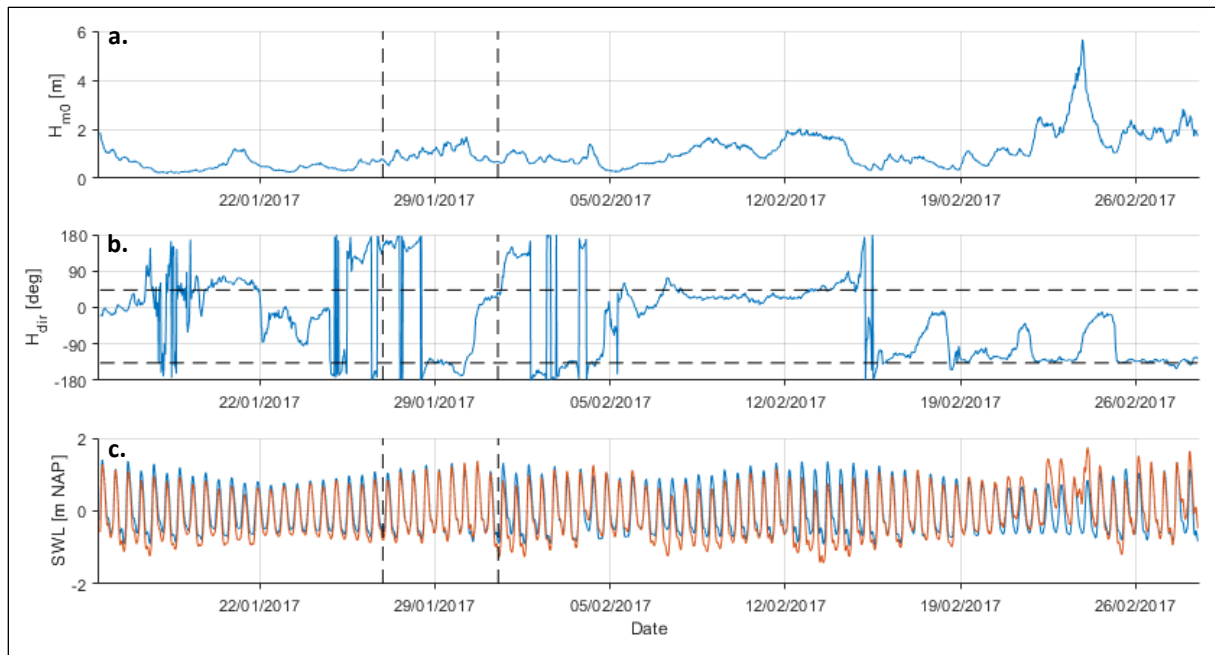


Figure 4-3: Significant wave heights (a), Mean wave directions (b) and still water levels (c) in period A (January 15 to February 28, 2017). The vertical dashed lines indicate period B (January 26 to 31, 2017). The horizontal dashed lines in figure b indicate the minimum and maximum angles of the domain. In figure c, the blue line is the astronomical tidal level and the red line includes the surge level.

Missing low water	Reason
24/01/2017 (~20h)	Bad quality, probably mist (high humidity)
18/02/2017 (~03h)	Bad quality, probably mist (high humidity)
22/02/2017 (~06h)	No scans taken (bug)
22/02/2017 (~19h)	No scans taken (bug)

Table 4-1: Missing low waters in period A (January 15 to February 27, 2017).

Period B (onshore intertidal bar migration)

In period B, from January 26 to 31 of January a selection of 110 scans is used to analyze a strong on-shore intertidal bar migration and compare it with XBeach results. Two scans from the 112 hourly scans are not usable due to a lack of range of the scans (as listed in Table 4-2). During period B, mild wave conditions are prevailing with an increasing tidal range, as depicted between the vertical dashed lines in Figure 4-3.

Missing scans	Reason
27/01/2017, 06h	Short range (bug)
27/01/2017, 10h	Short range (bug)

Table 4-2: Missing scans in period B (January 26 to 31, 2017).

4.2.2. Cross section selection

For the periods A & B, one cross section is selected based on a combination of the bathymetry survey in January 2017 and the scan of January 26 at 22 hours, depicted by c1 in Figure 4-4. The results of cross sections 2 and 3 (c2 and c3) are shown in appendix B. The left figure shows the actual orientation of the study area in RD-coordinates. For convenience, the study area is rotated (right figure) such that the longshore distance is aligned with the x-axis and the cross-shore distance with the y-axis. At a cross-shore distance of 100 m and between longshore distances of 400 m and 800 m an intertidal sandbar is growing and migrating onshore during period B. Furthermore, around a cross-shore distance of 150 m two distinctive intertidal sandbars, located at cross sections 1 and 3 (c1 and c3), are disrupted by a rip

channel, located at cross section 2 (c2). Cross sections 1 and 3 are located at the center of the two intertidal sandbars, where longshore changes are expected to be minimal. Moreover, cross section 1 is located relatively far away from the subtidal trough ($x \approx 300\text{m}$, $y \approx 400\text{m}$) which might influence the cross-shore intertidal behavior. In this case the cross-shore development of cross section 1 is analyzed and compared with XBeach results.

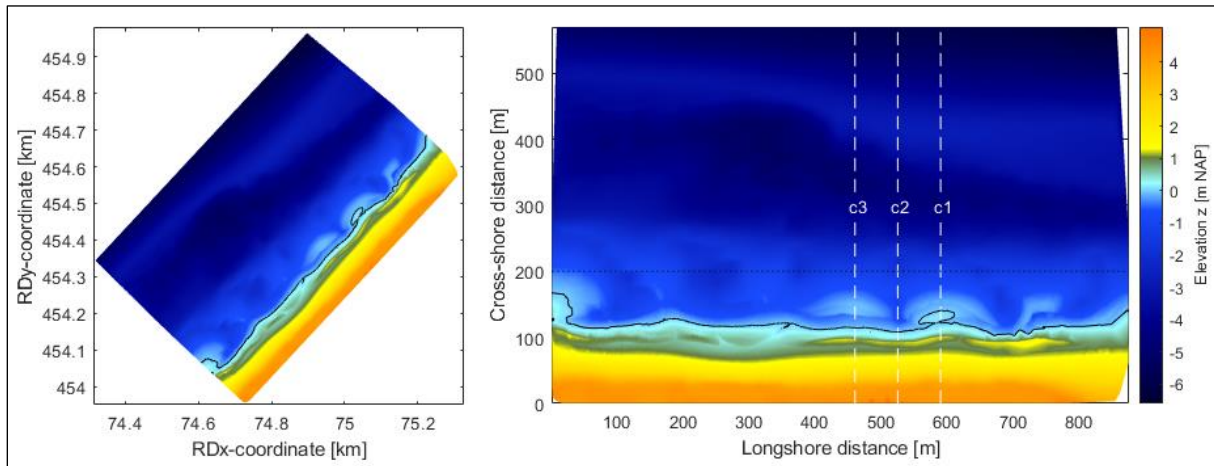


Figure 4-4: Bathymetry top view of the study area in RD-coordinates (left) and cross- and longshore distances (right), from a combination of the survey in January 2017 and the scan of January 26 at 22 hours. The white dashed lines indicate the longshore position of cross sections 1, 2 and 3. The black dotted line indicates the maximum offshore range of the TLS measurements. The black solid line indicates the +0 m NAP elevation contour.

4.3. Data processing

To obtain reliable representations of the measurements the raw data need to be processed. The raw data consist of point clouds such as depicted in Figure 4-5. In this figure it can be observed that the point clouds consist of more than the beach area only. Buildings, pavements, a dune area, waterbodies and more noise and unwanted objects are polluting the point clouds. Therefore, the data needs to be processed. In the following subsections six processing steps are elaborated, containing the steps listed in Figure 4-6.

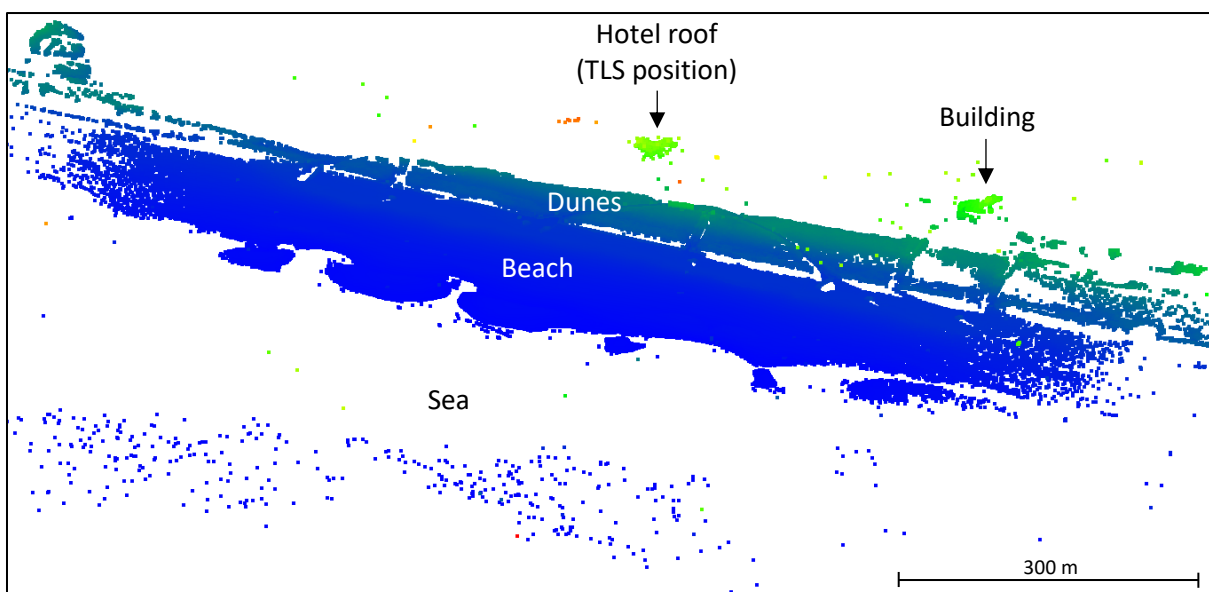


Figure 4-5: Example of a single scan at the beach of Kijkduin, from an offshore perspective. Colors indicate the relative height of the points, scaling from low to high (blue->green->yellow->red).

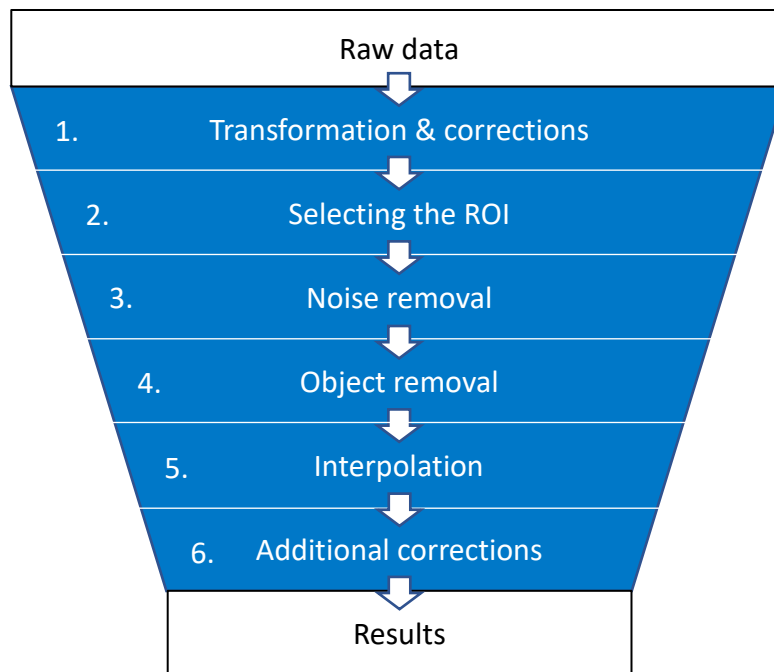


Figure 4-6: Data processing steps, to get from the collected raw data to the results.

4.3.1. Transformation and corrections

The raw data consist of point clouds in the form of range and rotational files related to the laser scanner. To transform these files to the national coordinate system, a transformation matrix is applied (Adopted from S.E. Vos) using the GPS measured reference points.

In the research of Hobbelen (2018) it appeared that some of the scans contain rotation errors. Visible as vertical deviations between subsequent scans the discrepancy increases with increasing distance from the laser scanner. Occasionally the vertical deviation between two subsequent low water scans exceed 10 cm at the foot of the dune area. Here, well above the water level, the deviations cannot occur by natural processes in such a short notice. Therefore, it can be concluded that the deviations are caused by errors in the rotational orientation of the laser scanner in the national coordinate system.

In an attempt to correct for the errors, three additional reference points are used (yellow points in Figure 4-2). In this way the orientation of the laser scanner in the national coordinate system can be positioned more accurately.

4.3.2. Selecting the ROI

By selecting the ROI (region of interest) the amount of points of a point cloud can be reduced significantly reducing the computational time for the following processing steps. Before selecting the ROI, a point cloud typically consists of around 3 million points. The vast majority of these points represent the hotel roof (~75%) and the dune area (~15%). These parts, together with the low point density longshore edges of the beach are excluded for further processing. An example of a point cloud with the selected ROI is shown in Figure 4-7. The selected ROI is a cubical shape, limiting both a horizontal and vertical area. Some points inside the square are excluded from the region of interest (red points) as they are located outside the vertical limitations.

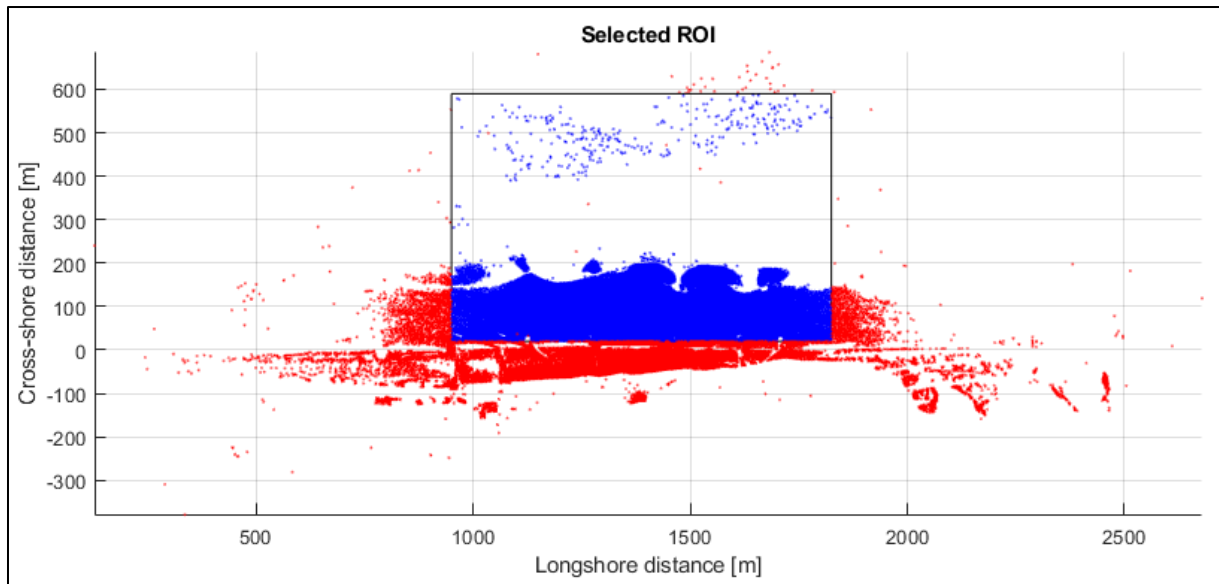


Figure 4-7: The selected region of interest represented in blue. Red points are eliminated for further processing. Scan 20/01/2017 at 5 pm.

4.3.3. Noise removal

The cropped point clouds contain noise, which primarily consist of seawater. This noise needs to be filtered and can be done with several methods. Here, LASnoise (developed by Isenburg (2018)) and the function 'pcdenoise' (available in Matlab) were applied. The methods both use the 3D point density of the point cloud as a filtering measure.

LASnoise

LASnoise is a tool which removes noise points in LiDAR data based on its isolation (Isenburg, 2018), both in horizontal and vertical direction. The tool removes points that only have a few points in its surrounding 3 by 3 by 3 grid cells. The size of the 27 grid cells and the threshold of points inside these grid cells can be set. When a point has less points in its surrounding grid cells than the set threshold, it is denoted as a noise point and will be removed.

It is difficult to find the optimal grid size and threshold of points as there is overlap between removed noise points and retained good points. Therefore, LASnoise is run twice. In the first run a relatively large grid size and threshold is used to remove the gross outliers. Subsequently, a smaller grid size and threshold is used in order to remove the left over noise points. By running LASnoise twice the vast majority of the noise points can be removed without removing too much good points. However, the removal of some of the good points cannot be prevented. Especially, on the longshore edges of the region of interest where the point density is low and boundary effects occur.

pcdenoise

The function pcdnoise filters outliers based on the distance of each point to its nearest neighbors in the 3D space (Rusu et al., 2008). In the function, the mean μ and standard deviation σ of nearest neighbor distances are computed. Subsequently, a point is filtered when the mean distance to its k nearest neighbors μ_k is outside $\mu \pm \alpha \cdot \sigma$. The number of nearest neighbors k and the threshold α determine which points are filtered. Pcdnoise is run twice, again to optimize the balance between the removal of noise points and retaining of good points.

The performance of LASnoise and pcdnoise is compared using both a scan with a high and low amount of noise. These scans are selected based on a visual inspection of the amount of water points close to the beach. From the results, presented in Figure 4-8 and Table 4-3, it can be concluded that LASnoise

performs best. Although LASnoise removes more good points for the scan on 15/01/2017 it also removes more noise points. For the scan on 27/01/2017 LASnoise performs much better as the percentage of filtered points in this low noise level scan is significantly lower. Moreover, pcdnoise has a higher filter percentage on the low noise scan than on the high noise scan which should be the other way around.

	Total points (before noise removal)	LASnoise		Pcdnoise	
		Points filtered	Percentage filtered	Points filtered	Percentage filtered
High noise level, scan 15/01/2017	234,774	4,526 (3,925 + 601)	1.9 %	2,005 (206+1,799)	0.9 %
Low noise level, scan 27/01/2017	252,884	3,510 (2,693 + 817)	1.4 %	6,396 (2,792+3,604)	2.5 %

Table 4-3: Comparison on the amount of filtered points by LASnoise and pcdnoise, for both a high noise and low noise level scan. The filtered points within the brackets represent the filtered points in respectively the first and second iteration.

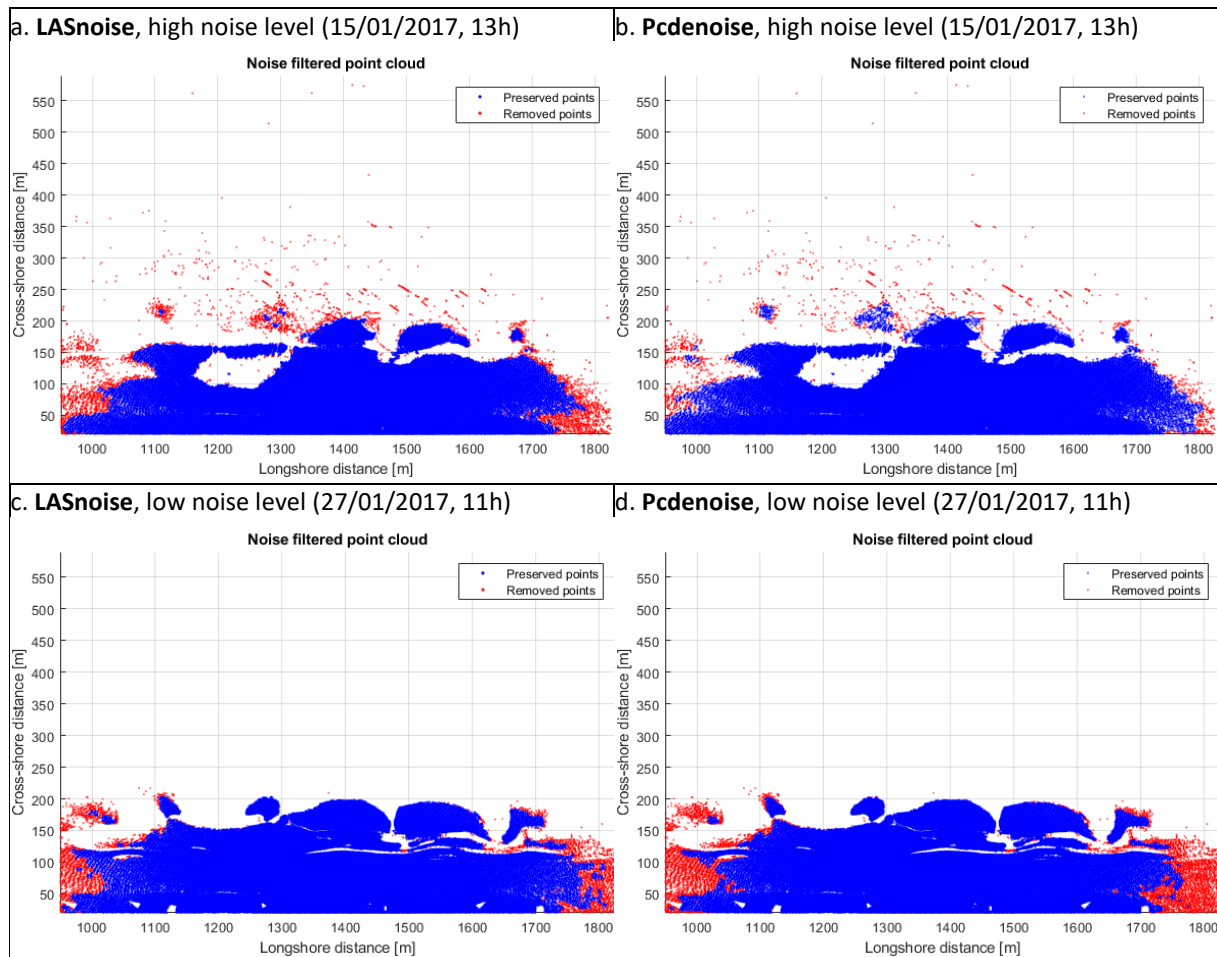


Figure 4-8: Comparison on the amount of filtered points by LASnoise and pcdnoise, for both a high noise and low noise level scan.

4.3.4. Object removal

After noise filtering the scans still contain unwanted objects like people, bins, poles and even a bulldozer. To get rid of these objects the tool LASground is used, developed by Isenburg (2018). This tool is based on the progressive morphological filter developed by Zhang et al. (2003).

In this case a grid is placed over the point cloud with the initial step size (or window size) of 2 meters. Within each grid cell the lowest point is classified as a ground point. However, when a point is located significantly lower than the lowest point of the neighboring grid cells (in this case 1 m), that point is classified as a non-ground point and removed. A triangulation is made of all the lowest points forming the initial ground terrain. Subsequently this step is repeated several times for a slightly shifted grid. Each iteration a different point might become the lowest point in a grid. In this way a first, rather coarse, ground estimate is made. The next step is to refine this estimate by defining the maximum bulge that is allowed between the ground estimate points. In this case it is set to 0.4 m, allowing for a gently sloping surface. In Figure 4-9a and b an example is shown of an object filtered point cloud using LASground.

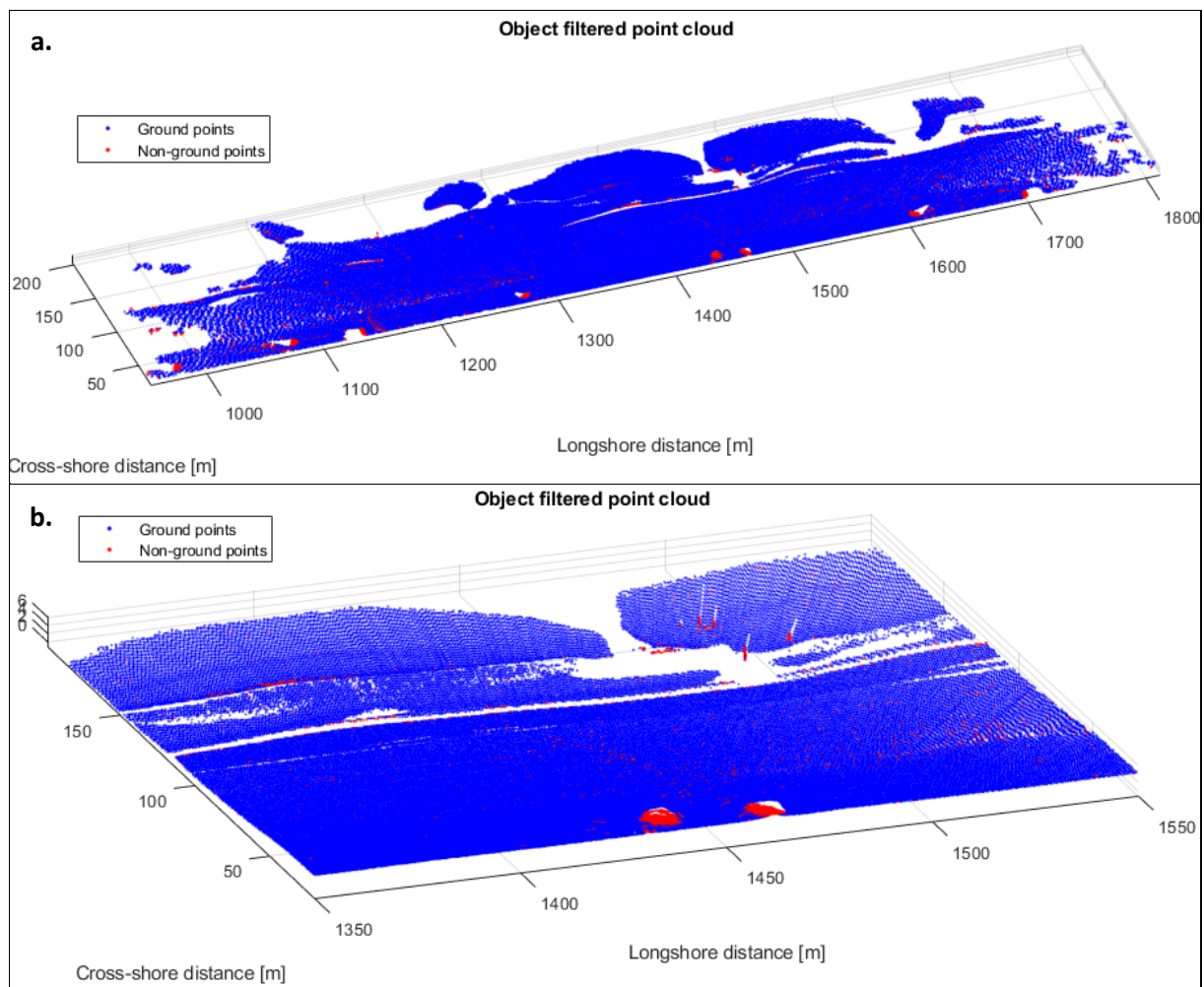


Figure 4-9: A 3D overview (a) and zoomed-in (b) example of an object filtered point cloud. Scan 27/01/2017, 11h.

4.3.5. Interpolation

Now the point clouds are filtered, they are interpolated to create a surface area. Using a meshgrid with a grid size of 0.5 m by 0.5 m the point clouds are linearly interpolated. In general, the point density ranges from approximately 1 point/m² on the offshore edge (near the coastline) to 5 points/m² on the beach berm (at the dune foot). The chosen grid size therefore provides good detail of the study area while diminishing the computational effort.

The intertidal bar behavior is studied in cross-shore direction. Therefore, cross sections are taken and only small longshore stretches are interpolated. This diminishes the computational time.

Interpolation might induce errors in areas with no detected points. Runnels for example, might drain water preventing the area to be detected by the laser scanner. As no points are detected, the area is interpolated by the ridge and beach face on respectively the offshore and onshore side of the runnel. Consequently, the bathymetry at the runnel is shifted upwards erroneously.

4.3.6. Additional corrections

Next to initial corrections of the scans, as described in step 1, additional corrections are performed to increase the precision of the results based on the data selection in subsection 4.2. In the cross-shore stretches with negligible hydrodynamic and human activity, the vertical deviation of subsequent scans is significant. Even after the initial corrections. This indicates that measuring errors are still clearly present in the processed data. For qualitative analyses in the intertidal area these errors are not obstructive. However, quantitative results may be affected significantly. Therefore, additional corrections are made for the selected periods A and B. For these two periods the additional corrections are described below for cross section 1 (from which the same method can be applied on the other cross sections).

Period A (mild- and storm period)

In period A, a cross-shore stretch of 12m is used for a better fit of the scans. The blue line in Figure 4-10 shows the vertical deviation for all 82 scans. In the cross-shore stretch between the dashed lines (from $x = 42\text{m}$ to $x = 54\text{m}$) the vertical deviation is relatively small. Higher in the profile ($x < 42\text{m}$) manmade elevation changes are induced. Bulldozers relocated sand from the dune foot into offshore directions at the beach (Anders et al., in press). Lower in the profile ($x > 54\text{m}$) hydrodynamic activity resulted in elevation changes. At the end of the period storm conditions caused elevation changes relatively high in the cross-shore profile. Therefore, only the small cross-shore stretch between the human and hydrodynamic activity can be used for correction.

A better fit is obtained by a vertical translation for all scans. The correction of the scan is based on the mean bed profile of all 82 scans along the 12m transect. Each scan is translated vertically with the mean deviation to the mean bed profile. The vertical translation is ranging from -1.1cm to +6cm as shown in Figure 4-11. Subsequently, the vertical deviation of all scans is reduced significantly as shown in Figure 4-10. It can be seen that the main changes are located in the higher part of the beach profile.

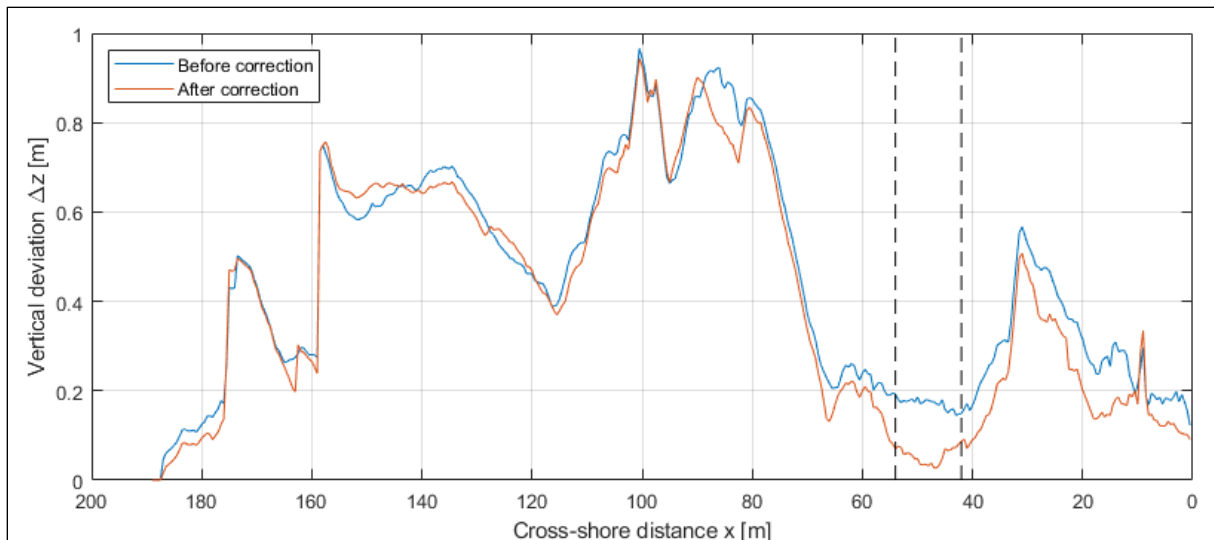


Figure 4-10: Vertical deviations along a cross section for the period from 15/01/2017 until 28/02/2017. The black dashed lines indicate the cross-shore stretch along which the scans are averaged ($x = 42\text{m}$ to $x = 54\text{m}$).

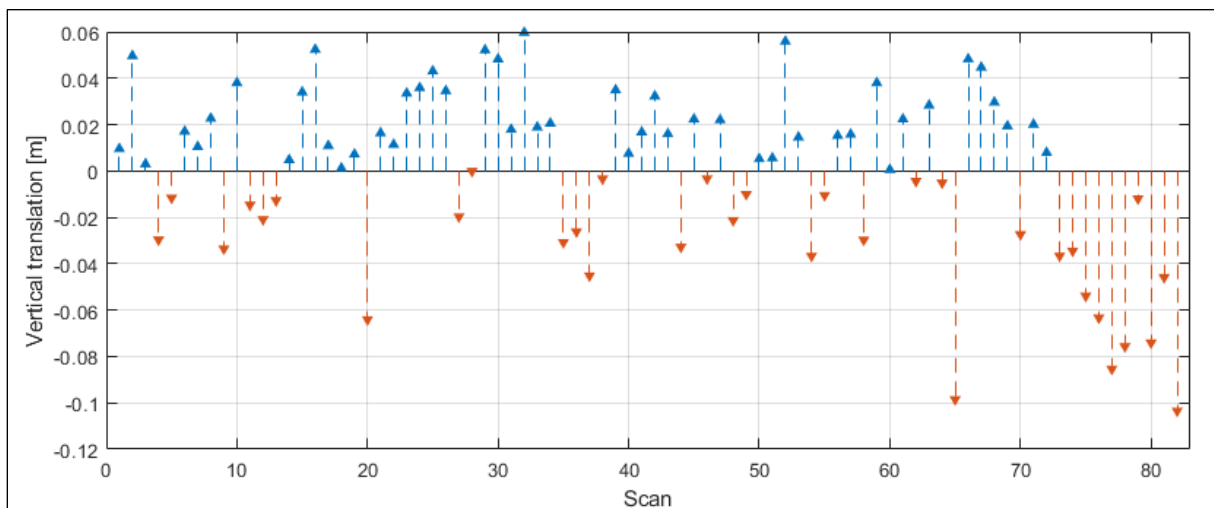


Figure 4-11: Vertical translation for each scan to get a best fit.

Period B (onshore intertidal bar migration)

In period B a cross-shore stretch of 65m is used for a better fit of the scans. The blue line in Figure 4-12 shows the vertical deviation for all 104 scans. In this period no significant manmade elevation changes are present. Moreover, the highest water level is relatively low compared to period A. This results in a larger cross-shore stretch that can be used for the correction.

A better fit of the scans is obtained based on a linear least squares approach. The 65m cross-shore stretch is long enough to provide a reliable linear trend for the linear least squares approach. Calculating the linear least squared estimates results in a regression line for each scan. These lines containing a rotation and vertical translation with respect to the onshore boundary of the domain. The regression lines are presented in Figure 4-13 by means of their standard deviation as a function of the cross-shore distance. The position of the laser scanner is located at the right boundary ($x = -136\text{m}$). At a distance of 136m from the onshore boundary of the domain ($x = 0\text{m}$). The standard deviation is minimal near that cross-shore position of the laser scanner. Therefore, it might be concluded that the vertical deviations are closely related to the cross-shore distance to the laser scanner. After rotating and translating the scans, the vertical deviation is reduced significantly.

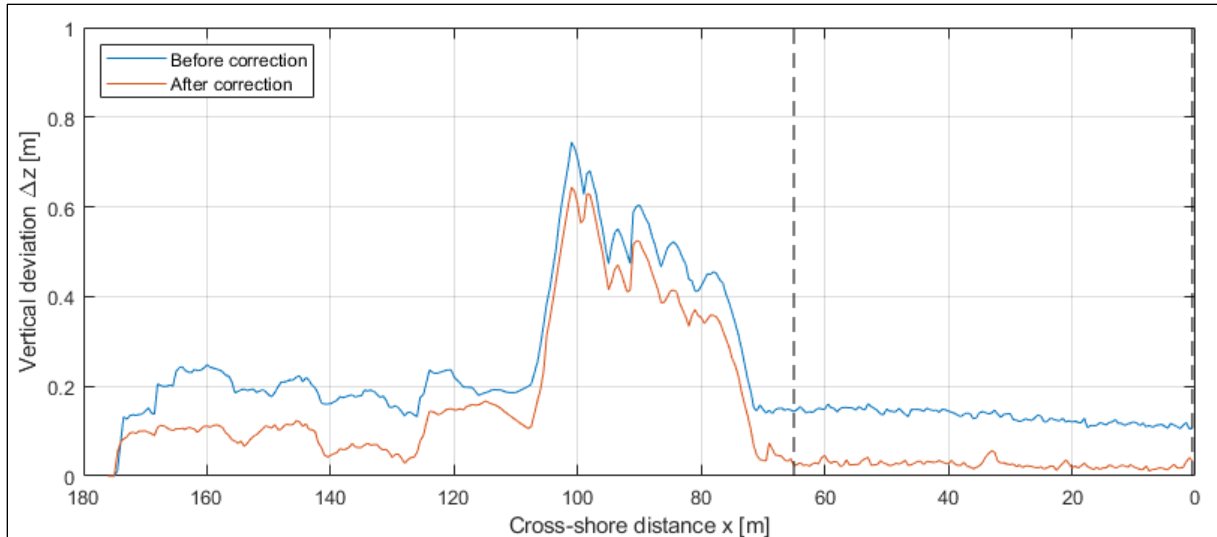


Figure 4-12: Vertical deviations along a cross section for the period from 26/01/2017 until 31/01/2017. The black dashed lines indicate the cross-shore stretch along which the scans are averaged ($x = 0.5\text{m}$ to $x = 65\text{m}$).

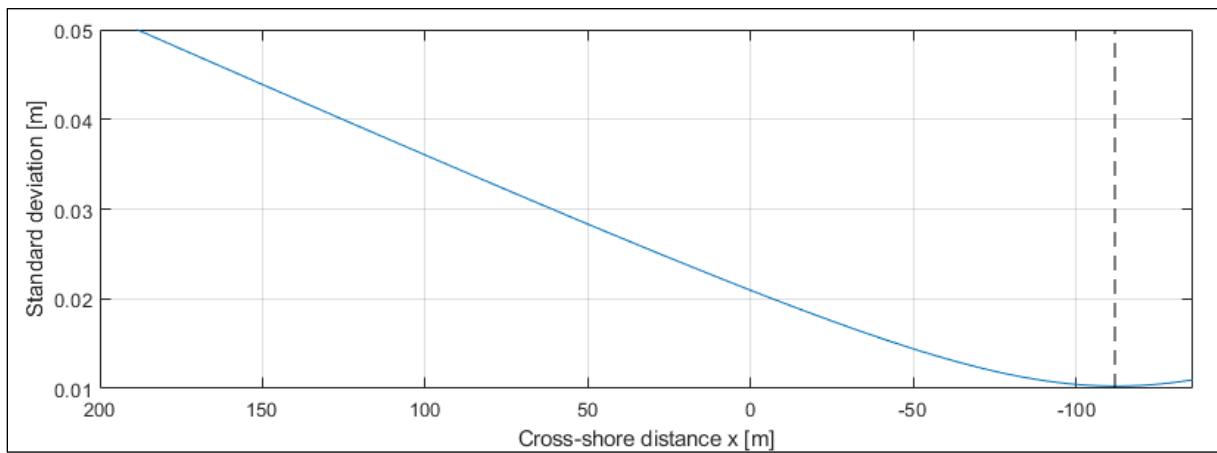


Figure 4-13: Standard deviation of the regression lines obtained in a linear least squares approach. The dashed line indicates the minimal standard deviation, located close to the cross-shore position of the laser scanner (at the right boundary).

4.4. Results

With the collected, selected and processed data described above, the results of cross section 1 can be extracted. This section is divided in the cross-shore development of period A and B. First the qualitative development of period A is analyzed. Subsequently, period B is analyzed in more detail describing both the qualitative and quantitative development of cross section 1.

4.4.1. Period A (mild- and storm period)

Bed level development

At cross section 1 two distinctive intertidal sandbars develop, grow and migrate in cross-shore direction during the period from January 15 to February 28, 2017 as shown in Figure 4-14 and Figure 4-15. In Figure 4-14, all 82 low water bed levels are shown in a 3D view. Figure 4-15 shows a selection of seven low water bed levels between which distinctive changes are observed. Initially the bed level shows a relatively smooth parabolic shape from the low water line up to the berm near the foot of the dune. At the offshore boundary a small intertidal bar starts developing. Over time, the crest of the bar moves onshore over a distance of 50m ($x = 170\text{m}$ to $x = 120\text{m}$) raising with a height of 0.7m (-0.3m to $+0.4\text{m}$ NAP) as indicated by the dashed arrow.

Higher in the profile a more pronounced intertidal sandbar develops. The development of this sandbar is indicated by the arrows and with numbers 1 to 4 in Figure 4-15. From an initially small perturbation, the sandbar develops quickly in about 5 days (arrow 1). Its vertical movement in particular, raising with a height of 0.7m ($+0.5\text{m}$ to $+1.2\text{m}$ NAP) while it moves onshore over a distance of 10m ($x = 110\text{m}$ to $x = 100\text{m}$). Hereafter in about the same time interval (arrow 2), the crest experiences a fast onshore movement of 25m ($x = 100\text{m}$ to $x = 75\text{m}$) raising with a height of 0.3m ($+1.2\text{m}$ to $+1.5\text{m}$ NAP). In the following 20 days the sandbar widens and increases in height relatively slow (arrow 3). Just before the storm hits a short and rapid onshore movement and elevation of the crest is visible (arrow 4). Finally, the intertidal sandbars are vanished by the storm creating a smooth parabolic beach shape (arrow 5).

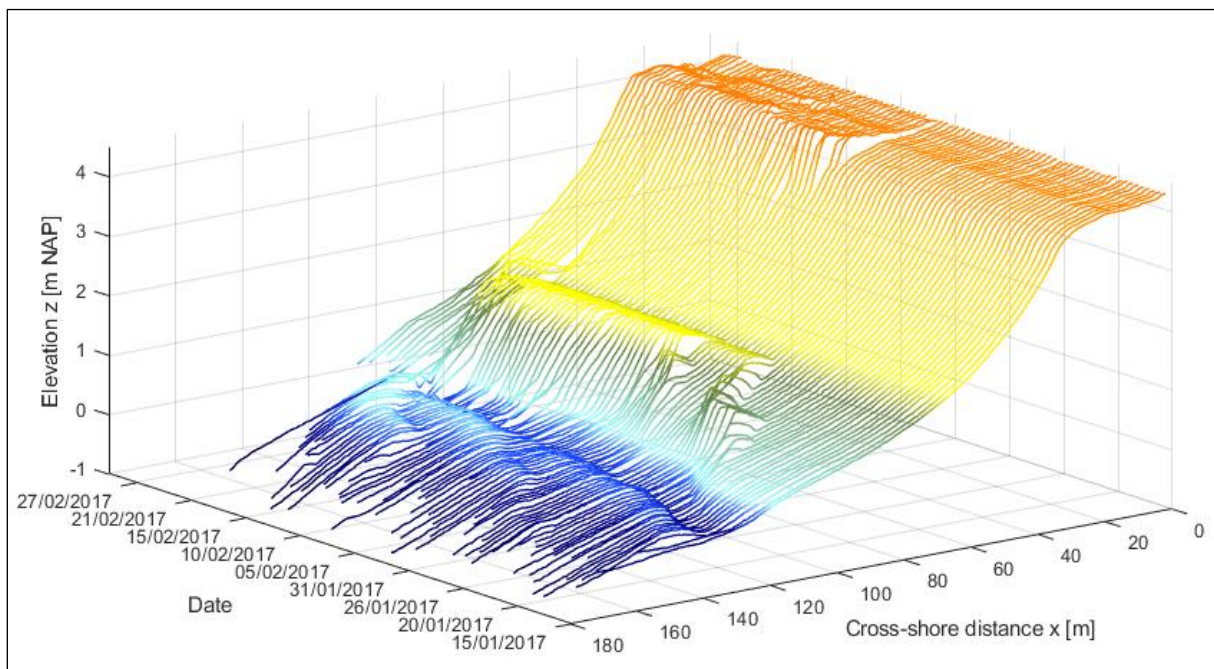


Figure 4-14: 3D view of 82 low water bed levels at cross section 1, from January 15 to February 28, 2017.

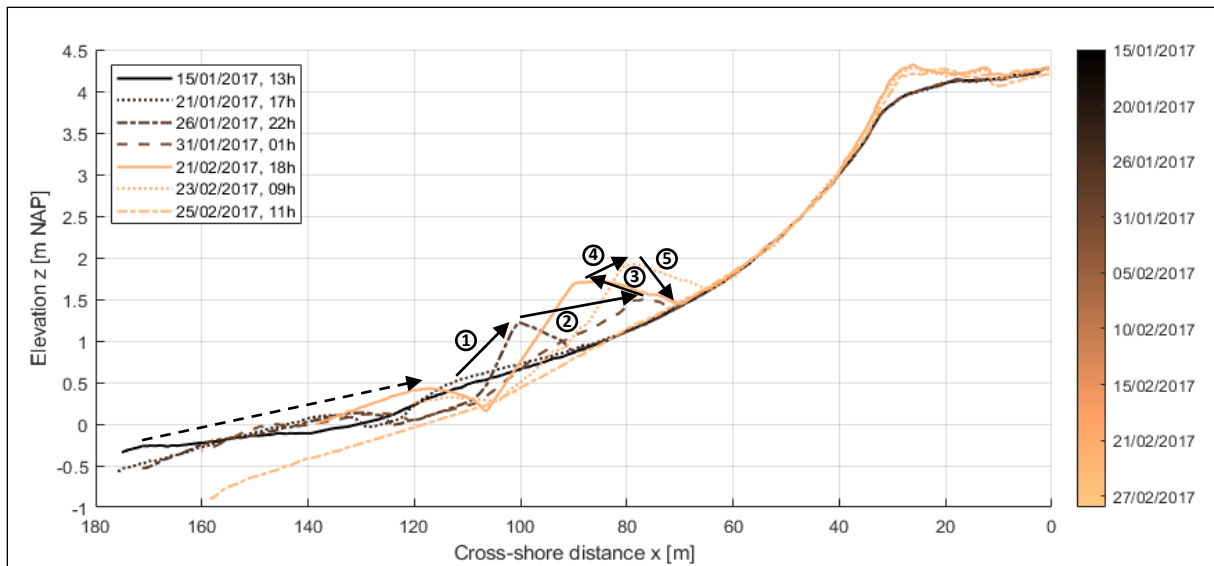


Figure 4-15: Bed levels at cross section 1 of 7 low water periods, from January 15 to February 25, 2017. The dashed arrow indicates the movement of the lower intertidal bar and the arrows with numbers 1 to 5 indicate decisive movements of the upper intertidal bar.

At the berm, near the foot of the dune, manmade profile changes are induced. Approximately halfway the measuring period (around February 26) a distinctive change is visible in the upper part of the profile ($x < 40\text{m}$). The elevation significantly increases in one to two days. Here, bulldozers relocated sand from the dune foot (just outside the domain, $x < 0\text{m}$) into offshore directions at the beach, as described in subsection 4.3.6.

Sediment transport patterns

The bed level development in cross-shore direction can be translated into sedimentation and erosion patterns, indicating sediment transport. In Figure 4-16 a sedimentation and erosion stack plot are shown between each subsequent low water period. Except for the four missing low water periods indicated by the vertical dotted lines (as described in subsection 4.2.1). Despite of some measurement errors, sedimentation and erosion patterns are clearly visible. The lower intertidal bar is fed by small amplitude bars, indicated by the dashed arrows. The distinctive upper intertidal bar changes (shown in Figure 4-15) can also be observed in the stack plot, indicated by the arrows with numbers. Especially the strong onshore movement from the 26th until the 31st of January (arrow 2). Here, sedimentation and erosion occur respectively on the onshore and offshore side of the intertidal bar. This sandbar migration is analyzed in more detail in the next section.

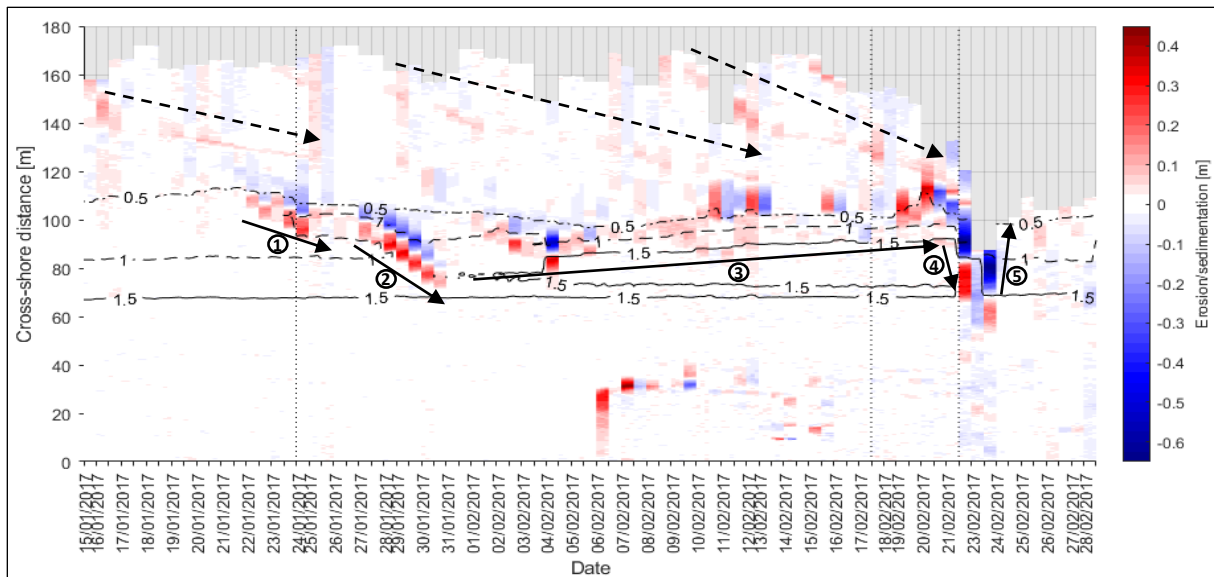


Figure 4-16: Sedimentation and erosion stack plot at cross section 1 in the period from January 15 to February 28, 2017. The black contour lines indicate isobaths at +0.5 m, +1 m and +1.5 m NAP. The vertical dotted lines indicate the date of the missing low water periods from which the 3th line represents two missing low water periods. The dashed arrows indicated the movement of small amplitude sandbars. The solid arrows with numbers 1 to 5 indicate decisive movements of the upper intertidal bar as shown in Figure 4-15.

4.4.2. Period B (onshore intertidal bar migration)

Bed level development

In the period from the 26th to the 31st of January a fast onshore upper intertidal bar movement is visible without inundation of the bar crest. The onshore bar movement is clearly visible in Figure 4-17. The dashed dotted lines indicate the highest water level (including surge) after each low water period, observed at Scheveningen. It can be observed that this water level does not rise above the bar crest at any time. However, the sediment transport of the sandbar is significant. Therefore, it can be concluded that swash zone processes are dominant (as described chapter 2) and consequently cause the onshore migration of the intertidal bar.

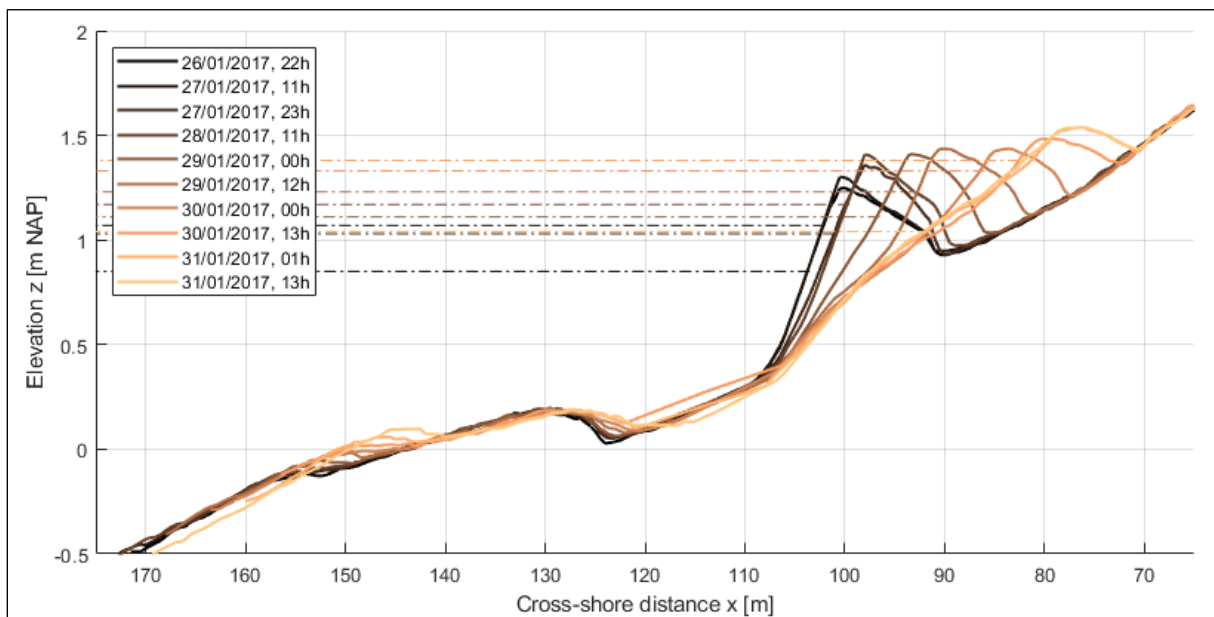


Figure 4-17: Low water bed levels at cross section 1, from January 26 to 31, 2017. The dashed dotted lines indicate the still high water level (including surge) after each subsequent low water period.

The lower intertidal bar shows a slow onshore movement. The lower intertidal bar with its crest initially at a cross-shore distance of 130m slowly migrates onshore. Lower in the profile a small amplitude bar (around a cross-shore distance of 150m) is catching up with the other intertidal bar. The small amplitude bar feeds the lower intertidal bar and ultimately might feed the upper intertidal bar.

Sediment transport patterns

The transport of sediment during the high water levels occurs mainly within periods of one to two hours. In Figure 4-18 the hourly sedimentation and erosion patterns are visualized in a stack plot. The sedimentation and erosion for each scan is calculated with respect to its previous low water scan (vertical black lines). In general, no data is available of the sandbar during a period of one to two hours, indicated by the gray area. In these intervals all the sediment is transported, migrating the sandbar onshore. In the periods just after the second, third and fourth high water levels a decreasing sedimentation pattern can be observed (1). These patterns indicate the retreat of water from the runnel onshore of the sandbar.

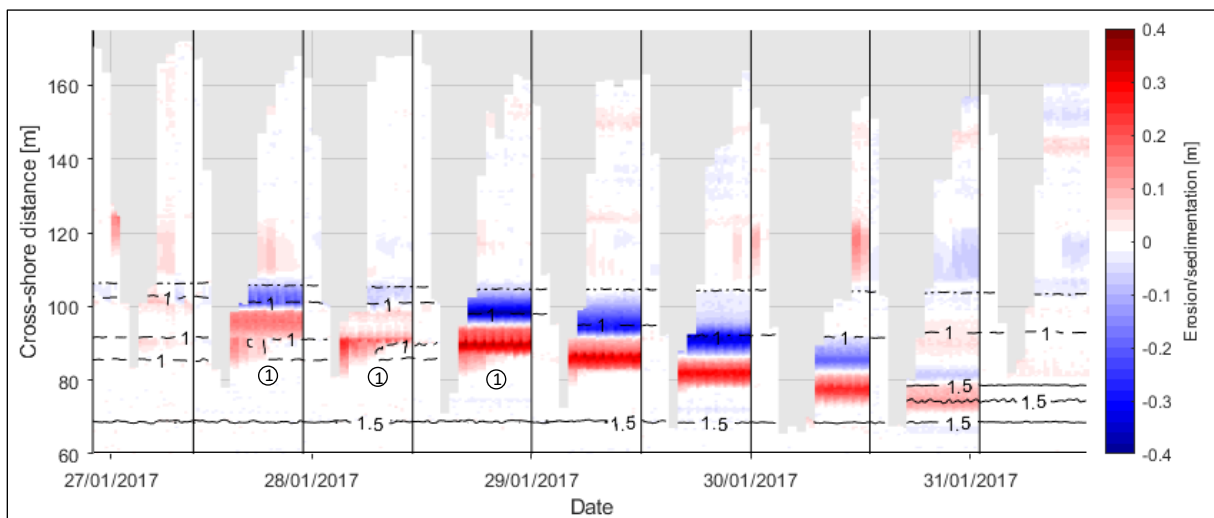


Figure 4-18: Hourly sedimentation and erosion stack plot at cross section 1 in the period from January 26 to 31, 2017. The sedimentation and erosion are calculated with respect to the previous low water scan, indicated by the vertical black lines. The black contour lines indicate isobaths at +0.5 m, +1 m and +1.5 m NAP. The circled ones indicate the retreat of water.

Sediment transport volumes

The bed level height difference between subsequent low water scans quantifies the transported sediment volumes during a tidal cycle. In period B (from January 26 to 31) transported sediment volumes (S_x) of up to $0.4 \text{ m}^3/\text{m}$ per meter width in a tidal cycle can be observed from Figure 4-19. Integrating the sediment transport volumes starting at the onshore boundary, result in the cumulative sediment transport volume in cross-shore direction. During most of the nine tidal cycles a clear net onshore movement is visible at the intertidal sandbar ($Q_x > 0$). The fourth and fifth tidal cycle contain the largest onshore flux (Q_x) of up to nearly 2 m^3 per meter width in a tidal cycle.

Most of the sediment budgets are not closed at the offshore boundary ($Q_x \neq 0$). This can partly be explained by measurement and interpolation errors. When low water scans eight and nine were taken, the runnel between cross-shore distances $x = 105\text{m}$ and $x = 120\text{m}$ (between the lower and upper intertidal bar) has not run dry completely. Therefore, no data is available in this area resulting in an interpolation error as discussed in 0. This error can be observed in Figure 4-19 by relatively large sedimented volumes (tidal cycle 7) followed by eroded volumes (tidal cycle 8 and 9). Apart from these errors, subtidal sediment transport and longshore sediment transport might also contribute to the export or import of sediment.

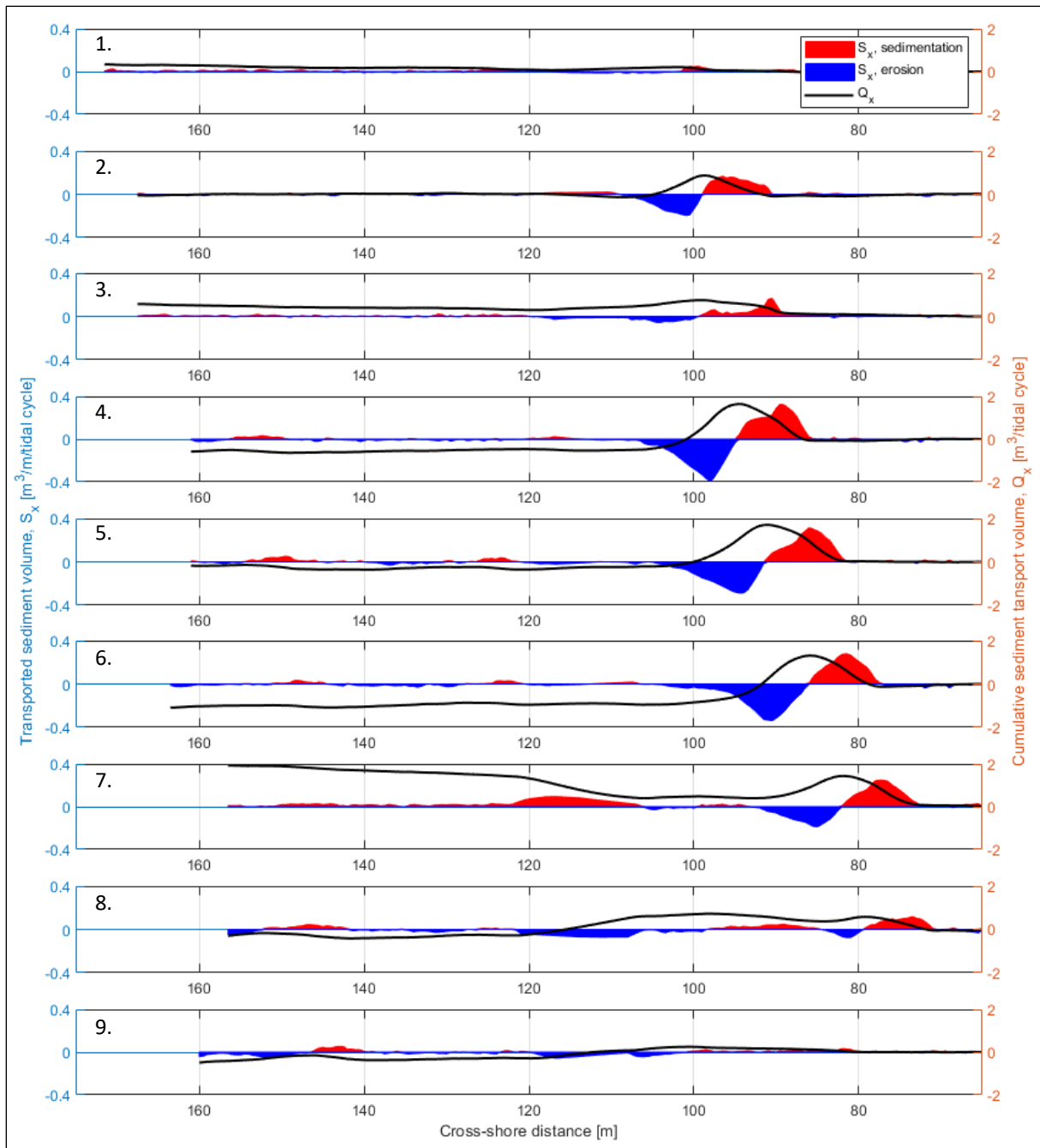


Figure 4-19: Transported sediment volumes S_x and cumulative sediment transport volumes Q_x for nine tidal cycles in the period from the January 26 to 31.

4.5. Conclusion

Based on this chapter an answer is given to sub-question 2, described below.

SQ 2: What is the intertidal bar behavior during mild and energetic wave conditions found in the TLS measurements at Kijkduin and which sediment transport processes are responsible?

In a period of approximately 6 weeks (period A), two distinctive intertidal bars develop, grow and migrate onshore during mild wave conditions and eventually erode again during a storm. In this period, the lower and upper intertidal bars grow vertically with a height of 0.7m and 1.4m and move onshore over a cross-shore distance of 50m and 35m, respectively. While the lower intertidal bar develops more gradually, fed by smaller bars, the upper intertidal bar develops in five distinctive steps:

1. Formation (fast vertical growth)
2. Fast onshore migration
3. Gradual horizontal and vertical growth
4. Fast and short vertical growth and onshore migration
5. Fast destruction

In a period of less than 5 days (period B), the fast onshore migration of the upper intertidal bar (second distinctive step) can largely be explained by a shift of sediment from the offshore side to the onshore side of the bar. In nine tidal cycles the upper bar grows vertically with a height of 0.3m and moves onshore over a cross-shore distance of 25m. Sediment is transported onshore up to nearly 2 m³ per meter width in one tidal cycle.

Based on the results it can be concluded that the swash zone processes are the dominant forcing mechanism for the onshore migration of the upper intertidal bar in period B. The intertidal bar is not submerged in the period of nine tidal cycles. Therefore, the onshore migration occurred due to swash zone processes. The wave-breaking induced turbulent uprush transports sediment over the bar crest where the gravity induced backwash takes over. It is not possible to state the dominant sediment transport processes for the lower intertidal bar.

5. XBeach modelling

This chapter describes the reproduction of the TLS measurement results (from the previous chapter) for a period of less than 5 days (period B) in two XBeach models, the surf beat model and the hydrostatic swash model. The chapter is divided in the model selection and description (section 5.1), the model setup for the two selected models (section 5.2) and the simulated results (section 5.3). Finally, in section 5.4, sub-question 4 is answered.

5.1. Model selection and description

XBeach is a numerical model that simulates hydrodynamic and morphodynamic processes following the model setup given in Figure 5-1. Starting with a specified initial bathymetry, coupled 2D horizontal equations for wave propagation, flow, sediment transport and bottom change are solved for varying boundary conditions (Roelvink et al., 2009). In this case only the 1D cross-shore development is modelled and therefore treated here. After each timestep the bathymetry is updated and the calculations are repeated until the model end time is reached. The following sections describe the important model formulations in XBeach related to the morphodynamics. These model formulations depend on the hydrodynamic model chosen and is therefore treated first. For the hydrodynamic model, apart from the hydrodynamic model, is referred to [Roelvink et al. (2009); Roelvink et al. (2018b); Reniers et al. (2013)].

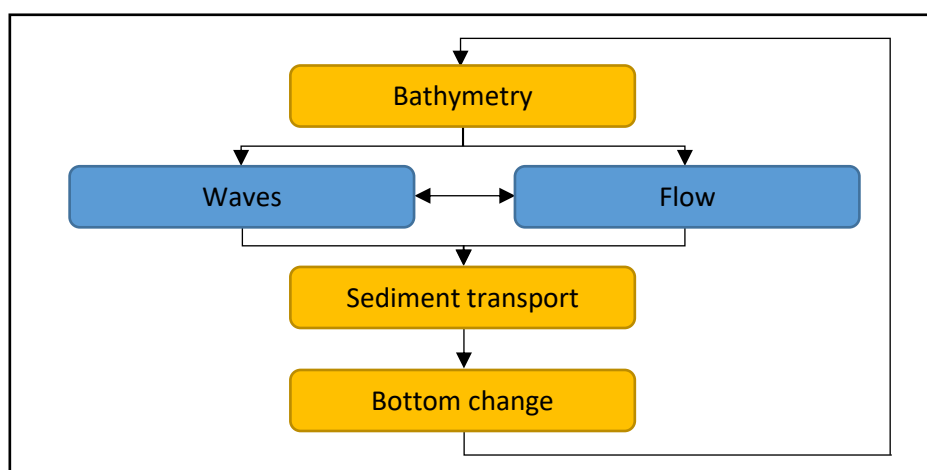


Figure 5-1: XBeach model setup.

5.1.1. Hydrodynamic model selection

Four hydrodynamic models can be used to calculate the fluid motions and concurrent sediment transport. In the current XBeach model there are three hydrodynamic model options: **Stationary, surf beat and non-hydrostatic** (Roelvink et al., 2018b). Additionally an earlier version of XBeach is extended to the **hydrostatic swash model** (Reniers et al., 2013). In the stationary model wave-averaged equations are solved. The cross-shore sediment transport in this model is induced by the mean return flow (due to mass flux and roller) and wave asymmetry and skewness effects. In the surf beat model the variations of the short waves on the scale of wave groups (short wave envelope) are resolved. These variations drive the (longer period) infra-gravity waves which are therefore included in this model. Finally, in the non-hydrostatic and hydrostatic swash models, the propagation and decay of short waves are modelled by the non-linear shallow water equations (NLSWE) with and without a non-hydrostatic pressure correction term respectively.

Both the surf beat and hydrostatic swash model are used for the analysis of Kijkduin. In section 2.5 it was concluded that the forcing oscillatory wave motion in the swash zone might be the long (infra-gravity) waves and/or the short waves. As the stationary model neglects both the short and the long waves this model is not applicable for this case. The non-hydrostatic model is not applicable either as the simulation of morphology on sandy beaches is still in development and has not (yet) been validated extensively (Roelvink et al., 2018a). The surf beat and hydrostatic swash model do include the most important cross-shore sediment transport processes (as concluded in section 2.5). The main differences between these two models are described below:

- The surf beat model simulates morphological changes on the wave group timescale, whereas the hydrostatic swash model on the individual short wave timescale. In the surf beat model the NLSWE are fed by the wave and roller forces, which are calculated by the wave action- and roller energy balance. Subsequently, the depth-averaged velocities and the water surface elevation can be calculated on the wave group timescale. In the hydrostatic swash model, the depth-averaged velocities and surface elevation of all the wave motions (including the short waves) are directly calculated by applying the boundary conditions onto the NLSWE.
- The surf beat model can be used in relatively deep water, whereas the hydrostatic swash model cannot. As in the surf beat model only the longer period waves are simulated in the shallow water equations, the shallow water criterion ($kh \ll 1$ or $h/L < 0.05$) is met for deeper water. Offshore wave and flow boundary conditions can therefore be applied directly to the model, keeping in mind the shallow water criterion.
- The hydrostatic swash model is computationally more expensive than the surf beat model. The hydrostatic swash model requires a higher spatial resolution to resolve the short wave motions, increasing the computational time. To provide numerical stability the numerical timestep needs to be small, further increasing the computational time. Although the wave action balance is not required, saving computational time, the hydrostatic swash model is still much more computational expensive.

It can be concluded that the preference of the model depends on the importance of the individual short waves for the sediment transport. When the long waves are dominant the surf beat model is preferred as it is computationally less expensive and offshore boundary conditions can be applied more easily. However, when the sediment transport on the short wave timescale is significant, the hydrostatic swash model might be preferred.

The sediment transport is described by different formulations for the surf beat and hydrostatic swash model. These formulations, followed by the implementation of the dominant cross-shore sediment transport processes (see section 2.5), are described separately for both models in the following two subsections.

5.1.2. Sediment transport: surf beat model

Transport formulations

The sediment transport in the surf beat model for both the *bed load* and the *suspended load* are modelled using a depth-averaged advection diffusion equation by Galappatti and Vreugdenhil (1985). The 1D cross-shore (x-direction) advection diffusion equation is given by:

$$\frac{\partial hC}{\partial t} + \frac{\partial hCu^E}{\partial x} + \frac{\partial}{\partial x} \left[D_h h \frac{\partial C}{\partial x} \right] = \frac{hC_{eq} - hC}{T_s} \quad (5.1)$$

where C represents the depth-averaged sediment concentration varying on the wave group time scale, u^E is the Eulerian velocity (the short-wave-averaged velocity observed at a fixed point) and D_h is the sediment diffusion coefficient. Consequently, the 1D cross-shore sediment transport is calculated according to:

$$S_x = S_b + S_s = hCu^E + D_h h \frac{\partial C}{\partial x}. \quad (5.2)$$

The right hand side of equation (5.1) represents the source and sink term, where the difference between the actual concentration, C , and the equilibrium concentration, C_{eq} , determines the entrainment or deposition of sediment. The response of the entrainment of sediment is determined by the adaptation time, T_s . Based on the local water depth, h , and the sediment fall velocity, w_s , the adaptation time is given by (Reniers et al., 2004):

$$T_s = \max \left(f_{T_s} \frac{h}{w_s}, T_{s,min} \right) \quad (5.3)$$

where f_{T_s} is a calibration factor (default value 0.1) and $T_{s,min}$ is the minimum adaptation time (default at 0.5 second). In shallow water the adaptation time becomes small ($T_s \approx T_{s,min}$), corresponding to nearly instantaneous sediment response for changing hydrodynamics.

The equilibrium sediment concentration can be calculated with several transport formulae. The default sediment transport formulation used in the present version of XBeach (Roelvink et al., 2018b) are the Van Thiel-Van Rijn equations. In these equations the equilibrium sediment concentrations for bed load $C_{eq,b}$ and suspended load transport $C_{eq,s}$ are calculated separately according to (van Rijn, 2007; Van Thiel de Vries, 2009):

$$C_{eq,b} = \frac{A_{sb}}{h} \left(\sqrt{|u^E|^2 + 0.64u_{rms,2}^2} - U_{cr} \right)^{1.5} \quad (5.4)$$

$$C_{eq,s} = \frac{A_{ss}}{h} \left(\sqrt{|u^E|^2 + 0.64u_{rms,2}^2} - U_{cr} \right)^{2.4} \quad (5.5)$$

where sediment is set in motion when a combination of flow stirring, by the Eulerian velocity u^E , and wave stirring, by the near-bed short wave orbital velocity $u_{rms,2}$, exceeds a threshold of motion, U_{cr} . The sediment grain size, relative density and the local water depth are included in the bed load coefficient, A_{sb} , and the suspended load coefficient, A_{ss} .

Cross-shore sediment transport processes

The effect of wave nonlinearities, *wave skewness* and *asymmetry*, on sediment transport is not simulated directly as the individual (short) waves are not modelled. To include their influence however, they are implemented by a mean flow velocity component due to nonlinear waves, u_a , in the advection diffusion equation (5.1). In the advection term the Eulerian velocity (u_E) is replaced by:

$$u_E - u_a \sin \theta_m \quad (5.6)$$

where θ_m is the mean wave direction. The additional advective velocity is defined as (Van Thiel de Vries, 2009):

$$u_a = (f_{Sk} S_k - f_{As} A_s) u_{rms} \quad (5.7)$$

where f_{Sk} and f_{As} are two calibration factors and u_{rms} is the orbital velocity due to short waves. The wave skewness, S_k , and the wave asymmetry, A_s , are calculated based on the water depth, dimensionless wave height and dimensionless wave period (Van Thiel de Vries, 2009).

The *undertow* and the *infra-gravity waves* are included in the advective velocity and flow stirring. The undertow and the infra-gravity waves are included in the Eulerian velocity, u_E . This flow velocity is implemented in the advection diffusion equation (5.1) as an advective velocity. Moreover, the Eulerian velocity is implemented in the equilibrium sediment concentration equations for bed load (5.4) and suspended load (5.5) in the form of flow stirring.

The *turbulence* is accounted for by the wave stirring term $u_{rms,2}$ in the equilibrium sediment concentration. $u_{rms,2}$ is a combination of the orbital velocity due to short waves, u_{rms} , and the breaking induced turbulence near the bed due to short waves, k_b , according to the empirical formulation (Van Thiel de Vries, 2009):

$$u_{rms,2} = \sqrt{u_{rms}^2 + 1.45 k_b} \quad (5.8)$$

Finally, the effect of *gravity* on the sediment transport is implemented in a bed-slope correction factor. This correction factor is based on the bed slope, where sediment transport is enhanced or inhibited for an up- or down-sloping bed respectively. The magnitude of the cross-shore sediment transport including the bed-slope correction factor is given by:

$$S_{x,slope} = S_x - \alpha h C u^L \frac{\partial z_b}{\partial x} \quad (5.9)$$

where α is a calibration factor and u^L is the Lagrangian velocity according to the GLM approach (Roelvink et al., 2018b).

5.1.3. Sediment transport: hydrostatic swash model

Transport formulations

The sediment transport for the bed load and suspended load is modelled separately in the hydrostatic swash model. The bed load transport is calculated based on the model of Meyer-Peter and Müller (1948):

$$S_b = 12 \beta_s \left[\max[|\theta'(t)| - \theta_{cr}, 0] \right] \sqrt{\theta'(t)} \frac{u(t)}{|u(t)|} \sqrt{\Delta g D^3} \quad (5.10)$$

where sediment is set in motion when the non-dimensional shear stress, $\theta'(t)$, exceeds a threshold value, θ_{cr} . Furthermore, the sediment transport is depended on the bed-slope correction factor, β_s , the

instantaneous cross-shore velocity, $u(t)$, the relative weight of the sediment, Δ (≈ 1.6 for sand), and the grain size diameter, D . The non-dimensional shear stress is given by:

$$\theta'(t) = \frac{0.5f_{2.5}(u^2(t) + k_b)}{g\Delta D} \quad (5.11)$$

where $f_{2.5}$ is the wave friction factor and k_b is the near-bed wave-breaking induced turbulence (Reniers et al., 2013).

The suspended load transport is calculated (in a similar way as the surf beat model) with the depth-averaged advection diffusion equation (5.1). The cross-shore suspended sediment transport is thus given by (similar to equation (5.2)):

$$S_s = hCu + Kh \frac{\partial C}{\partial x} \quad (5.12)$$

where in this case the sediment diffusion coefficient D_h , is replaced by the horizontal diffusivity coefficient K . This coefficient is set equal to the turbulent eddy viscosity, u_h , given by:

$$u_h = \max(0.1, 0.3h\sqrt{k}) \quad (5.13)$$

where k is the turbulent kinetic energy calculated according to (Reniers et al., 2013). The depth-averaged equilibrium concentration associated with wave breaking only is calculated according to (Roelvink and Stive, 1989) by rewriting the suspended load transport formulation:

$$C_{eq} = \frac{\epsilon_s}{g\Delta w_s h} \beta_d k_b^{\frac{3}{2}} \quad (5.14)$$

where ϵ_s is the suspended load efficiency (Bailard, 1981) and β_d is a turbulent stirring calibration factor.

Cross-shore sediment transport processes

The effects of *wave skewness and asymmetry*, the *undertow* and *infra-gravity waves* are all implemented in the instantaneous cross-shore velocity, $u(t)$. In the hydrostatic swash model, the short wave motion is simulated where waves are breaking individually and the wave shape changes, such that wave skewness and asymmetry can be computed. Infra-gravity waves can be included at the offshore boundary. They are no longer included by the radiation stress source term in the NLSWE (as the case in the surf beat model) and should therefore be applied directly at the offshore boundary. Finally, the undertow balances the onshore mass transport due to wave breaking and rollers.

The instantaneous cross-shore velocity, and therefore the above mentioned processes, is included in the advective velocity (both bed load and suspended load) and sediment stirring (only bed load). In the bed load transport, equation (5.10), the cross-shore velocity is implemented in the non-dimensional shear stress and is therefore partly determining the stirring and advection of the sediment. Moreover, $u(t)$ determines the direction of the sediment transport. In the suspended load transport, equation (5.12) the cross-shore velocity determines the advection of the sediment.

The *turbulence* is implemented in both the bed load and the suspended load sediment transport by the turbulent kinetic energy, k . In the suspended load transport the turbulent kinetic energy is included directly as part of the turbulent eddy viscosity. Additionally, the turbulence is included by the near-bed wave-breaking induced turbulence, k_b . This term is a function of the turbulent kinetic energy accounting for the vertical decay with the distance from the surface according to Roelvink and Stive

(1989). The near-bed wave-breaking induced turbulence is included in the non-dimensional shear stress as expressed in equation (5.11), representing the initiation of motion for the bed load transport. k_b is also included in the equilibrium sediment concentration for suspended load transport in equation (5.14). Here, the suspended load efficiency, ϵ_s , and the calibration factor, β_d , can be adjusted to increase or decrease the suspended sediment load in the water column.

The effect of *gravity* is implemented in the bed load sediment transport by the bed-slope correction factor β_s , in equation (5.10). the bed-slope correction factor is given by:

$$\beta_s = \cos\beta_b \left(1 - \frac{u(t) \tan\beta_b}{|u(t)| \tan\phi} \right) \quad (5.15)$$

where β_b is the local bed slope and ϕ is a critical bed slope.

5.1.4. Bottom change

The next step in both the surf beat and the hydrostatic swash model is the simulation of the bottom change based on the conservation of mass. The gradients of the calculated cross-shore sediment transport, $S_{x,slope}$ (surf beat model) or S_x (hydrostatic swash model), result in the bottom change (erosion or accretion). Similar to equation (2.2), the bed level changes according to:

$$\frac{\partial z_b}{\partial t} + \frac{f_{mor}}{(1-p)} \frac{\partial S_x}{\partial x} = 0 \quad (5.16)$$

where z_b is the bed level, f_{mor} is a morphological acceleration factor and p is the porosity. With these bed level changes the bathymetry gets updated and the hydrodynamic and morphodynamic calculations are repeated.

5.2. Model setup

The model setup, for the above selected and described surf beat model and hydrostatic swash model, is described in this section. Both the surf beat model and the hydrostatic swash model are used to simulate the morphological response at cross section 1 and for period B (January 26 to 31, 2017). This cross section and period were described and selected in section 4.2.

5.2.1. General setup

To simulate the cross-shore morphology in XBeach the **simulation time**, the **bathymetry and grid** and the **boundary conditions** need to be stated first. In period B an onshore growing and migrating intertidal sandbar is observed, described in subsection 4.4.2. This period of nine tidal cycles is simulated in the XBeach surf beat and hydrostatic swash models and therefore represents the simulation time. The survey in January 2017 is used to setup the bathymetry for both the surf beat model and the hydrostatic swash model. In Figure 5-2 it can be observed that the survey fits well with the TLS measurements for cross section 1. When zooming in at the intertidal bar in Figure 5-2b, it appears that the TLS measurements of the 26th at 22 hours and the 27th at 11 hours fit best with the survey. In this case, the first of these two measurements is used as the starting point for the simulations in XBeach. The bathymetry and grid, the boundary conditions and some general settings are described separately for the surf beat and hydrostatic swash model in their model setup (subsections 5.2.2 and 5.2.3 respectively).

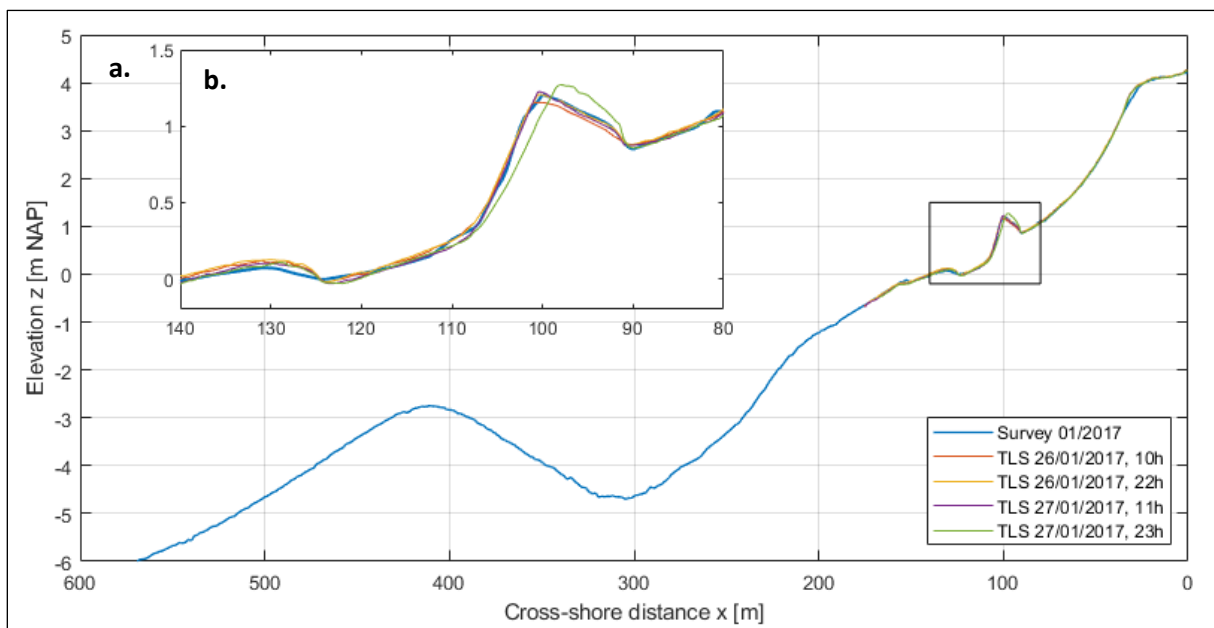


Figure 5-2: Bed levels at cross section 1. Observed during the bathymetry survey in January 2017 and TLS measurements on the 26th and 27th of January 2017. Figure b clarifies the differences around the intertidal bar indicated by the box.

5.2.2. Surf beat model setup

Bathymetry and grid

The bathymetry, based on the survey of January 2017, is extended in cross-shore direction down to a depth of approximately 11m with respect to NAP. In Figure 5-3 the bed levels of three surveys (September 2016, January and July 2017) are shown for cross section 1. There are significant changes visible between the subsequent surveys. Both in the intertidal area as well as in the subtidal area. However, around the cross-shore distance of 500 m the bed levels changes seem to diminish in offshore direction. Therefore, the bathymetry obtained from January (reaching up to a depth of 6 m) can be extended to a depth of 11 m, using the survey of July 2017.

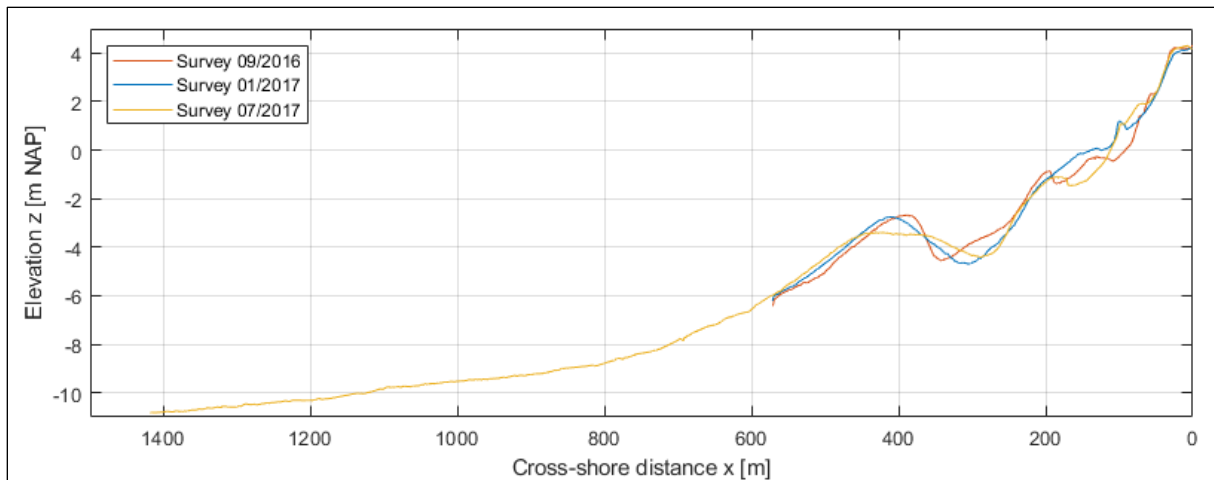


Figure 5-3: Bed levels at cross section 1. Observed during the surveys in September 2016 and January and July 2017.

The bathymetry is extended further, to a depth of 30m, such that the wave conditions can directly be applied to the offshore boundary of the model. Moreover, sufficiently deep water is required to ensure realistic long wave boundary conditions with no wave breaking ($c_g/c < 0.8$). The wave conditions are known at the Europlatform which is located 40 km offshore of the coast of Goeree at a water depth of 30m (see Figure 3-1 in chapter 3). To extend the bathymetry to the required water depth a slope of 1/25 is applied. In contrast with extrapolating the flat slope of the survey at July 2017, this slope diminishes the cross-shore length of the bathymetry. Ultimately reducing the computational effort of the model. The total bathymetry used for the surf beat model, consisting of the surveys at January and July 2017 and the extension to the Europlatform, is shown in Figure 5-4.

A variable cross-shore grid size is used to optimize the model. Using the function `xb_grid_xgrid` from the Open Earth Tools (OET), the grid size is determined based on the water depth and the long (intra-gravity) wave resolution (Van Koningsveld et al., 2010; Hoonhout, 2015). The grid resolution should be sufficiently high to describe intra-gravity waves (10 – 20 points) and morphological features (5 – 10 points) (Roelvink et al., 2018b). On the contrary, the grid resolution should be low to diminish the computational effort. In this case the grid size of the intertidal area is 0.5m, providing good detail on small scale changes. With increasing water depth, the grid size increases up to 13m at the offshore boundary.

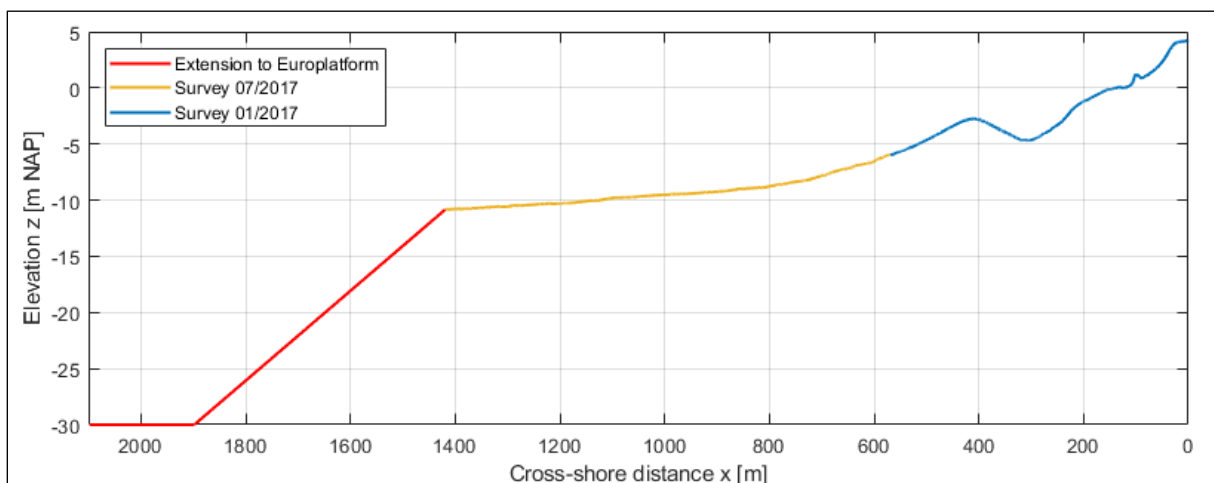


Figure 5-4: The total bathymetry used as a reference situation for the surf beat model. The original bathymetry (yellow and blue) obtained from two surveys is extended up to a depth of 30 m (red).

Boundary conditions

Waves

The wave boundary condition is defined by time varying JONSWAP spectra obtained from the Europlatform. As the XBeach grid extends down to the Europlatform water depth, the wave conditions from this platform can directly be applied at the offshore boundary. The wave spectra are described by a set of parameters, listed in Table 5-1.

XBeach parameter	Description	Unit
H_{m0}	Significant wave height of the wave spectrum	[m]
T_p	Peak wave period of the wave spectrum	[s]
θ_m	Mean incident wave angle	[degrees]
s	Directional spreading coefficient	[-]
γ	Peak enhancement factor	[-]
duration	Duration of the wave spectrum	[s]

Table 5-1: Wave boundary condition parameters as input for XBeach.

The significant wave height, H_{m0} , peak wave period, T_p , and mean incident wave angle, θ_m , are shown in Figure 5-5 (a, b and c). In the period of less than 5 days the significant wave height varies between 0.5m and 1.6m with an average peak period of 5 seconds. The mean wave direction is primarily directed offshore outside the model domain (indicated by the horizontal dashed lines in Figure 5-5c), especially the first two days. Therefore, large amounts of energy are lost at the offshore boundary, reducing the wave energy approaching the coast. The observed mean incident wave angle is accompanied by the directional spreading coefficient, s , indicating the wave directional spreading. The peak enhancement factor is set to $\gamma = 3.3$ and corresponds to a JONSWAP spectrum shape for deep water conditions. Finally, the duration of the wave spectra is a compromise between stationary time series (requiring a short enough duration) and reliable averages (requiring a long enough duration).

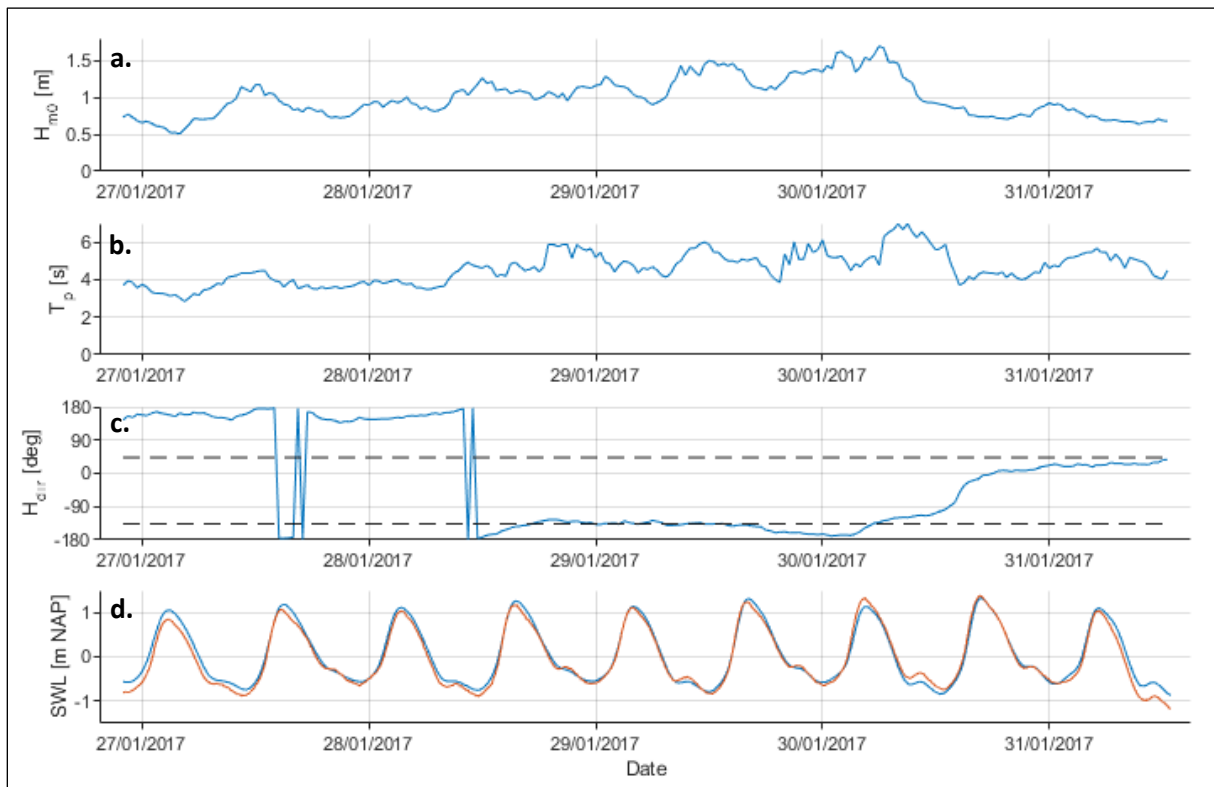


Figure 5-5: Significant wave heights (a), peak periods (b), mean wave directions (c) and still water levels (d) in the period from January 26 to 31, 2017. The horizontal dashed lines in figure c indicate the minimum and maximum angles of the domain. In figure d, the blue line is the astronomical tidal level only and the red line includes the surge level.

Tide and surge

The astronomical tide and surge boundary condition is defined by time varying data obtained from Scheveningen. The tide and surge levels (varying every 10 minutes), shown in Figure 5-5 (d), are applied on the offshore boundary of the domain. A uniform water level change can be assumed as the tide is a slowly varying long wave, preventing surface gradient induced flow.

Default and WTI settings

A large number of parameters (around 300) can be adjusted to control the performance of the model. Default settings have been defined by XBeach developers for all these parameters. These default settings have been re-determined in the WTI2017 project ('Wettelijk Toets Instrumentarium') (Van Geer et al., 2015) in order to apply XBeach on the Dutch coast more accurately. The derivation of the WTI settings is based on the comparison of numerical results to measured result from 30 test cases. Nine parameters were found to be most sensitive to the influence on the numerical results, listed in Table 5-2 (Van Geer et al., 2015).

XBeach Parameter	Default setting	WTI setting	Description
wetslp	0.300	0.260	Critical avalanching slope under water
dryslp	1.000	1.000	Critical avalanching slope above water
alpha	1.000	1.262	Wave dissipation coefficient in Roelvink formulation
facSk	0.100	0.375	Calibration factor time averaged flows due to wave skewness
facAs	0.100	0.123	Calibration factor time averaged flows due to wave asymmetry
gamma	0.550	0.541	Breaker parameter in Baldock or Roelvink formulation
fw	0.000	0.000	Short-wave friction coefficient
cf	0.003	0.001	Dimensionless friction coefficient flow
gammax	2.000	2.364	Maximum ratio wave height to water depth
beta	0.100	0.138	Breaker slope coefficient in roller model

Table 5-2: Default and WTI settings for XBeach (Van Geer et al., 2015).

5.2.3. Hydrostatic swash model setup

Bathymetry and grid

The survey in January 2017 is used to setup the bathymetry for the hydrostatic swash model, at the offshore boundary to a depth of -0.5m NAP (cross-shore distance $x = 170\text{m}$). The water depth in the hydrostatic swash model should be very small to agree to the shallow water criteria ($kh \ll 1$ or $h/L < 0.05$), where vertical accelerations in the water can be ignored and a hydrostatic pressure is present. In this case, with an average peak wave period of 5 seconds, the water depth should be smaller than 0.6m to agree to that criteria. As the intertidal zone ranges from approximately -1.2m to +1.4m NAP during period B (as shown in Figure 5-5) the shallow water criteria cannot be met if the entire intertidal zone is simulated. The bathymetry is therefore shortened up to a bed level of -0.5m NAP, focusing on the upper intertidal bar development.

The entire bathymetry has a cross-shore grid size of 0.5m. Both the hydrodynamics as well as the morphodynamics require a small grid size to simulate short waves and morphological features respectively. To correctly describe the (nonlinear) wave shape of the short waves it is preferred to have 30 points per wave or more. On the contrary, it is preferred to set the grid size such that the computational effort is reasonable. In this case a grid size of 0.5m is used for the entire cross-shore domain.

Boundary conditions

Waves

The wave boundary condition is defined by a shallow water wave spectrum similar to a TMA spectrum. In shallow water a JONSWAP wave spectrum changes to a TMA wave spectrum. In the TMA spectrum the peak reduces and the high frequency tail of the short waves transforms from a f^{-5} shape (for the JONSWAP spectrum) to a f^{-3} shape (Bouws et al., 1985) reducing the wave energy in the high frequency tail. In this case, a TMA spectrum is approximated by reducing the peak enhancement factor of a JONSWAP spectrum ($\gamma=3.3$) to 1.0, mimicking the peak reduction of a TMA spectrum. Moreover, the high frequency tail is cut off at 1.5 times the peak frequency to reduce the wave energy in the high frequency tail. An example is shown in Figure 5-6 where the solid line represent the approximation of the TMA spectrum and the dashed line the original JONSWAP spectrum.

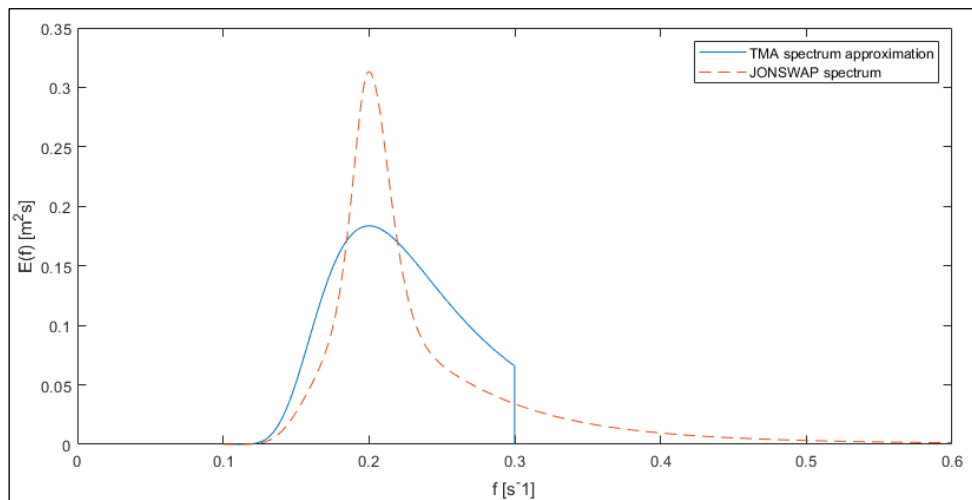


Figure 5-6: TMA wave spectrum approximation compared to a JONSWAP wave spectrum, for a significant wave height of 0.4m and peak wave period of 5s.

The significant short and long wave height for period B applied at the offshore boundary are 0.2m and 0.08m respectively. Waves observed at the Europlatform are transformed towards the coast using the surf beat model. The average peak short wave period at the Europlatform is about 5 seconds. In shallow water the peak wave frequency generally shifts to somewhat lower frequencies as the higher frequency waves start breaking first. Therefore, a peak wave period of 6 seconds is used for the simulation in the hydrostatic swash model. Additionally, a long wave peak period of 50s is assumed. With these wave conditions the wave spectra can be defined, as described above.

Tide and surge

Only the high water level periods are applied in the hydrostatic swash model as depicted in Figure 5-7. The offshore boundary is located at a depth of -0.5m NAP. The still water level is reaching below this depth during the low water level periods and therefore do not contribute to any morphological changes. Moreover, morphological changes of the upper intertidal bar only occur during the high water level periods, as shown and described in subsection 4.4.2. In this case the high water periods above a still water level of +0.0m NAP is applied in the hydrostatic swash model. In addition, it has the advantage that the simulation time decreases to less than 45 hours.

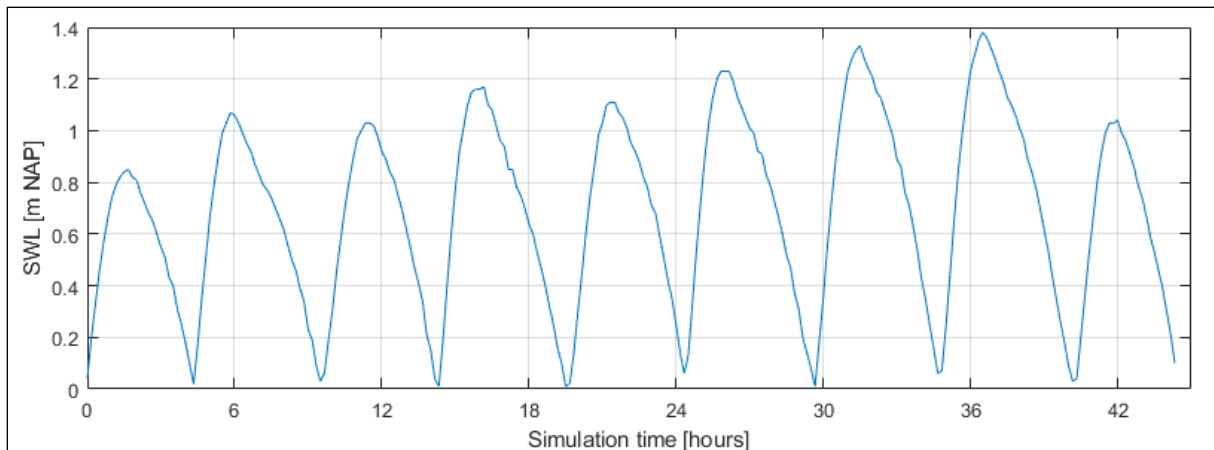


Figure 5-7: Still water levels (astronomical tide + surge) during high water periods ($> 0\text{m NAP}$) applied in the hydrostatic swash model.

Discharge outflow

A discharge outflow point is implemented in the model to simulate 3D effects through rip channels. In practice, waves that overtop the intertidal bar accumulate in the trough to form a channel of water. When the water level in the trough rises above the still water level or when the still water level drops, the accumulated water flows alongshore to rip channels where it flows back offshore to sea (3D effect). Once the still water level does not rise above the bar crest during high water, no return flow is expected to flow offshore over the bar crest. In the model, only cross-shore flows are simulated. Therefore, the water level in the trough might rise above the bar crest due to wave overtopping. Consequently, return flow and offshore sediment transport is induced erroneously. To overcome this error an outflow point with a discharge capacity of $0.01 \text{ m}^3/\text{s}$ is applied in the trough, simulating the 3D effect. The outflow point is located at a cross-shore distance ($x = 84\text{m}$) such that the intertidal bar has some space to migrate onshore will the outflow point remains in the trough. Preferably, several outflow points are implemented across the trough that migrate onshore with the intertidal bar and trough. This however, is not (yet) implemented in the model.

Settings

The settings of the hydrostatic swash model are based on settings in the surf beat model and the settings described in Reniers et al. (2013). Additionally, a suspended load efficiency, $\epsilon_s = 0.025$, is used according to Bailard (1981) and a turbulent stirring calibration factor, $\beta_d = 0.1$, is applied (Roelvink and Stive, 1989) both implemented in the equilibrium concentration for suspended load, equation (5.14). Furthermore, a critical wave slope, $m_{cr} = 0.1$, is applied. Wave fronts that exceed this slope are defined as breaking waves. The bed level is fixed over a distance of 20 grid points at the offshore boundary to prevent boundary effects. Moreover, the tidal cycles are not completed omitting the low water periods which affect the lower bed levels near the offshore boundary.

5.3. Results

Based on the model setup described in the previous section, the morphological response is simulated for cross section 1 in period B (January 26 to 31, 2017). The results are described in this section for the surf beat model (subsection 5.3.1) and the hydrostatic swash model (subsection 5.3.2), focusing on the upper intertidal bar changes. In subsection 5.3.3, these results are compared with the observed morphological changes in the TLS measurements (subsection 4.4.2).

5.3.1. Surf beat model

Bed level development and sediment transport volumes

In the period of less than 5 days (period B) the upper intertidal bar migrates onshore over a distance of 10m and the bar crest height slightly reduces, as shown in Figure 5-8. In the first three tidal cycles, morphological change is merely visible at the seaward side of the intertidal bar crest. The seaward slope of the bar flattens as sediment just below the crest is transported offshore to the bar toe. This can also clearly be observed from Figure 5-9 in the first three figures. Due to the offshore transport a beach scarp (near vertical beach slope) develops at the bar crest by avalanching, slightly reducing the bar crest height. From the fourth tidal cycle onwards, the intertidal bar starts to develop differently. In the fourth tidal cycle, the bar crest height reduces with about 0.1m and migrates onshore over a distance of 5m. Subsequently in the remaining five tidal cycles, the bar gradually grows and migrates onshore over a distance of 5m. Ultimately, the crest height nearly reaches its initial elevation. Furthermore, the seaward slope of the bar continuously flattens, from an initial slope of 0.15 to a slope of 0.05, while the landward slope steepens up to a slope of 0.25.

The slow growth and onshore migration in the second half of the simulation primarily occurs while the bar crest is submerged. The dashed dotted lines in Figure 5-8 indicate the highest still water level (including surge) after each low water period, observed at Scheveningen. This water level rises above the bar crest during several high water periods. In these periods it can therefore be concluded that surf zone processes are dominant at the sandbar. In tidal cycles five to eight (Figure 5-9), the sediment transport at the bar is mainly a shift of sediment in onshore direction ($Q_x > 0$, at $x \approx 90\text{m}$ to 100m). Moreover, onshore directed processes are dominant in the intertidal zone as the sediment budget is increasing ($Q_x > 0$ at the offshore edge).

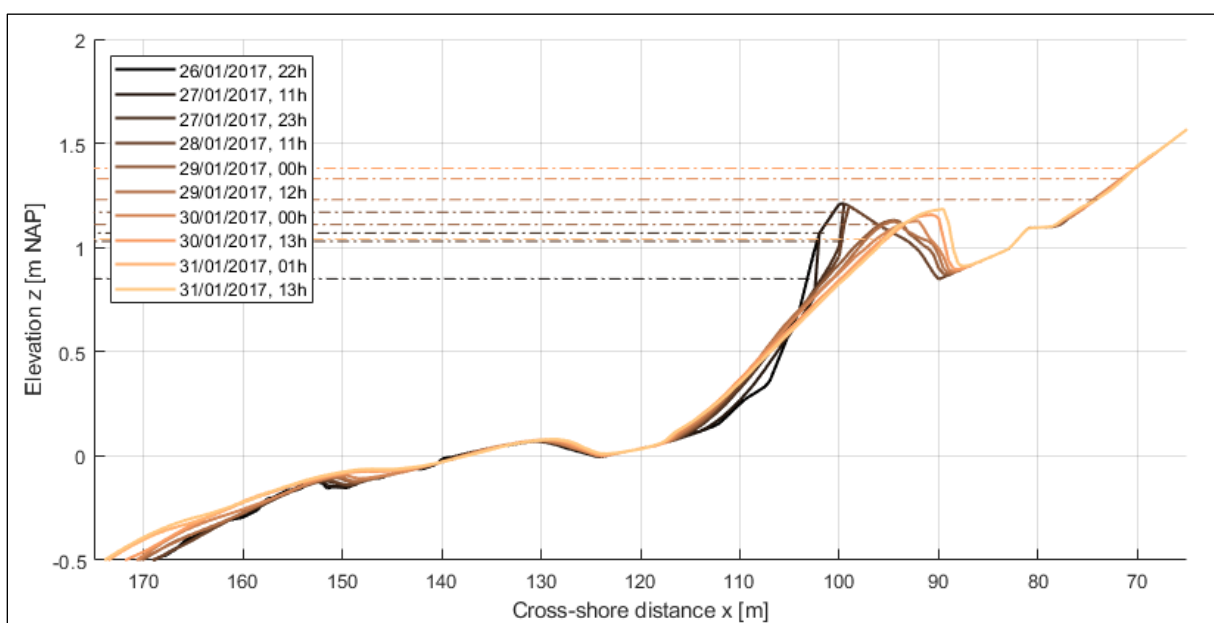


Figure 5-8: Surf beat model simulated low water bed levels at cross section 1 in period B (January 26 to 31, 2017). The dashed dotted lines indicate the still high water level (including surge) after each subsequent low water period.

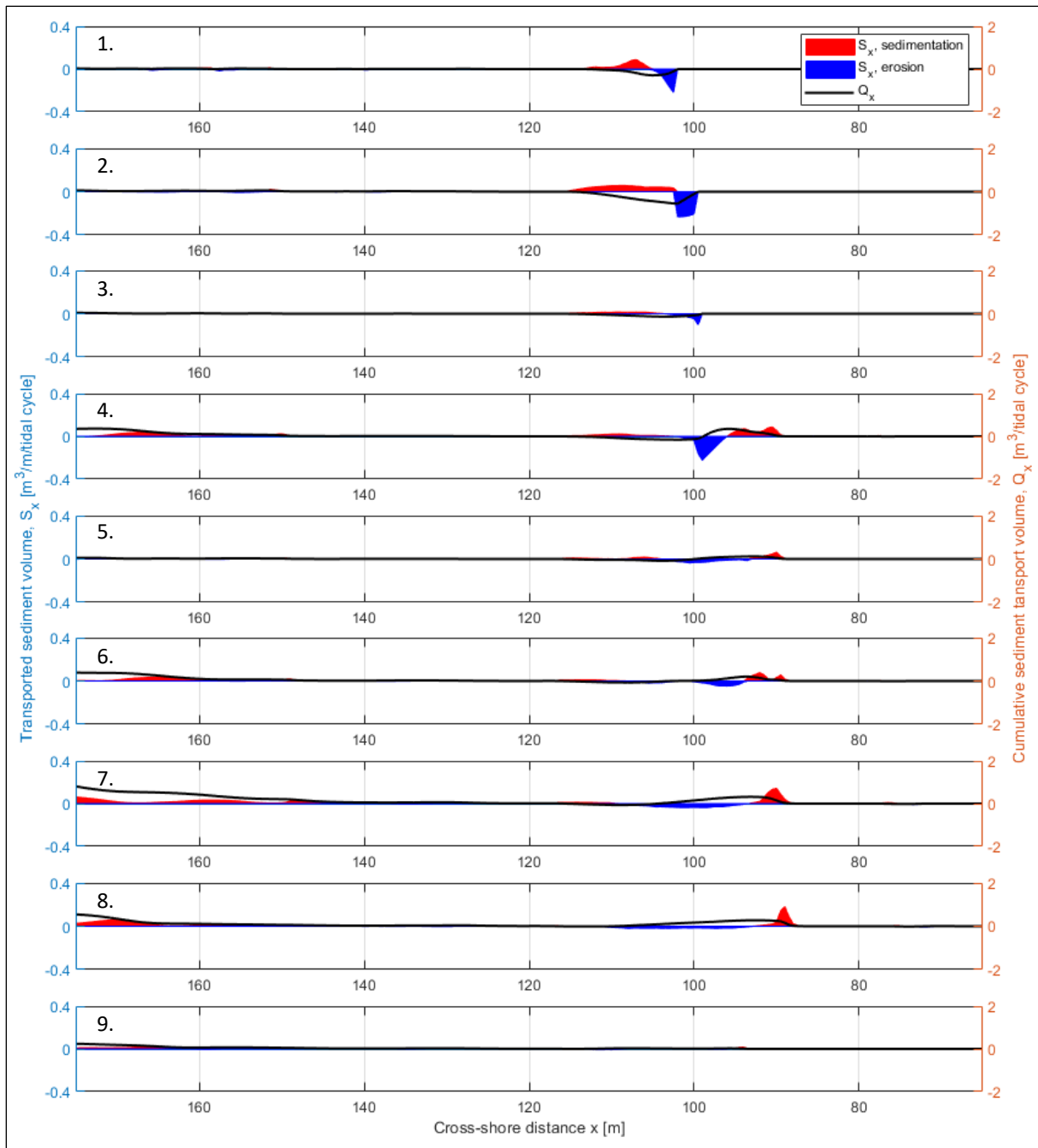


Figure 5-9: Surf beat model simulated sediment transport volumes S_x and cumulative sediment transport volumes Q_x for nine tidal cycles in period B (January 26 to 31, 2017).

5.3.2. Hydrostatic swash model

Bed level development and sediment transport volumes

In the hydrostatic swash model, the upper intertidal bar migrates onshore over a distance of 5m and the bar crest height grows in vertical direction with 0.3m, as shown in Figure 5-10. In the first five tidal cycles, the morphological change is small and the sandbar merely grows with a height of 0.1m. In the next three tidal cycles, the sediment transport is larger as shown in Figure 5-11. The seventh and eighth tidal cycles contain relatively large sediment transport volumes (S_x) of up nearly 0.4 m³/m per meter width, reaching an onshore flux (Q_x) of about 0.6 m³ per meter width. In these tidal cycles the sandbar clearly narrows creating a peaked crest with a seaward and landward slope of about 0.15.

The sediment transport at the intertidal bar occurs while the bar crest remains above the tidal water level. The dashed dotted lines in Figure 5-10 indicate the highest still water level after each low water period. This water level does not rise above the bar crest. It can therefore be concluded that swash zone processes are prevailing. Sediment-laden uprush overtops the bar crest and is deposited on top and at the landward side of the crest. This results in the onshore migration and growth of the intertidal bar. From Figure 5-11, it can be observed that the sediment transport is primarily in onshore direction ($Q_x > 0$, around $x = 100\text{m}$). The intertidal zone does not lose or gain sediment during the simulation period as the sediment budget is closed at the offshore boundary ($Q_x = 0$).

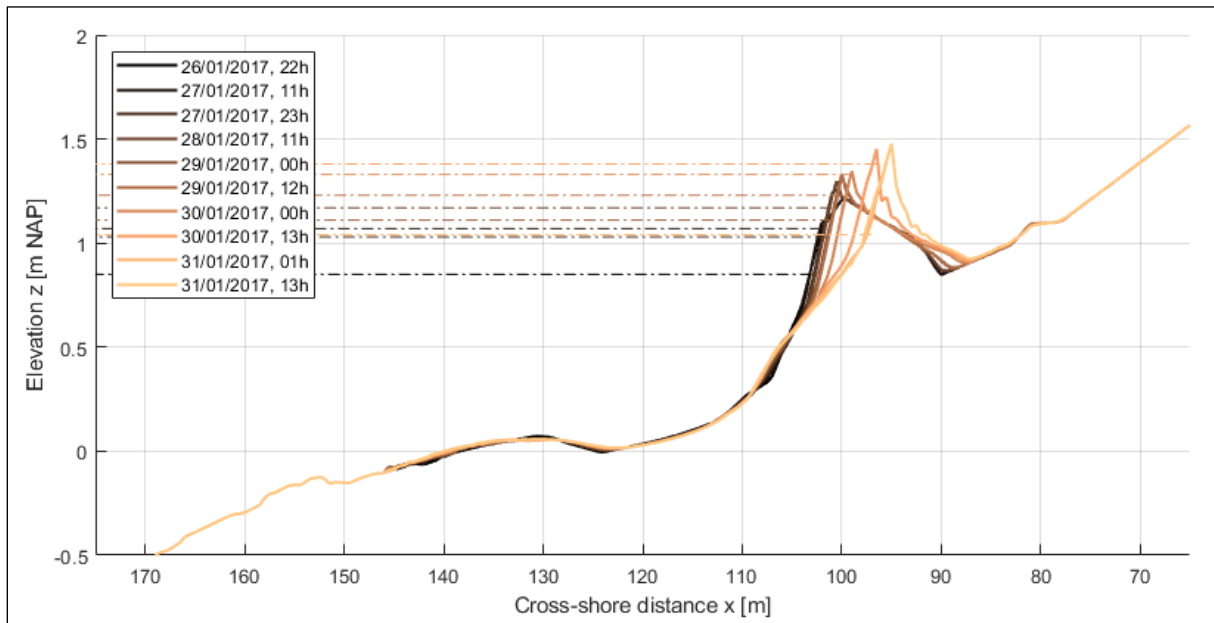


Figure 5-10: Hydrostatic swash model simulated low water bed levels at cross section 1 in period B (January 26 to 31, 2017). The dashed dotted lines indicate the still high water level (including surge) after each subsequent low water period.

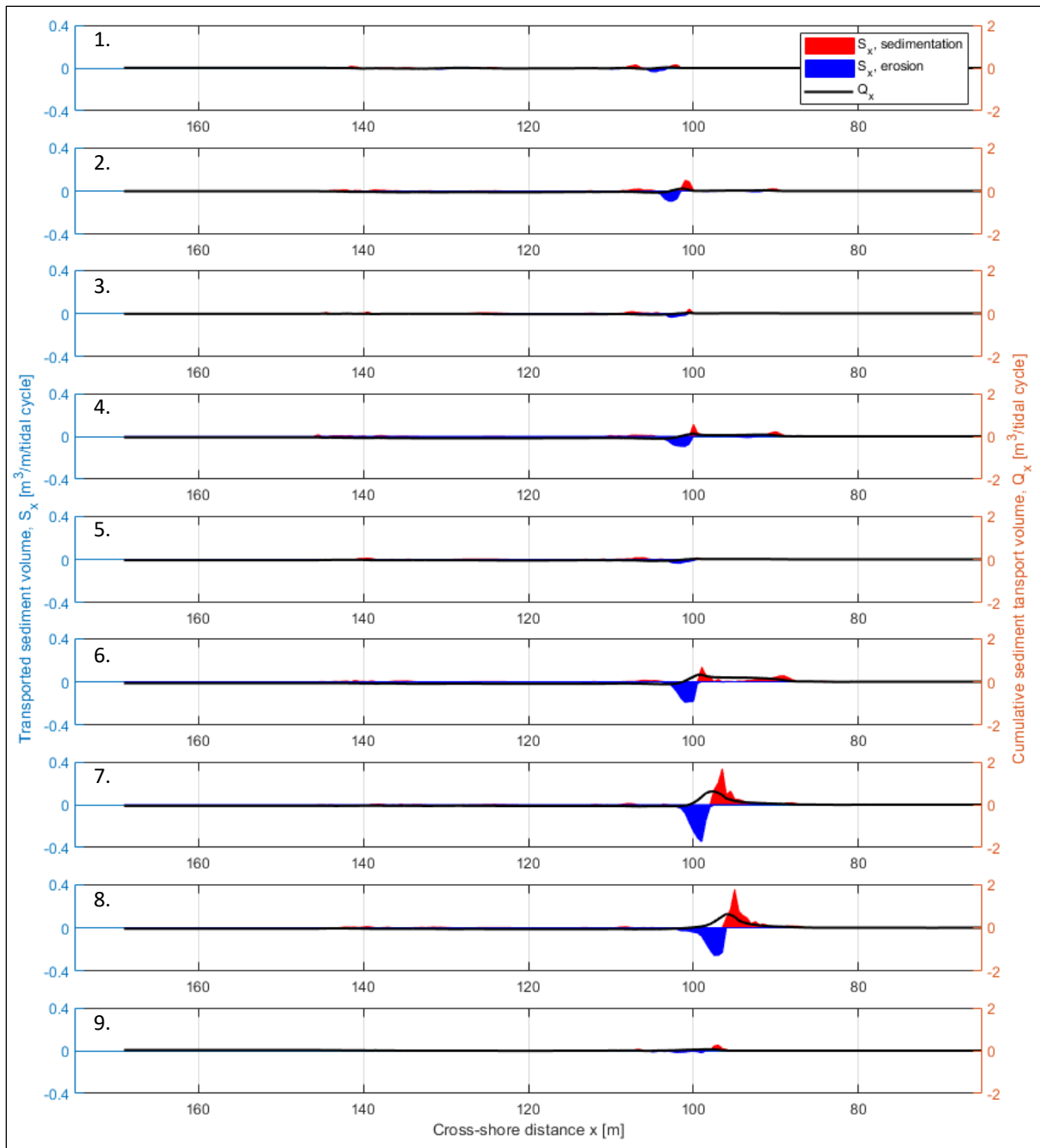


Figure 5-11: Hydrostatic swash model simulated sediment transport volumes S_x and cumulative sediment transport volumes Q_x for nine tidal cycles in period B (January 26 to 31, 2017).

5.3.3. XBeach model performance

In this section, the morphological changes of the XBeach models are compared with respect to the observed TLS measurement results, for both the surf beat and the hydrostatic swash model.

Surf beat model

The results of the surf beat model show some similar patterns, but largely different magnitudes compared with the TLS measurement results. Both results show an onshore migration of the intertidal bar, although with a different magnitude. From Figure 5-12 it can clearly be observed that the onshore migration and growth in the surf beat model cannot keep up with the bar movements in the measurement results. According to the measurements the bar migrates onshore over a cross-shore distance of 25m, whereas in the surf beat model a migration distance of 10m is observed. Moreover, the bar crest

height in the surf beat model slightly decreases, while it grows vertically with a height of 0.3m in the measurement results. These dissimilarities are the results of different sediment transport volumes. Where the onshore flux reaches up to nearly 2 m^3 per meter width in a tidal cycle according to the measurements, the maximum onshore flux in the surf beat model is just over 0.5 m^3 per meter width.

The onshore sediment transport in the second half of the simulation period is mainly induced by surf zone processes in the surf beat model, while swash zone processes are prevailing according to the observations of the TLS measurements. The slow growth and onshore migration in the second half of the simulation period primarily occurs while the tidal water level is located above the crest of the bar. This indicates that the surf zone processes are the dominate sediment transporting processes. In the observation of the TLS measurements it is shown that the tidal water level does not rise above the bar crest, which can also be observed in Figure 5-12 (indicated by the dashed dotted lines). Therefore, it was concluded in section 4.5 that the swash zone processes are prevailing.

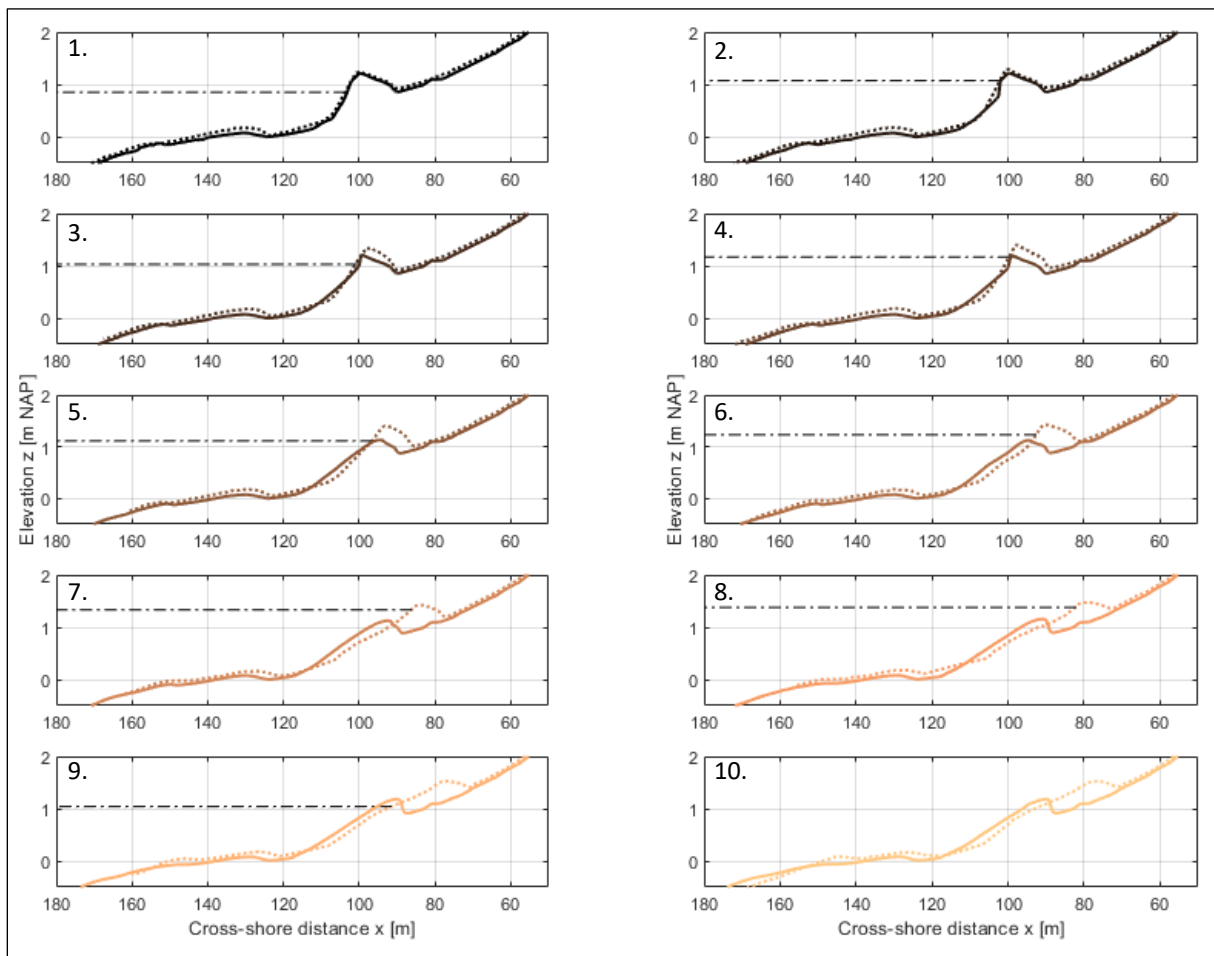


Figure 5-12: Surf beat model simulated (solid lines) and TLS measured (dotted lines) low water bed levels at cross section 1 in period B (January 26 to 31, 2017). The dashed dotted lines indicate the still high water level (including surge) after each subsequent low water period.

Hydrostatic swash model

The results of the hydrostatic swash model show some similar patterns, but with clearly different magnitudes compared to the TLS measurement results. The hydrostatic swash model simulates an onshore migration of the intertidal bar, although with a vastly smaller magnitude as in the measurements. Figure 5-13 shows that the intertidal bar behavior in the hydrostatic swash model cannot keep up with the bar movements in the measurement results. Where according to the measurements the bar migrates onshore over a cross-shore distance of 25m, the migration distance in the hydrostatic swash

model does not reach further than 5m. The simulated and measured bar crest heights match better, with final elevations just under and above +1.5m NAP respectively. Although this crest height is fairly similar, the shape of the sandbar is different. The simulated bar is narrow with steep seaward and landward slopes, whereas the measured bar is broad with relatively flat slopes. These dissimilarities are the results of different sediment transport volumes. Where the onshore flux reaches up to nearly 2 m^3 per meter width in a tidal cycle according to the measurements, the maximum onshore flux in the hydrostatic swash model is about 0.6 m^3 per meter width.

The sediment is mainly transported by swash zone processes, similar to the measurement results. The growth and slow onshore migration of the sandbar occurs while the tidal water level does not rise above the crest. The onshore sediment transport in the hydrostatic swash model is therefore mainly induced by swash zone processes. During the seventh tidal cycle the water level nearly reaches the bar crest height such that surf zone processes might also become important.

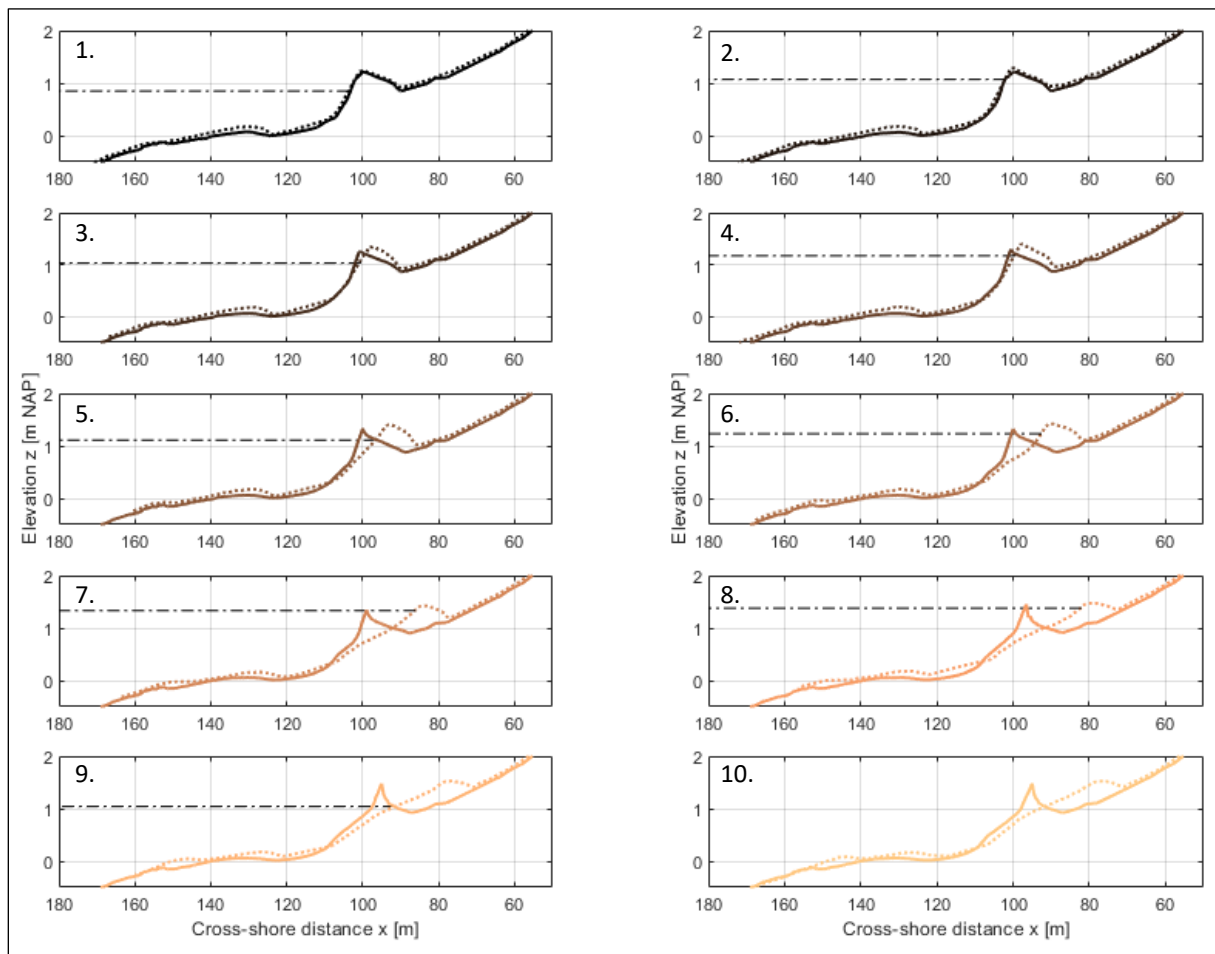


Figure 5-13: Hydrostatic swash model simulated (solid lines) and TLS measured (dotted lines) low water bed levels at cross section 1 in period B (January 26 to 31, 2017). The dashed dotted lines indicate the still high water level (including surge) after each subsequent low water period.

5.4. Conclusion

Based on this chapter an answer is given to sub-question 3, described below.

SQ3: What is the performance of the XBeach model with respect to the TLS measurement results?

In a period of 5 days (period B) the morphological changes in the surf beat model and the hydrostatic swash model show similar patterns but largely different magnitudes. As shown in Table 5-3, the surf beat model corresponds better to the measurements regarding to the onshore migration distance. However, the hydrostatic swash model shows a better match with the TLS measurements regarding the vertical growth of the intertidal bar. Finally, the maximum onshore sediment flux is similar for the surf beat model and the hydrostatic swash model, with values of about four times smaller than the maximum onshore flux of nearly 2 m³ per meter width observed in the TLS measurements.

	Onshore migration distance [m]	Vertical growth [m]	Maximum onshore flux [m ³ /m width]
TLS measurements	25	0.3	2
Surf beat model	10	-0.1	0.5
Hydrostatic swash model	5	0.3	0.6

Table 5-3: Onshore migration distance, vertical growth and maximum onshore sediment flux of the TLS measurements compared with the surf beat model and hydrostatic swash model for period B (January 26 to 31, 2017).

Comparing the models in relation to the sediment transport processes that drive the onshore transport of sediment, the hydrostatic swash model performs best. The TLS measurements shows that the swash zone processes are dominant for the onshore sediment transport. This is matching the hydrostatic swash model that also shows that the onshore transport is primarily induced by the swash zone processes. However, the dominant driver in the surf beat model are the surf zone processes, especially in the second half of the simulation period.

6. Developing a conceptual model

In this chapter a conceptual model of the intertidal bar dynamics is developed to help visualize its complex behavior. In section 2.4 an initial conceptual model is developed, based on the theory and literature review in chapter 2. This model is further developed and extended in this chapter, mainly based on the observations of the TLS measurements (chapter 4).

The morphological behavior of an intertidal sandbar is largely dependent on the tidal water level and the nearshore wave conditions (Wijnberg and Kroon, 2002; Masselink et al., 2006a) as concluded in chapter 2. In the initial conceptual model, a distinction is made between surf zone and swash zone processes acting on an intertidal bar. Which processes are prevailing depends on the tidal water level with respect to an intertidal bar. This concept is extended here by categorizing the tidal water level into four intertidal bar regimes as presented in Figure 6-1. The intertidal bar regimes are similar to the storm impact regimes proposed by Sallenger (2000), as described in subsection 2.1.3. During a low tidal water level, the **swash regime** prevails, where the runup level (R_{up}) remains below the bar toe (B_{toe}). When the water level increases and the runup level gets above the bar toe, the **runup regime** is reached. With a further increasing water level where the runup level gets higher than the bar crest (B_{crest}) but the rundown level (R_{down}) stays below the bar crest, the **overwash regime** is reached. Finally, for a high water level the **submersion regime** prevails, when also the rundown level is above the bar crest.

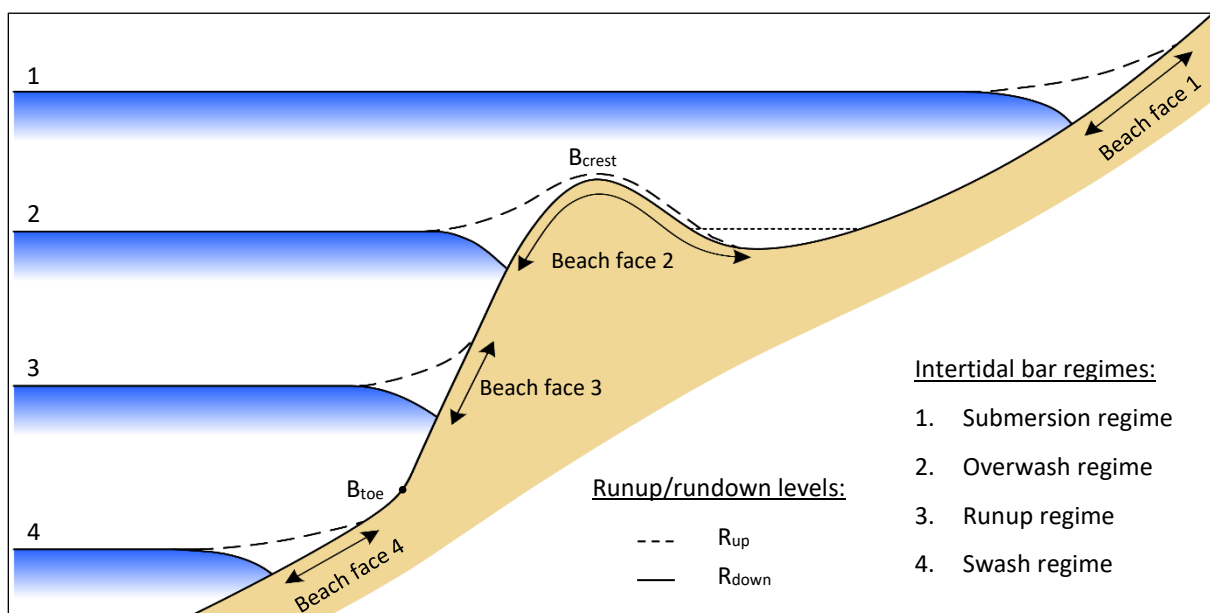


Figure 6-1: Overview of the intertidal bar regimes

Next to the tidal water level, the nearshore wave conditions (mild or energetic) in the surf zone and swash zone are important for determining the behavior of intertidal bars. In the TLS measurement results (section 4.4) the following five distinctive intertidal bar movements are observed:

1. Formation (fast vertical growth)
2. Fast onshore migration
3. Gradual horizontal and vertical growth
4. Fast and short vertical growth and onshore migration
5. Fast destruction

In these movements, four development stages are recognized: **Formation**, **Migration**, **Growth** and **Destruction**. The formation, migration and growth occurred during mild wave conditions while the destruction of the intertidal bars occurred during energetic (storm) wave conditions. Within a regime, the wave conditions in the surf zone and swash zone together with the local bathymetry and the sediment characteristics determine the magnitude and direction of sediment transport based on the dominant cross-shore sediment transport processes.

Combining the observed intertidal bar behavior with the prevailing intertidal bar regime and the wave conditions, the conceptual model presented in Table 6-1 is developed. The five observed intertidal bar movements are classified in this model and indicated by the circled numbers. The conceptual model is explained and described below for each development stage.

Development stage		A. Formation	B. Migration	C. Growth	D. Destruction
Wave conditions		Mild	Mild	Mild	Energetic
Tidal level ↑ HW ↓ LW	1. Submersion regime <i>Intertidal bar dominated by surf zone processes</i>	X	Onshore migration	No (significant) growth	⑤ (Fast) destruction
	2. Overwash regime <i>Intertidal bar dominated by swash zone processes</i>	X	② ④ (Fast) onshore migration	③ ④ Horizontal and/or vertical growth	⑤ Destruction
	3. Runup regime <i>Intertidal bar dominated by swash zone processes</i>	① Formation, if: • Mild wave conditions Figure 6-2a	No migration	③ Horizontal growth	Destruction (avalanching)
	4. Swash regime <i>No sediment transport processes</i>	• Significant tidal range Figure 6-2b	No migration	No growth	No destruction

Table 6-1: Conceptual model on the formation, migration, growth and destruction of an intertidal bar, based on the prevailing regime: swash, runup, overwash or submersion. The development of the intertidal bar might be positive (green), negative (red) or insignificant (white) for beach recovery.

A. Formation

Initially, when no intertidal bar is present, the four intertidal bar regimes cannot be distinguished. Instead the swash or runup regime is considered. For energetic wave conditions the beach face tends to be flattened due to a strong undertow resulting in a net offshore sediment transport (Kroon, 1994; Houser and Greenwood, 2003). In this case an intertidal bar cannot be formed.

An intertidal bar might form during mild wave conditions with a significant tidal range (observed movement 1). For mild wave conditions the beach face tends to steepen, where the net onshore sediment transport is dominant. Ultimately, an equilibrium profile is reached when the wave breaking induced turbulent uprush is balanced by the gravity induced backwash. When the tidal range is insignificant an intertidal bar cannot be formed. The wave action merely results in an equilibrium profile where the beach face is relatively steep and a beach berm is created as depicted in Figure 6-2a. However, when the tidal range is significant (i.e. > 1m, according to Masselink et al. (2006a)), an intertidal bar might form as depicted in Figure 6-2b. With an increasing tidal water level, the wave action moves along the beach profile. Sediment is stirred around the rundown level and transported onshore to the runup level where flow velocities decrease and sediment settles to form an initial intertidal bar.

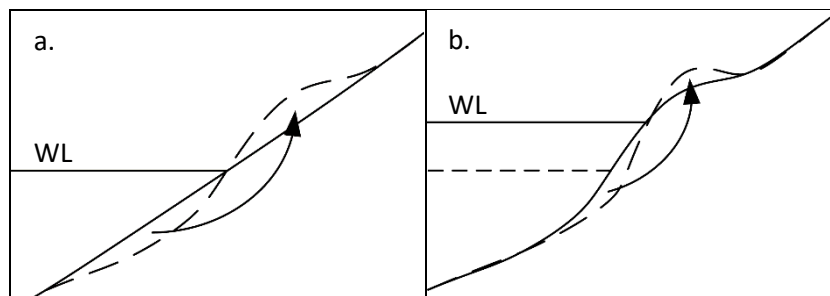


Figure 6-2: Beach face steepening (a) and intertidal bar formation (b). WL = water level.

The duration of the wave action at one location, or in other words the residence time for cross-shore sediment transport processes to occur (Masselink et al., 2006a; Kroon and Masselink, 2002) is important for the formation of the intertidal bar. As described above, an insignificant tidal range does not support the formation of an intertidal bar. In contrast, a large tidal range (macro tidal range) might inhibit the formation. A large tidal range result in a short wave action duration at one location. The formation process can therefore not catch up with the rising tide. Consequently, the area is submerged and different sediment transport processes become dominant.

B. Migration

Once an intertidal bar is formed, four regimes can be distinguished where bar migration can occur within the overwash and submersion regime. In the swash and runup regime, with low tidal water levels, the bar is not migrating. However, in the runup regime the seaward slope of the bar might steepen or flatten depending on the wave conditions.

A (fast) onshore migration might occur in the overwash regime due to swash zone processes, as observed in the TLS measurements (movements 2 and 4). Waves overtop the bar when the still water level is just below the bar crest elevation. Sediment is transported over the crest by wave-breaking induced turbulent uprush changing to gravity induced backwash on the landward site of the bar. Where generally these two processes (uprush and backwash) counteract each other, in the overwash regime they are complementary. This can result in a fast onshore migration. The water that overtops the bar crest might infiltrate the soil or flow back offshore through the trough and rip channels (3D effect). For energetic wave conditions the bar crest might be eroded due to high flow velocities, changing from the overwash to the submersion regime.

Surf zone processes are prevailing in the submersion regime and can also migrate a bar onshore as observed in the surf beat model. In this regime the rundown level remains above the bar crest. Therefore, the swash zone processes occur higher in the profile and do not prevail at the bar. The balance between the surf zone processes determine the magnitude of the on- or offshore migration of the bar. Generally, onshore and offshore migration occurs for mild and energetic wave conditions, respectively. However, during energetic conditions the intertidal bars are generally destructed (Kroon, 1994; Houser and Greenwood, 2003). The offshore migration of intertidal bars in the submersion regime is therefore not included in the conceptual model.

C. Growth

In the runup regime the intertidal bar can grow horizontally, widening the bar (observed movement 3). During mild wave conditions, sediment (in the form of small amplitude bars) can migrate onshore by surf- and swash zone processes. In the runup regime this sediment transport might feed the existing intertidal bar, by welding to the seaward slope due to swash zone processes as observed in the TLS measurements (movement 3).

In the overwash regime the intertidal bar can grow horizontally and vertically (observed movement 3 and 4). Horizontal growth can occur due to surf and swash zone processes. Sediment transported onshore might feed the seaward slope of the bar or might be transported further resulting in vertical growth of the intertidal bar due to swash zone processes. When flow velocities on the bar crest are small, sediment advected from the surf zone and stirred in the uprush might settle, increasing the bar height.

In the submersion regime no significant growth is expected. When the intertidal bar is submerged the surf zone processes are prevailing. Flow velocities are usually relatively large over the bar crest as the water depth is relatively small. Therefore, it is unlikely that sediment will settle on top of the bar crest.

D. Destruction

Destruction of an intertidal bar generally occurs during energetic wave conditions (observed movement 5). In the runup regime destruction of the intertidal bar might occur due to avalanching, as occurred in the simulation of the surf beat model. Sediment is eroded on the seaward slope of the bar. When a critical slope angle is exceeded, sediment is slumping down resulting in destruction of the intertidal bar. In the overwash regime flow velocities over the crest can be large for energetic wave conditions. Sediment gets stirred in the water column decreasing the bar height. Finally, when reaching the submersion regime, the intertidal bar can be destructed fast for energetic wave conditions. Under these conditions the return flow becomes dominant resulting in a strong offshore flow, especially above the bar crest where the water depth is relatively small. Strong offshore sediment transport ultimately flattens the beach resulting in a smooth cross-shore profile of the beach.

Conclusion

Based on this chapter an answer is given to sub-question 4, described below.

SQ 4: How can the intertidal bar behavior be described in a conceptual model?

The intertidal bar behavior observed in the TLS measurements can be described in a conceptual model as presented in Table 6-1. The five distinctive movements of the upper intertidal bar observed in the measurements at Kijkduin are indicated by the circled numbers. In this conceptual model, the behavior of the intertidal bar depends on the tidal level by means of the prevailing intertidal bar regime on one hand, and the wave conditions through the development stage on the other hand.

7. Discussion

In this chapter the results from the TLS measurements (chapter 4) and XBeach models and their comparison (chapter 5) are discussed.

7.1. TLS measurement accuracy

The accuracy of the TLS measurements is sufficient for this research, although some errors occur. In this research the cross-shore morphology is studied and therefore also interpolated and corrected in this direction. Comparing the TLS measurements with the survey of January 2017 indicates height differences in the order of centimeters (as was shown in Figure 5-2) being sufficient for this research. Additional corrections (described in subsection 4.3.6) significantly improved the precision of the scans and reduced erroneous sediment transport volumes.

The cross-shore interpolation (described in subsection 4.3.5) of cross section 1 in period A (6 weeks) and B (5 days) induced some interpolation errors. This can be attributed to the existence of water draining runnels, areas that are too wet to detect or areas that are in the shadow zone of the laser scanner. These errors occur in a few scans throughout the study period, resulting in additional sediment transport volumes between two subsequent scans. Although these errors affect the results, the sediment transport patterns can still clearly be detected. As this is the main objective for the TLS measurements the interpolation errors do not obstruct this research.

7.2. TLS measurement and XBeach model comparison

Based on the theory and the methodology used in this study, arguments for the mismatch between measurement and XBeach model are discussed.

Uncertainty in wave spreading

The wave boundary condition in the surf beat model is defined by a two-dimensional frequency-direction spectrum (an example is shown in Figure 7-1). In this spectrum, the frequency spreading is described by a JONSWAP spectrum shape and the directional spreading by a $\cos^{2s}\theta$ model (Roelvink et al., 2018b), as shown in Figure 7-2. Based on the directional spreading coefficient (s) the directional spreading is defined. From Figure 7-2 it can be observed that the wave direction is limited to 90° on either side of the mean wave direction (as $s \geq 1$). Therefore, no wave energy would approach the coast when the mean wave is directed offshore perpendicular to the shoreline. In practice, the wave spectrum can have a different shape from these frequency and directional distributions leading to different amounts of wave energy approaching the shoreline.

To cope with the uncertainty of the directional spreading, an additional case with increased wave energy is applied for both the surf beat model and the swash zone model. The observed wave conditions at the Europlatform, including the mean wave direction and directional spreading, were applied to the

surf beat and hydrostatic swash model as described in chapter 5. The directional spreading coefficient observed at the Europlatform generally have value $s = 1$ to $s = 3$. This implies a large directional spreading, indicating that the wave energy is approaching over a broad directional space. To see what the result would be if the wave energy is increased, a second wave case is applied. In this case, the maximum possible wave energy approaching the coast would be if the observed waves at the Europlatform are approaching the coast shore normal. This wave condition is therefore applied in the second wave case shown in appendix C, using the same directional spreading as implemented in chapter 5.

From the XBeach results in appendix C it can be observed that the increased wave energy in case 2 does increase the sediment transport volumes significantly. However, sediment is also transported in offshore direction, especially in the surf beat model. Ultimately, the intertidal bar is diffused and destroyed largely in the surf beat model. The morphological changes in the hydrostatic swash model show more promising results. Although the onshore sediment transport volumes found in the TLS measurement results are still nearly two times larger the onshore sediment transport and migration of the intertidal bar is significantly improved for the hydrostatic swash model. Therefore, it might be concluded that the uncertainty in the wave directional spreading could partly contribute to the mismatch.

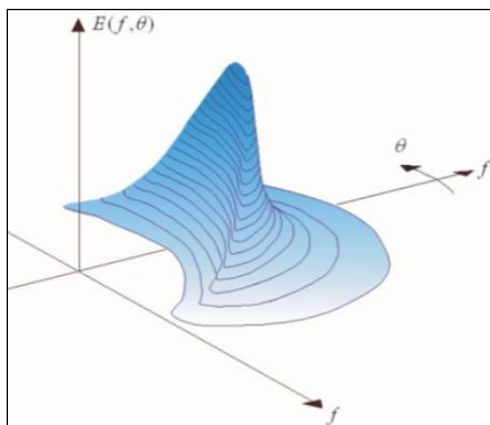


Figure 7-1: Two-dimensional wave frequency-direction spectrum, from (Holthuijsen, 2007).

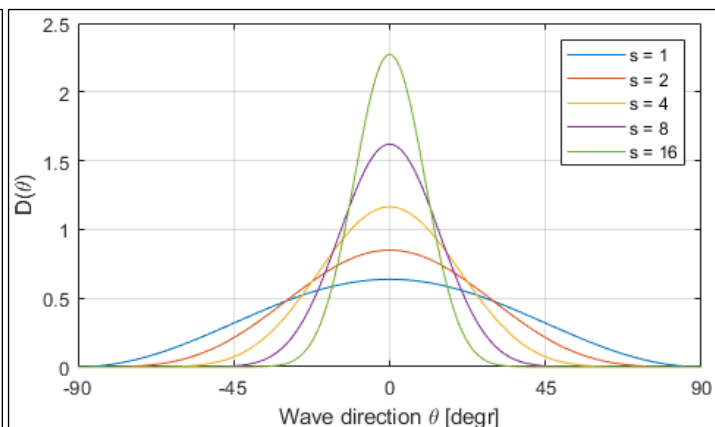


Figure 7-2: Directional spreading as formulated in XBeach.

The frequency spectrum applied to the hydrostatic swash model is described by a TMA spectrum shape approximation. This spectrum approximation might induce several errors in the model. Firstly, the wave energy approaching the coast is overestimated in this approximation. The surface elevation applied at the offshore boundary is obtained from the surf beat model, which transforms waves observed at the Europlatform to the hydrostatic swash model boundary at -0.5m NAP. The obtained waves include the reflected waves which are therefore erroneously applied to the hydrostatic swash model. Another error is induced by missing the wave nonlinearities at the offshore boundary. The TMA spectrum merely applies linear waves to the model, omitting wave skewness and asymmetry at the offshore boundary. An onshore sediment transport component is therefore missing. An attempt was made to include these wave nonlinearities by transforming the observed waves from the Europlatform to the offshore boundary of the hydrostatic swash model using the non-hydrostatic XBeach model. However, the wave energy obtained from this model was significantly lower than obtained from the surf beat model. This might be caused by numerical damping over the relatively long cross-shore distance with over 2000 grid cells. Therefore, this wave condition is not used.

Importance of waves on the short wave timescale

The main difference between the XBeach models is the morphological response on the timescale of short waves and long waves in the hydrostatic swash model and the surf beat model, respectively. The

model results clearly show differences in the intertidal bar behavior. The morphological response in the swash zone model is based on cross-shore sediment transport processes matching best with the measurement results (as concluded in section 5.4). Therefore, it might be stated that the morphological change on the timescale of the (individual) short waves do contribute significantly to the morphological response. However, there are more differences between the models which might explain the different morphological response in the two models. For example, the sediment transport formulations. In the surf beat model the bed load and suspended load are calculated together in a advection-diffusion equation according to Galappatti and Vreugdenhil (1985), whereas in the hydrostatic swash model the bed load and suspended load are calculated separately. The bed load transport is calculated based on the model of Meyer-Peter and Müller (1948) and the suspended load with the same advection-diffusion equation as in the surf beat model. This might lead to different sediment transport volumes and patterns. Moreover, the discharge output implemented in the hydrostatic swash model is not included in the surf beat model. This results in different currents over and behind the bar crest (in the trough) and is discussed next.

3D effects

A discharge outflow point is implemented in the hydrostatic swash model to simulate 3D effects through rip channels. Alongshore variations can induce additional sediment transport in the cross-shore direction. In this case, the alongshore (upper and lower) intertidal bars are disrupted by rip channels inducing 3D effects. In the hydrostatic swash model an attempt to implement this effect is made by including a discharge output at the trough, as described in subsection 5.2.3. This discharge output helps in reducing offshore sediment transport due to return flow over the bar crest, when the overwash or submersion regime prevails. To see the effect of this outflow point, the morphological change is also simulated without the discharge output. The comparison is presented in Figure 7-3, where the black line indicates the initial profile, the brown solid line the final profile of the simulation without a discharge outflow point and the brown dotted line the final profile of the simulation with a discharge outflow point. It can be observed that the onshore sediment transport is larger for the simulation with a discharge outflow. Therefore, the discharge outflow point has a positive effect on the onshore sediment transport.

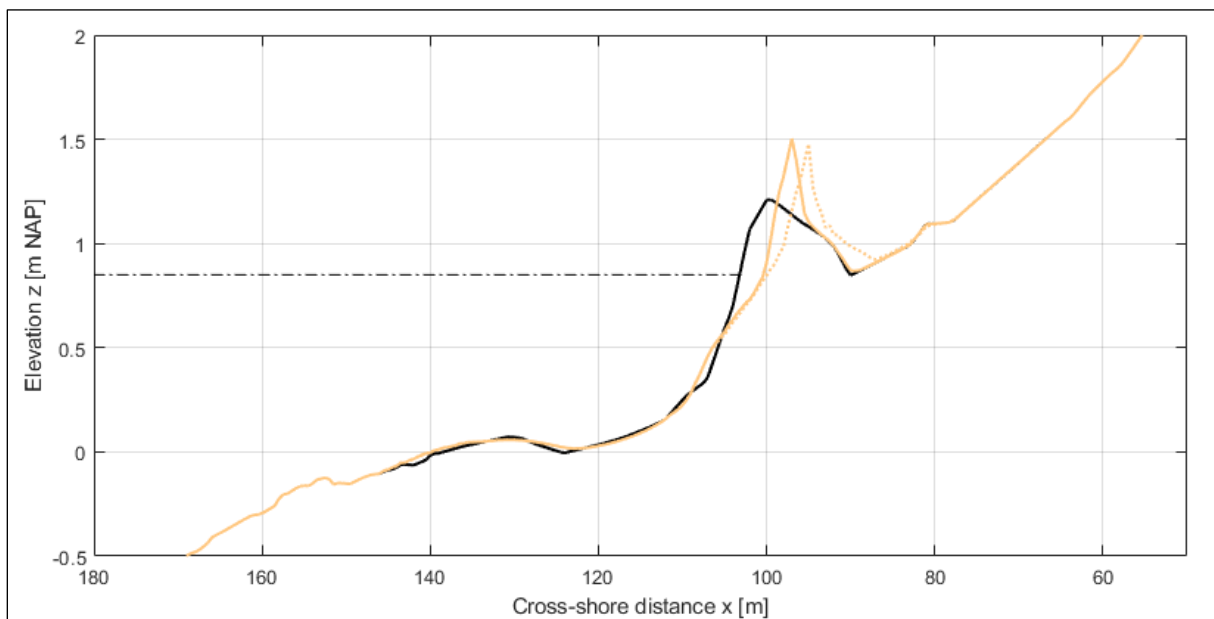


Figure 7-3: Hydrostatic swash model simulated low water bed levels at cross section 1 at the start (black line) and end (brown lines) of period B (January 26 to 31, 2017) for a simulation with (dotted line) and without discharge outflow (solid line). The dashed dotted lines indicate the still high water level (including surge) after the first low water period.

The influence of rip channels with a rising tide and before reaching the overwash regime is not implemented in the hydrostatic swash model. Before the rising tide is reaching the overwash regime, no water is present in the trough in the model simulations. However, in practice the trough is filling up with water flowing around the intertidal bar through the rip channels. The filled up trough with low flow velocities provides the opportunity for sediment, transported by overtopping waves, to settle in the trough and at the landward side of the intertidal bar.

Concluding remarks

Despite of the above mentioned discussions, an additional or enhanced sediment transport component is required to improve the model performance. The onshore migration of the intertidal bar is largely underestimated in the two models. This can partly be explained by the discussion points described above. However, it cannot explain the complete ascertained differences between the models and measurement results. Therefore, onshore sediment transport need to be enhanced in order to approach the TLS measurement results.

8. Conclusion and recommendations

8.1. Conclusion

The main research question stated in section 1.3 is answered in this section based on the four sub-questions answered throughout this thesis at the end of chapter 2 (SQ 1), 4 (SQ 2), 5 (SQ 3) and 6 (SQ 4). The main research question of this thesis was formulated as follows:

What is the cross-shore morphological behavior of intertidal bars at Kijkduin on a timescale of hours to weeks and to what extent can it be reproduced in XBeach?

This study has shown that two distinctive intertidal bars formed, grew and migrated onshore after a storm during mild wave conditions in a period of approximately 6 weeks (period A). Within this period, a fast onshore migration of the upper intertidal bar occurred in less than 5 days (period B) which can partly be reproduced in XBeach.

The cross-shore morphological behavior of the upper intertidal bar in period A can be described in a conceptual model as presented in Table 8-1. While the lower intertidal bar develops more gradually, fed by smaller bars, the upper intertidal bar develops in five distinctive steps: 1. Formation (fast vertical growth); 2. Fast onshore migration; 3. Gradual horizontal and vertical growth; 4. Fast and short vertical growth and onshore migration; 5. Fast destruction. These five development steps are classified in the conceptual model depicted in Table 8-1 (circled numbers).

In period B, the fast onshore migration of the upper intertidal bar (distinctive movement 2 in period A) can largely be explained by sediment transport due to swash zone processes. In nine tidal cycles the upper bar grows vertically with a height of 0.3m and moves onshore over a cross-shore distance of 25m. Sediment is transported onshore up to nearly 2 m³ per meter width in one tidal cycle. The sediment is primarily transported from the seaward side to the landward side of the bar when the overwash regime prevails (see Table 8-1). The onshore migration of the intertidal bar can therefore be attributed to swash zone processes. Sediment is transported over the bar crest due to turbulent uprush (induced by wave-breaking) and continues at the landward site of the bar by (gravity induced) backwash.

Two hydrodynamic model options in XBeach, the surf beat model and the hydrostatic swash model, partly reproduce the morphological behavior of the upper intertidal bar. The onshore migration of the bar in the surf beat model is mainly induced by surf zone processes, not matching the results of the measurements. In contrast, the hydrostatic swash model shows onshore migration and vertical growth primarily induced by swash zone processes, comparable to the processes in the TLS measurements. However, for both models the onshore sediment transport is vastly smaller than observed in the TLS measurements and the maximum onshore fluxes are about four times smaller.

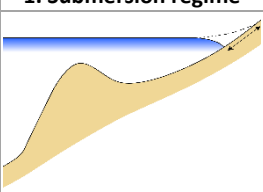
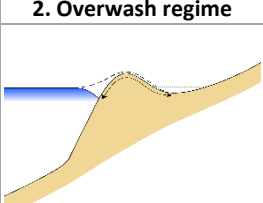
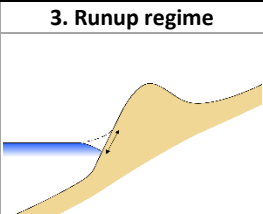
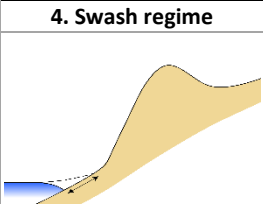
Development stage:		A. Formation	B. Migration	C. Growth	D. Destruction
Wave conditions:		Mild	Mild	Mild	Energetic
Tidal level ↑ HW ↓ LW	1. Submersion regime 	X	Onshore migration	No (significant) growth	⑤ (Fast) destruction
	2. Overwash regime 	X	② ④ (Fast) onshore migration	③ ④ Horizontal and/or vertical growth	⑤ Destruction
	3. Runup regime 	① Formation	No migration	③ Horizontal growth	Destruction (avalanching)
	4. Swash regime 	Formation	No migration	No growth	No destruction

Table 8-1: Conceptual model on the formation, migration, growth and destruction of an intertidal bar, based on the prevailing regime: swash, runup, overwash or submersion. The development of the intertidal bar might be positive (green), negative (red) or insignificant (white) for beach recovery.

8.2. Recommendations

This study has provided more insight into the onshore sediment transport through intertidal bars using TLS measurements. Its reproducibility in a numerical model has been tested by using two hydrodynamic options in XBeach, the surf beat model and the hydrostatic swash model. Some recommendations are made here to further improve the understanding of the beach recovery behavior through intertidal bars and to further improve the reproducibility in a numerical model like XBeach.

Additional data for TLS measurement campaigns

The TLS measurement presented in this thesis provided accurate results, which clearly showed the sediment patterns. However, for the quantification of sediment transport it might be useful to further increase the accuracy and precision of the TLS measurements such that no additional corrections need to be made, as performed in this study (section 4.3.6). This could be done by applying additional reference points for Geo-Referencing, especially in the direction shore normal to the coastline.

New TLS measurement campaigns can give more insight in the circumstances in which intertidal bars develop and migrate, further improving the conceptual model. When a new measuring campaign is setup, additional data would be useful besides the TLS data. One example is nearshore wave data. When nearshore wave data (wave height, wave period and wave direction) is available the development of an intertidal bar might be correlated more accurately with the wave conditions that prevail. Moreover, the sensitivity to changing wave conditions might be investigated. Next to a better understanding of the intertidal bar behavior, also the boundary conditions applied to a numerical model are more accurate when nearshore wave data is available. Therefore, the uncertainties in the wave conditions discussed in chapter 7 are decreased.

The TLS measurements can also be assisted by video recording or photogrammetry. These methods might help in detecting wave overtopping and runup levels. As the laser scanner cannot detect submerged or wet areas, video recording or photogrammetry can fill in this gap. Moreover, it is not known to what extent the laser scanner does detect a wet beach surface. Therefore, imaging can determine the applicability of laser scanning on these (partly) wet areas more distinctively.

Extending and improving the modelling work

In this case the morphological response is simulated in cross-shore direction. Longshore variations however, might also contribute to the behavior of intertidal bars as discussed in chapter 7. Therefore, 2D modelling in XBeach can give a more complete result of the morphological response including the 2D effects in a depth-averaged sense.

Further developing the non-hydrostatic model can be beneficial for the reproduction of intertidal bar behavior. As was stated in subsection 5.1.1 the non-hydrostatic model is not used in this thesis as the morphodynamics for sandy beaches are not yet fully integrated and validated in that model. When this would be accomplished, the intertidal bar behavior might be modelled more accurately. The offshore boundary conditions from the Europlatform can be applied in deeper water (compared to the hydrostatic swash model) as a two layer system is implemented in the model and a non-hydrostatic pressure term is added. Similar to the hydrostatic swash model, both short waves and long waves are included which can both be important for the intertidal bar response.

The onshore sediment transport is clearly underestimated by the surf beat model and hydrostatic swash model. Further research need to be done to improve the reproducibility and enhance the onshore sediment transport.

Bibliography

- Aagaard, T., Greenwood, B. & Hughes, M. 2013. Sediment transport on dissipative, intermediate and reflective beaches. *Earth-science reviews*, 124, 32-50.
- Anders, K., Lindenbergh, R.C., Vos, S., Mara, H., de Vries, S. & Höfle, B. in press. High-frequency 3D geomorphic observation using hourly terrestrial laser scanning data of a sandy beach.
- Bailard, J.A. 1981. An energetics total load sediment transport model for a plane sloping beach. *Journal of Geophysical Research: Oceans*, 86, 10938-10954.
- Bakhtyar, R., Barry, D.A., Li, L., Jeng, D.S. & Yeganeh-Bakhtiary, A. 2009. Modeling sediment transport in the swash zone: A review. *Ocean Engineering*, 36, 767-783.
- Bosboom, J. & Stive, M.J. 2015. *Coastal Dynamics I: Lectures Notes CIE4305*, VSSD.
- Bouws, E., Günther, H., Rosenthal, W. & Vincent, C. 1985. Similarity of the wind wave spectrum in finite depth water: 1. Spectral form. *Journal of Geophysical Research: Oceans*, 90, 975-986.
- Cohn, N., Anderson, D. & Ruggiero, P. 2015. Observations of intertidal bar welding along a high energy, dissipative coastline. *The Proceedings of the Coastal Sediments 2015*. World Scientific.
- Cohn, N., Hoonhout, B.M., Goldstein, E.B., De Vries, S., Moore, L.J., Durán Vincent, O. & Ruggiero, P. 2019. Exploring Marine and Aeolian Controls on Coastal Fore-dune Growth Using a Coupled Numerical Model. *Journal of Marine Science and Engineering*, 7, 13.
- Cohn, N., Ruggiero, P., de Vries, S. & García-Medina, G. Beach growth driven by intertidal sandbar welding. *Proceedings of the Coastal Dynamics Conference*, 2017. 1059-1069.
- Cowell, P.J., Stive, M.J., Niedoroda, A.W., de Vriend, H.J., Swift, D.J., Kaminsky, G.M. & Capobianco, M. 2003. The coastal-tract (part 1): a conceptual approach to aggregated modeling of low-order coastal change. *Journal of Coastal Research*, 812-827.
- Dashtgard, S.E., MacEachern, J.A., Frey, S.E. & Gingras, M.K. 2012. Tidal effects on the shoreface: towards a conceptual framework. *Sedimentary Geology*, 279, 42-61.
- Dawson, J.C., Davidson-Arnott, R.G. & Ollerhead, J. 2002. Low-energy morphodynamics of a ridge and runnel system. *Journal of Coastal Research*, 36, 198-215.
- Deigaard, R., Jakobsen, J.B. & Fredsøe, J. 1999. Net sediment transport under wave groups and bound long waves. *Journal of Geophysical Research: Oceans*, 104, 13559-13575.
- Elfrink, B. & Baldock, T. 2002. Hydrodynamics and sediment transport in the swash zone: a review and perspectives. *Coastal Engineering*, 45, 149-167.
- Elgar, S., Gallagher, E.L. & Guza, R. 2001. Nearshore sandbar migration. *Journal of Geophysical Research: Oceans*, 106, 11623-11627.
- Elgar, S. & Guza, R. 1985. Observations of bispectra of shoaling surface gravity waves. *Journal of Fluid Mechanics*, 161, 425-448.

-
- Galappatti, G. & Vreugdenhil, C. 1985. A depth-integrated model for suspended sediment transport. *Journal of Hydraulic Research*, 23, 359-377.
- GmbH, R.L.M.S. 2017. *Datasheet Riegl VZ-2000* [Online]. Available: <https://www.3dlasermapping.com/riegl-terrestrial-laser-scanners/> [Accessed].
- Grasmeijer, B.T. 2002. *Process-based cross-shore modelling of barred beaches*.
- Guza, R.T. & Inman, D.L. 1975. Edge waves and beach cusps. *Journal of Geophysical Research*, 80, 2997-3012.
- Hobbelen, R. 2018. Mapping sub-annual beach growth using terrestrial laser scanning: A study on the application of terrestrial laser scanning on small scale beach variability, to quantify beach resilience on sub-annual time scale.
- Holthuijsen, L.H. 2007. Waves in Oceanic and Coastal Waters. *Waves in Oceanic and Coastal Waters, by Leo H. Holthuijsen, pp. 404. Cambridge University Press, January 2007. ISBN-10: . ISBN-13:, 404.*
- Hoonhout, B. 2015. *XBeach Matlab Toolbox (reference)* [Online]. Available: https://xbeach.readthedocs.io/en/latest/matlab_toolbox.html#xb-grid-xgrid [Accessed].
- Hoonhout, B. & de Vries, S. 2017. Field measurements on spatial variations in aeolian sediment availability at the Sand Motor mega nourishment. *Aeolian Research*, 24, 93-104.
- Houser, C. 2009. Synchronization of transport and supply in beach-dune interaction. *Progress in Physical Geography*, 33, 733-746.
- Houser, C. & Greenwood, B. Response of a swash bar to a sequence of storms. *Proceedings Coastal Sediments*, 2003.
- Isenburg, M. 2018. *LAStools - efficient LiDAR processing software* [Online]. Available: <https://rapidlasso.com/lastools/> [Accessed].
- Jensen, S.G., Aagaard, T., Baldock, T.E., Kroon, A. & Hughes, M. 2009. Berm formation and dynamics on a gently sloping beach; the effect of water level and swash overtopping. *Earth Surface Processes and Landforms*, 34, 1533-1546.
- Kroon, A. 1994. *Sediment transport and morphodynamics of the beach and nearshore zone near Egmond, the Netherlands*.
- Kroon, A. & Masselink, G. 2002. Morphodynamics of intertidal bar morphology on a macrotidal beach under low-energy wave conditions, North Lincolnshire, England. *Marine geology*, 190, 591-608.
- Longuet-Higgins, M.S. 1953. Mass transport in water waves. *Phil. Trans. R. Soc. Lond. A*, 245, 535-581.
- Luijendijk, A.P., Ranasinghe, R., de Schipper, M.A., Huisman, B.A., Swinkels, C.M., Walstra, D.J. & Stive, M.J. 2017. The initial morphological response of the Sand Engine: A process-based modelling study. *Coastal engineering*, 119, 1-14.
- Masselink, G., Kroon, A. & Davidson-Arnott, R. 2006a. Morphodynamics of intertidal bars in wave-dominated coastal settings—a review. *Geomorphology*, 73, 33-49.

-
- Masselink, G. & Puleo, J.A. 2006b. Swash-zone morphodynamics. *Continental Shelf Research*, 26, 661-680.
- Meyer-Peter, E. & Müller, R. Formulas for bed-load transport. IAHSR 2nd meeting, Stockholm, appendix 2, 1948. IAHR.
- Osborne, P.D. & Greenwood, B. 1993. Sediment suspension under waves and currents: time scales and vertical structure. *Sedimentology*, 40, 599-622.
- Puleo, J., Beach, R., Holman, R.A. & Allen, J. 2000. Swash zone sediment suspension and transport and the importance of bore-generated turbulence. *Journal of Geophysical Research: Oceans*, 105, 17021-17044.
- Reniers, A., Gallagher, E., MacMahan, J., Brown, J., Van Rooijen, A., de Vries, J.v.T. & Van Prooijen, B. 2013. Observations and modeling of steep-beach grain-size variability. *Journal of Geophysical Research: Oceans*, 118, 577-591.
- Reniers, A.J., Roelvink, J. & Thornton, E. 2004. Morphodynamic modeling of an embayed beach under wave group forcing. *Journal of Geophysical Research: Oceans*, 109.
- Ribberink, J.S. 1998. Bed-load transport for steady flows and unsteady oscillatory flows. *Coastal Engineering*, 34, 59-82.
- Rijksoverheid 2017. Water in kaart 2017.
- Roelvink, D., McCall, R., Mehvar, S., Nederhoff, K. & Dastgheib, A. 2018a. Improving predictions of swash dynamics in XBeach: The role of groupiness and incident-band runup. *Coastal Engineering*, 134, 103-123.
- Roelvink, D., Reniers, A., Van Dongeren, A., Van Thiel de Vries, J., McCall, R. & Lescinski, J. 2009. Modelling storm impacts on beaches, dunes and barrier islands. *Coastal engineering*, 56, 1133-1152.
- Roelvink, D., Van Dongeren, A., McCall, R., Hoonhout, B., Van Rooijen, A., Van Geer, P., De Vet, L., Nederhoff, K. & Quataert, E. 2018b. XBeach Documentation - Release XBeach v1.23.5527 XBeachX FINAL. *Delft, The Netherlands: Deltares, Technical report*.
- Roelvink, J.A. & Stive, M.J.F. 1989. Bar-generating cross-shore flow mechanisms on a beach. *Journal of Geophysical Research: Oceans*, 94, 4785-4800.
- Ruessink, B., Kuriyama, Y., Reniers, A., Roelvink, J. & Walstra, D. 2007. Modeling cross-shore sandbar behavior on the timescale of weeks. *Journal of Geophysical Research: Earth Surface*, 112.
- Rusu, R.B., Marton, Z.C., Blodow, N., Dolha, M. & Beetz, M. 2008. Towards 3D point cloud based object maps for household environments. *Robotics and Autonomous Systems*, 56, 927-941.
- Sallenger, A.H. 2000. Storm impact scale for barrier islands. *Journal of Coastal Research*, 16.
- Short, A.D. 1992. Beach systems of the central Netherlands coast: processes, morphology and structural impacts in a storm driven multi-bar system. *Marine Geology*, 107, 103-137.
- Soulsby, R. 1997. *Dynamics of marine sands: a manual for practical applications*, Thomas Telford.

- Steetzel, H. 1993. Cross-shore Transport during Storm Surges.
- Sunamura, T. & Takeda, I. 1984. Landward migration of inner bars. *Marine Geology*, 60, 63-78.
- Svendsen, I.A. 1984. Mass flux and undertow in a surf zone. *Coastal Engineering*, 8, 347-365.
- Trouw, K.J.M., Zimmermann, N., Mathys, M., Delgado, R. & Roelvink, D. 2012. Numerical modelling of hydrodynamics and sediment transport in the surf zone: a sensitivity study with different types of numerical models. *Coastal Engineering Proceedings*, 1, 23.
- Van Geer, P., den Bieman, J., Hoonhout, B. & Boers, M. 2015. XBeach 1D—Probabilistic model: ADIS, Settings, Model uncertainty and Graphical User Interface. *Tec. Rep*, 1209436-002.
- Van Houwelingen, S. 2004. *Spatial and temporal variability in ridge and runnel morphology along the North Lincolnshire Coast, England*. PhD thesis (unpublished), Loughborough University.
- Van Koningsveld, M., De Boer, G., Baart, F., Damsma, T., Den Heijer, C., Van Geer, P. & De Sonnevile, B. OpenEarth-inter-company management of: data, models, tools & knowledge. Proceedings WODCON XIX Conference: Dredging Makes the World a Better Place, 9-14 September 2010, Beijing, China, 2010.
- van Rijn, L.C. 2007. Unified view of sediment transport by currents and waves: part I and II. *Journal of Hydraulic Engineering*, 133, 668-689.
- Van Thiel de Vries, J. 2009. Dune erosion during storm surges.
- van Thiel de Vries, J., Van Gent, M., Walstra, D. & Reniers, A. 2008. Analysis of dune erosion processes in large-scale flume experiments. *Coastal Engineering*, 55, 1028-1040.
- Verhagen, H. 1990. Coastal Measurements in the Netherlands. *Manuscript*.
- Vos, S., Lindenbergh, R. & de Vries, S. 2017. Coastscan: Continuous monitoring of coastal change using terrestrial laser scanning. *Coastal Dynamics 2017*.
- Vosselman, G. & Maas, H.-G. 2010. *Airborne and terrestrial laser scanning*, CRC.
- Walstra, D. & Van Rijn, L. 2003. Modeling of sand transport in Delft3D. *Report Z3624. WL/Delft Hydraulics, Delft*.
- Weger, R.d. 2017. Veldrapportage #39 Januari 2017, post-storm Monitoring Zandmotor Morfologie.
- Wijnberg, K.M. & Kroon, A. 2002. Barred beaches. *Geomorphology*, 48, 103-120.
- Wijsman, J.W.M. & Verduin, E. 2011. To monitoring Zandmotor Delflandse kust: benthos ondiepe kustzone en natte strand. IMARES.
- Wright, L. & Short, A.D. 1984. Morphodynamic variability of surf zones and beaches: a synthesis. *Marine geology*, 56, 93-118.
- Zhang, K., Chen, S.-C., Whitman, D., Shyu, M.-L., Yan, J. & Zhang, C. 2003. A progressive morphological filter for removing nonground measurements from airborne LIDAR data. *IEEE transactions on geoscience and remote sensing*, 41, 872-882.

A. Laser scanner details

The Riegl-VZ2000 laser scanner is equipped with the LiDAR (Light Detection And Ranging) sensor technology. A single (near infrared) laser pulse is emitted and is reflected on a surface spot, back to the receiver. The two way travel time of the pulse is converted in a range distance using the speed of light. In this way, the position of the detected (reflection) point is determined with respect to the laser scanner (Vosselman and Maas, 2010). Additionally, the strength of the reflected pulse is measured which is referred to as the reflectance. This might give an indication on the type of surface. All the detected points together form a point cloud including the reflectance and the 3D point coordinates with respect to the laser scanner.

The accuracy and precision of the laser scanner are respectively 8 and 5 mm (GmbH, 2017). These characteristics give the opportunity to detect small scale height profile changes between subsequent scans. Furthermore, the level of detail of the scans and the size of the data is determined by the angular resolution. Higher resolution leads to more detail, which comes with larger data files and therefore a higher computational effort. In this case the resolution is set such that the data size is kept low and workable. Consequently, the visibility of the two reference points in the dune area (red points in Figure 4-2) is bad and the center could not be detected accurately. These reference points are therefore excluded for Geo-Referencing the point clouds.

B. TLS measurement results for cross sections 2 and 3

This appendix shows the results of two more cross sections, besides cross section 1. In section 4.2 the longshore location of cross section 2 and 3 are described and depicted in Figure 4-4. The bed level development and sediment transport volumes in period B (January 26 to 31, 2017) for these cross sections are depicted in the figures below.

Bed level development

Cross section 2

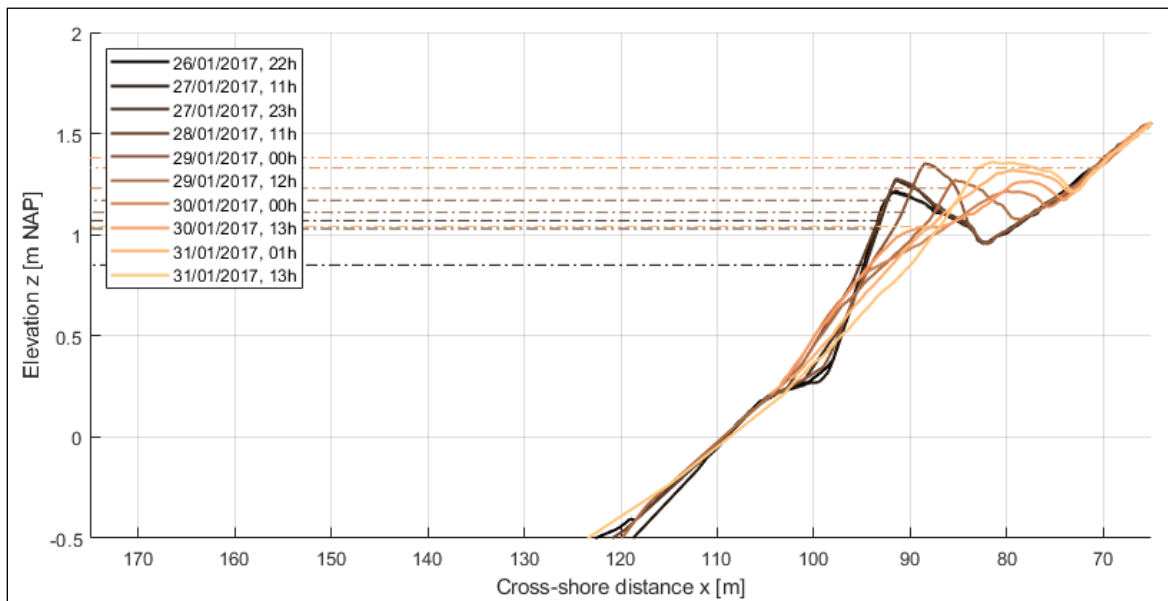


Figure B-1: Low water bed levels at cross section 2, from January 26 to 31, 2017. The dashed dotted lines indicate the still high water level (including surge) after each subsequent low water period.

Cross section 3

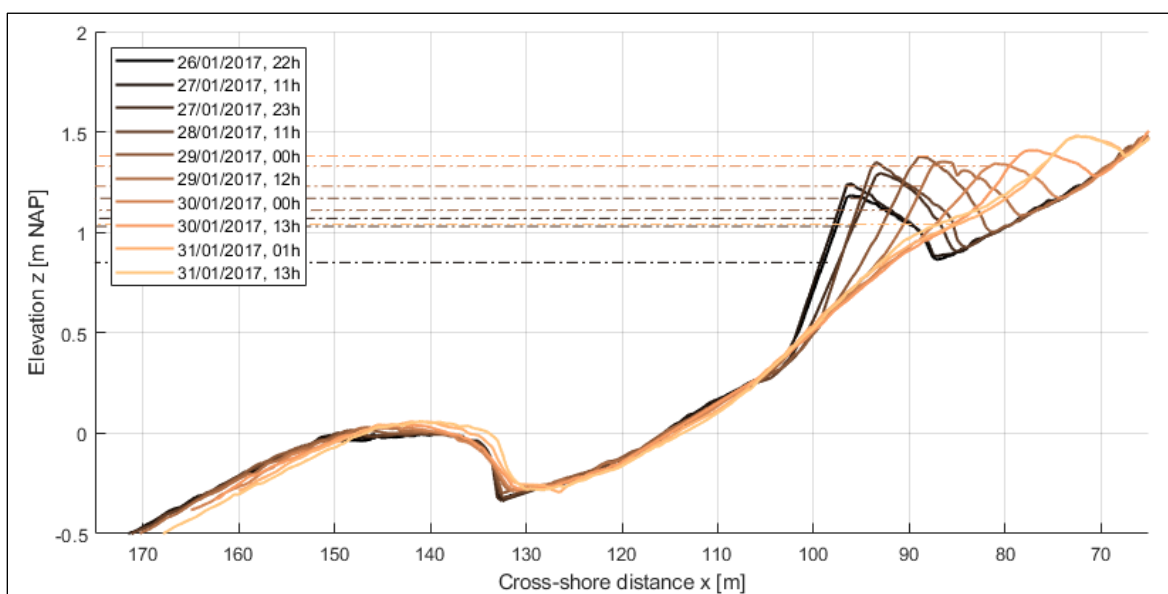


Figure B-2: Low water bed levels at cross section 3, from January 26 to 31, 2017. The dashed dotted lines indicate the still high water level (including surge) after each subsequent low water period.

Sediment transport volumes

Cross section 2

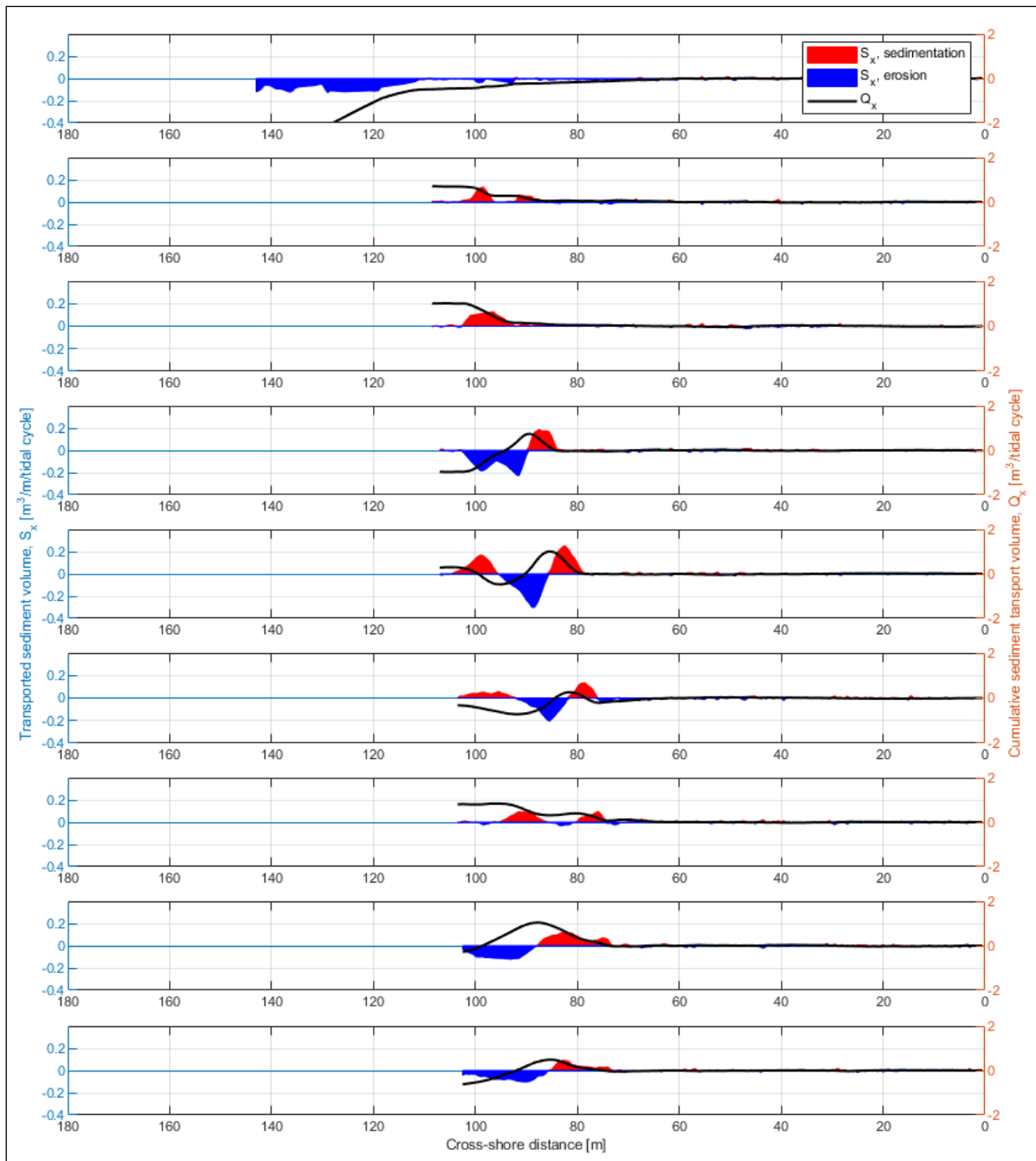


Figure B-3: Transported sediment volumes S_x and cumulative sediment transport volumes Q_x for nine tidal cycles in the period from the January 26 to 31 at cross section 2.

Cross section 3

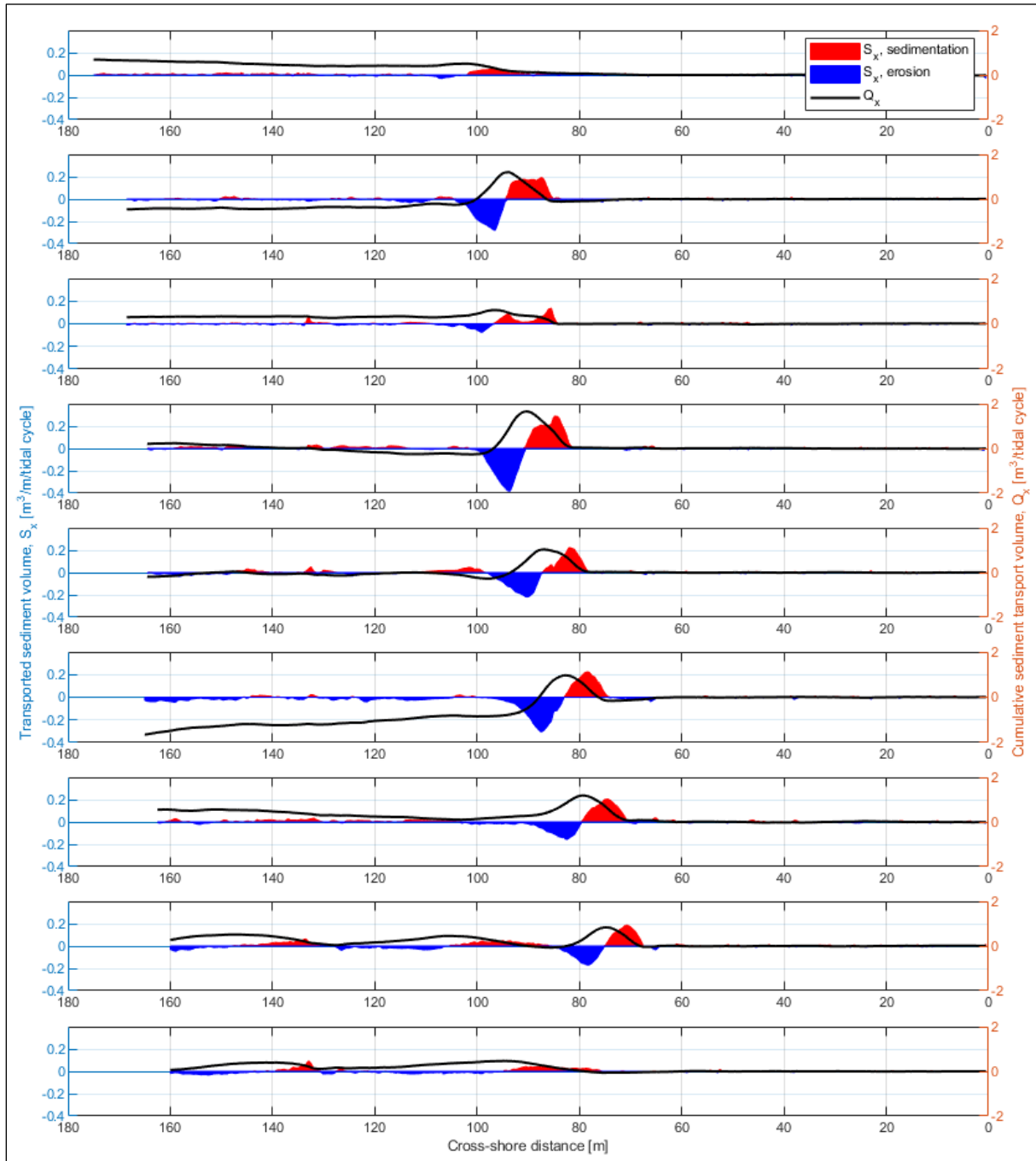


Figure B-4: Transported sediment volumes S_x and cumulative sediment transport volumes Q_x for nine tidal cycles in the period from the January 26 to 31 at cross section 3.

C. XBeach model results for increased wave energy

This appendix shows the results of an additional simulation for both the surf beat model and the hydrostatic swash model. In this simulation the wave energy is increased with respect to the simulation described in chapter 5 by applying shore normal approaching waves. The bed level development and sediment transport volumes in period B (January 26 to 31, 2017) for this wave case are depicted in the figures below.

Bed level development

Surf beat model

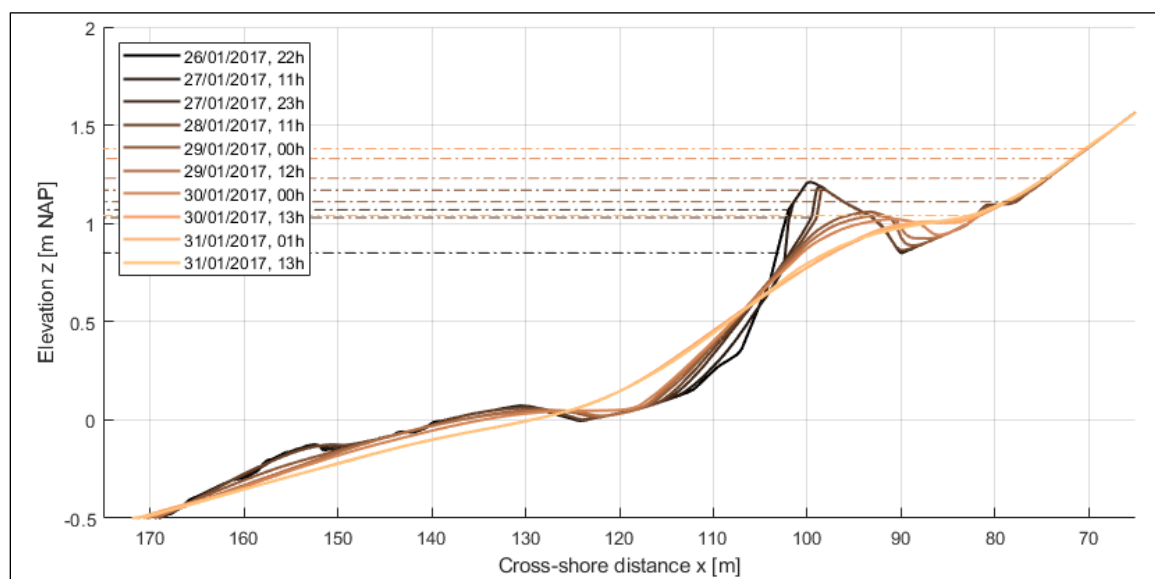


Figure C-1: Surf beat model simulated low water bed levels at cross section 1 in period B (January 26 to 31, 2017). The dashed dotted lines indicate the still high water level (including surge) after each subsequent low water period.

Hydrostatic swash model

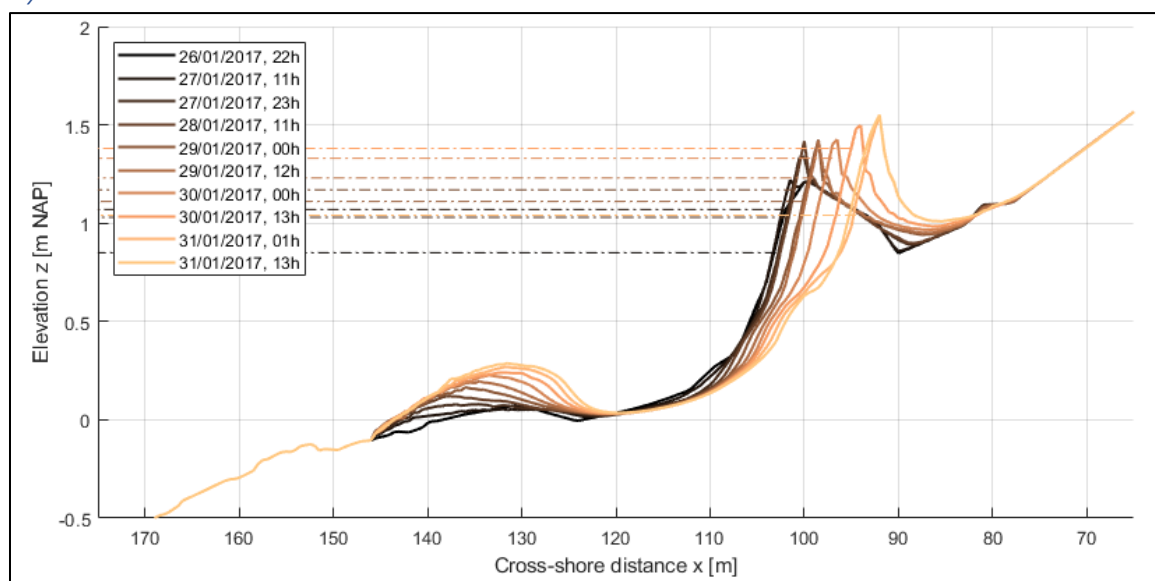


Figure C-2: Hydrostatic swash model simulated low water bed levels at cross section 1 in period B (January 26 to 31, 2017). The dashed dotted lines indicate the still high water level (including surge) after each subsequent low water period.

Sediment transport volumes

Surf beat model

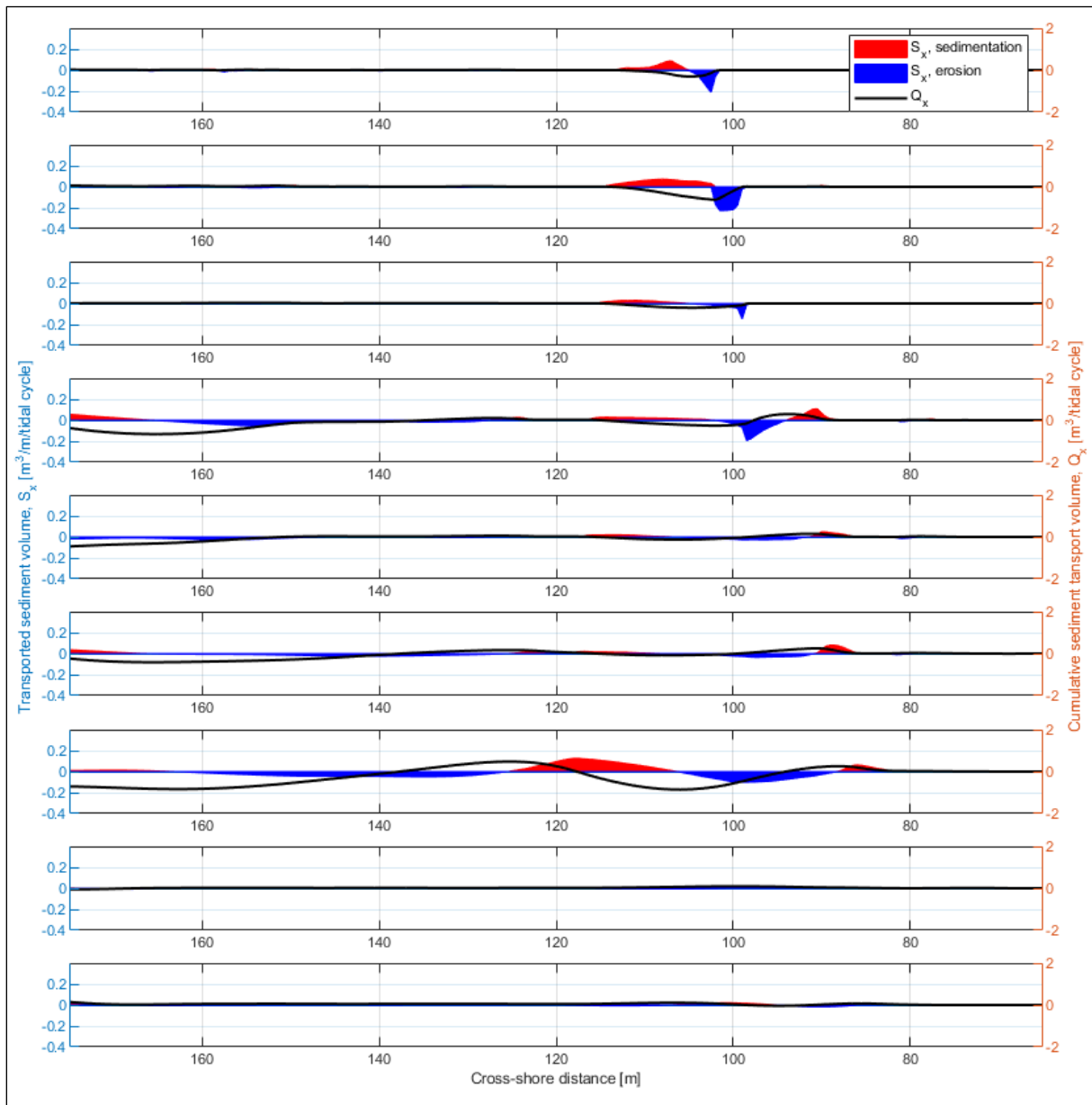


Figure C-3: Surf beat model simulated sediment transport volumes S_x and cumulative sediment transport volumes Q_x for nine tidal cycles in period B (January 26 to 31, 2017) for shore normal approaching waves.

Hydrostatic swash model

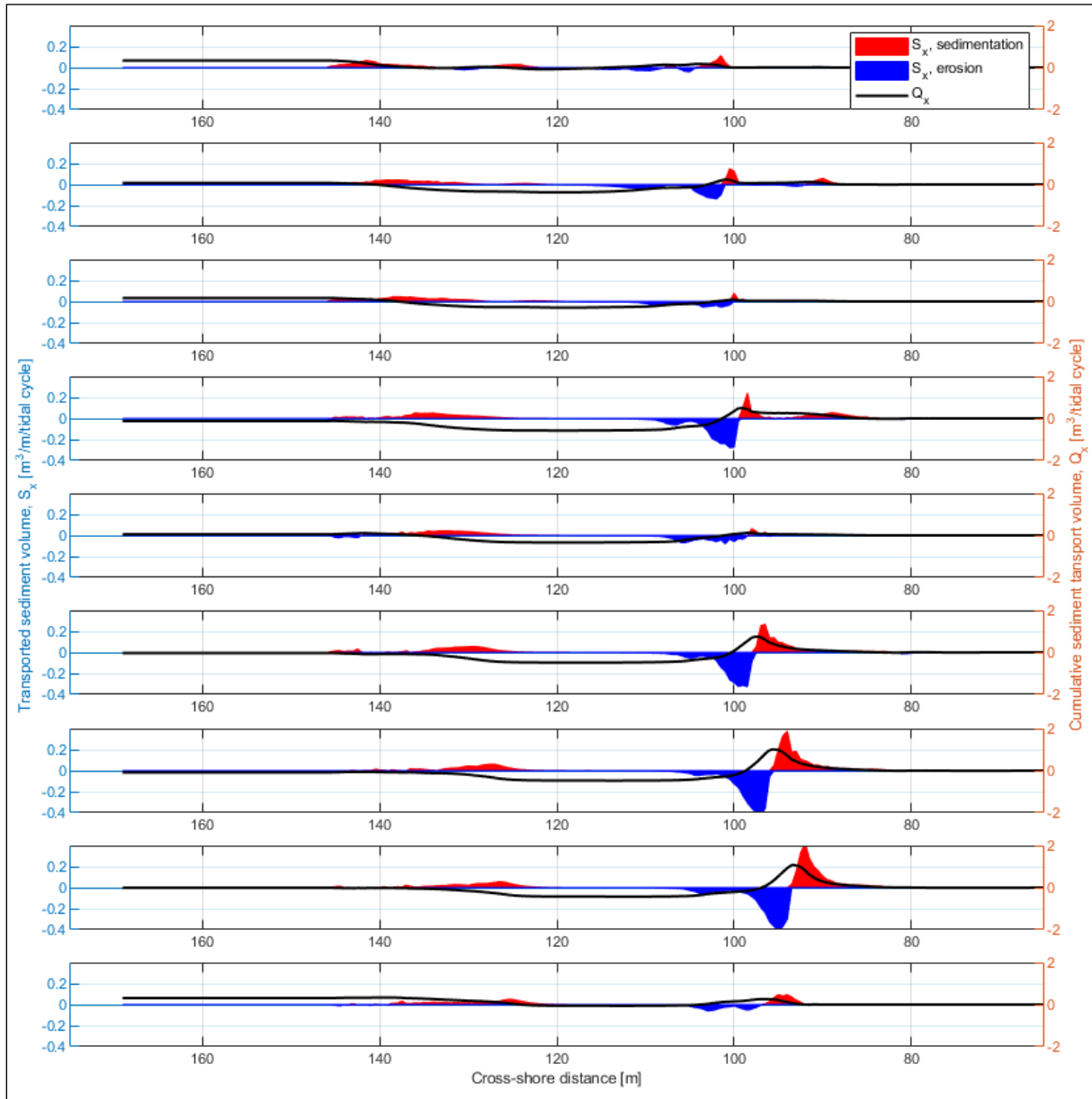


Figure C-4: Hydrostatic swash model simulated sediment transport volumes S_x and cumulative sediment transport volumes Q_x for nine tidal cycles in period B (January 26 to 31, 2017) for shore normal approaching waves.